3-23-2012

Evaluation of the Thorax of Manduca Sexta for Flapping-Wing Micro Air Vehicle Applications

Alex C. Hollenbeck

EVALUATION OF THE THORAX OF MANDUCA SEXTA FOR FLAPPING WING MICRO AIR VEHICLE APPLICATIONS

THESIS

Alex C. Hollenbeck, 2nd Lieutenant, USAF

AFIT/GAE/ENY/12-M22

DEPARTMENT OF THE AIR FORCE
AIR UNIVERSITY

AIR FORCE INSTITUTE OF TECHNOLOGY

Wright-Patterson Air Force Base, Ohio

AFIT/GAE/ENY/12-M22

EVALUATION OF THE THORAX OF MANDUCA SEXTA FOR FLAPPING WING MICRO AIR VEHICLE APPLICATIONS

THESIS

Presented to the Faculty

Department of Aeronautics and Astronautics

Graduate School of Engineering and Management

Air Force Institute of Technology

Air University

Air Education and Training Command

In Partial Fulfillment of the Requirements for the

Degree of Master of Science (Aeronautical Engineering)

Alex C. Hollenbeck, BS

2nd Lieutenant, USAF

March 2012

AFIT/GAE/ENY/12-M22

EVALUATION OF THE THORAX OF MANDUCA SEXTA FOR FLAPPING WING MICRO AIR VEHICLE APPLICATIONS

Alex C. Hollenbeck, BS
2nd Lieutenant, USAF

Approved:

_____	_____
Anthony Palazotto, PhD (Chairman)	date
_____	_____
Lt Col Timothy Radsick, PhD (Member)	date
_____	_____
Mark Willis, PhD (Member)	date

ABSTRACT

The tobacco hornworm hawkmoth (*Manduca sexta*) provides an excellent model from which to garner knowledge pertaining to the development of a Flapping Wing Micro Air Vehicle (FWMAV). Insect-sized FWMAVs will be used by the future warfighter for reconnaissance, nuclear/chemical/biological hazard sensing, and targeting. Civilian applications are also numerous, including searching collapsed buildings for survivors and surveying inaccessible sites such as a nuclear power plant in meltdown.

One of the major challenges facing FWMAV developers is the energetically demanding nature of low Reynolds flapping flight. Investigating the *M.sexta* thorax/wing flapping mechanism as a mechanical system will provide insight into the efficiencies inherent therein. This present work examined the energetics of the thorax under static loading using an innovative load-application technique. It was discovered that the thorax can be characterized by the spring constant $k = 0.62\ N/mm$ under the action of the Dorsoventral flight Muscles (DVMs).

A second experiment involving Constant Stiffness Measurement (CSM) nanoindentation of a major component of the thoracic exoskeleton, the tergum, revealed an elastic modulus of 5 GPa. This value is a benchmark for engineers seeking energy-storing materials for a FWMAV fuselage.

Finally, a truly groundbreaking device was developed and used to directly measure the power requirement of the DVMs at *M.sexta*'s natural flapping frequency (25 Hz). This effort yielded a mechanical power output of 72-143 $W*kg^{-1}$ for that flight muscle group. The feasibility of this approach was confirmed by the agreement of the conclusion with published results, despite the use of the heretofore untried method. The power output requirement confirms the need for lightweight and energy-dense power sources for the fruition of fully-capable FWMAVs.

To my wife and my parents

ACKNOWLEDGEMENTS

Having persevered through the ample coursework and challenging thesis research which have defined my last 18 months, I am keenly aware of the ever-present support of faculty, fellow students and family along the way.

I could not have asked for a more supportive or encouraging research advisor than Dr. Anthony Palazotto. He brought energy and boundless enthusiasm to this project and was always excited to hear about the outcome of my experiments. He is truly one of AFIT's most valuable resources. Dr. Palazotto has also coordinated with Dr. Douglas Smith of AFOSR to make this research possible.

Fellow students Jeremy Murray and Major Ryan O'Hara helped me turn my ideas into functional experiments. Jeremy provided a code he had written which I modified and applied to my own research. Major O'Hara, an absolute genius with electronics and mechanics, filled multiple gaps in my knowledge with varying degrees of tutorial support, once quipping "we'll make an experimentalist out of you yet." Don't be surprised if you see his name on your electronic gadgets in the not-too-distant future.

I would also like to thank 2Lt Kevin Hadsall, a classmate and wingman who teamed up with me to create a finite element model of the hawkmoth thorax as part of a class project. Additionally, Lt Hadsall was invaluable as a study partner and should be credited for not a few positive points on my GPA.

My beautiful wife, Silvey, exhibited more patience than I deserved, taking my long hours, late nights and high stress-state in stride. She even tolerated the dozens of micro-roommates with which we shared our home for nearly a year.

Those friendly fuzzy flappers moved out in October 2011. For that I am indebted to Captain David Sanders, who opened his entomology laboratory for our hawkmoth-rearing needs these past several months. Captain Sanders is continually looking for opportunities to help us out and is an excellent resource for insect-related knowledge.

The entire supply of hawkmoth specimens for the AFIT flapping-wing micro air vehicle research effort originated from Dr. Mark Willis' laboratory at Case Western University in Cleveland OH. Dr. Willis, an expert in all things *Manduca sexta*, has also dedicated time and resources to furthering my understanding of the hawkmoth through hands-on experience and advice.

I also owe a debt of gratitude to my parents, who have encouraged me throughout my entire educational journey. Every good parent tells their children that they are special and smart, but I could tell that mine really meant it. I am certain that I would not be who I am today without their selfless support.

Finally, I would be remiss to leave out Jesus Christ, my Savior and the ultimate Engineer. After all, it is important to cite the source when reverse-engineering someone else's design. His handiwork is evident in the incredible design of the creature I was lucky enough to study for my thesis. As it is in every living thing throughout the earth, to which mankind can always look for inspiration.

But ask the animals, and they will teach you,
or the birds in the sky, and they will tell you;
or speak to the earth, and it will teach you,
or let the fish in the sea inform you.

Which of all these does not know
that the hand of the LORD has done this?
In his hand is the life of every creature
and the breath of all mankind. **Job 12:7-10**

Alex C. Hollenbeck

TABLE OF CONTENTS **PAGE**

ABSTRACT v

ACKNOWLEDGEMENTS vii

LIST OF FIGURES xi

LIST OF TABLES xvii

LIST OF ACRONYMS xviii

1. INTRODUCTION 1

1.1. OBJECTIVE 1

1.2. MOTIVATION 2

1.3. BIOLOGICAL INSPIRATION 4

1.3.1. Flapping Wings 6

1.4. WHY MANDUCA SEXTA? 8

1.4.1. The Thorax 9

1.4.2. Flight Muscles 10

1.4.3. The Exoskeleton 12

2. LITERATURE REVIEW 14

2.1. RESEARCH OUTLINE 14

2.2. FINITE ELEMENT MODELING 15

2.3. NANOINDENTATION FOR ELASTIC MODULUS OF BIOLOGICAL MATERIALS 20

2.3.1. Nanoindentation of Insect Cuticle 20

2.4. POWER ESTIMATION AND MEASUREMENT 23

3. THEORY 30

3.1. STATIC FORCE AND WORK 30

3.1.1. Spring Constant 31

3.1.2. Work 32

3.2. POWER 34

3.3. NANOINDENTATION FOR ELASTIC MODULUS OF THE TERGUM 36

3.3.1. Basic Indentation Process 36

3.3.1.1. Typical IIT Test Chronology 38

3.3.1.2. Load-Displacement Curve 39

3.3.1.3. Calculating Material Properties 41

3.3.2. Continuous Stiffness Measurement 45

3.3.2.1. Simple Harmonic Oscillator 46

3.3.2.2. Modeling the Indenter Prior to Contact 50

3.3.2.3. Natural Frequency 51

3.3.2.4. Modeling Indenter in Contact with Specimen 52

4. EXPERIMENTS 55
4.1. STATIC LOAD EXPERIMENT 56
4.1.1. Design of the Experiment 56
4.1.2. Construction 58
4.1.2.1. The Mount 59
4.1.2.2. Refining the Experiment 61
4.1.2.3. Improved Design with Load Cell 61
4.1.3. Procedure 61
4.1.3.1. Load Measurement 62
4.1.4. Processing 64
4.2. DYNAMIC LOAD EXPERIMENT 67
4.2.1. Design of the Experiment 68
4.2.1.1. Construction 69
4.2.1.2. Set Up 69
4.2.1.3. Refining the Experiment 71
4.2.1.4. Signal Code 74
4.2.2. Procedure 77
4.2.3. Processing 80
4.2.3.1. Checkpoints 80
4.2.3.2. Processing Code 81
4.2.3.3. Power Calculation Code 84
4.3. NANOINDENTATION OF THE TERGAL PLATE 87
4.3.1. Equipment 88
4.3.2. Test Settings 88
4.3.2.1. Indentation Depth 90
4.3.2.2. Number of Sample Points per Test Run 92
4.3.3. Sample Preparation 92
4.3.3.1. Isolating the Tergum 94
4.3.3.2. Mounting with Crystalbond Hot Melt 94
4.3.3.3. Positioning in Machine 95
4.3.3.4. Finding an Adequate Testing Location 96
4.3.4. Processing 97
4.3.4.1. Eliminating Aberrant Samples 98
4.3.4.2. Calculating the Average Elastic Modulus with Matlab 99
5. RESULTS 102
5.1. RESULTS – STATIC LOAD EXPERIMENT 102
5.1.1. Static Load Experiment with Load Cell 103
5.1.1.1. Linear Spring Constant 106
5.1.1.2. Evaluation of Wing Angle vs. Force 107
5.2. RESULTS – NANOINDENTATION EXPERIMENT 111
5.3. RESULTS – DYNAMIC LOAD EXPERIMENT 113

6. CONCLUSIONS 118
6.1. STATIC LOAD EXPERIMENT 118
6.1.1. Recommendations 118
6.2. NANOINDENTATION EXPERIMENT 119
6.2.1. Recommendations 119
6.3. DYNAMIC LOAD EXPERIMENT 121
6.3.1. Evidence for Elastic Storage of Inertial Energy 122
6.3.2. Evidence for Passive Wing Twist 123
6.3.3. Actuators 123
6.3.4. Recommendations 124
6.3.4.1. Improvements to Current Experiment 124
6.3.4.2. Adapting for Future Experimentation 125
6.3.4.3. Wings: Aeroelasticity and Inertial Effects 126
6.4. SUMMARY OF CONCLUSIONS 127
Appendix A. Raising Hawkmoths 130
Appendix B. Matlab Code for Static Experiment Processing 135
Appendix C. Signal and Load Code for Dynamic Experiment 136
Appendix D. Video Proc. and Tracking for Dynamic Experiment 138
Appendix E. Power Calculation Code for Dynamic Experiment 140
Appendix F. Processing Code for Nanoindentation Experiment 141
Appendix G. Complete Results of Static Experiment 142
Appendix H. Modifying Dynamic Device for Full ROM Flapping 147
Appendix I. High-Speed Video Frame Sequence 150
Appendix J. *M.sexta* Thorax Non-Linear Spring FE Model 154
Bibliography 157
Vita 163

LIST OF FIGURES **PAGE**

Figure 1 - System Elements Required for MAVs (McMichael and Francis 1997) 5

Figure 2 - Examples of current bio-inspired FWMAV technology: (A) Wright State's dragonfly (WSU 2011), (B) Harvard's monolithic bee (Harvard 2012), (C) AeroVironment's hummingbird (AeroVironment 2012) 8

Figure 3 – Dorsal view of *M.sexta* coloration (scale is centimeters) 9

Figure 4 - Major body components of *M.sexta* 10

Figure 5 - Hawkmoth flight muscles: (A) Schematic of M.sexta thorax highlighting flight muscles (adapted from [19]), (B). Photograph of flight muscles in cross-section of thorax. 11

Figure 6 - View of tergum with scales removed 11

Figure 7 - Schematic of the dorsoventral (DVM) and dorsolongitudinal (DLM) indirect flight muscles of *M.sexta* in action 12

Figure 8 - Mode shapes of *M.sexta* forewing (Norris, Palazotto and Cobb 2006) 16

Figure 9 - Finite element model of *M.sexta* forewing (Sims 2010) 17

Figure 10 - Specimen cross-section and finite element model geometry overlay. Photo by Tubbs 2011 18

Figure 11 - FE models – (A) First model, thin extruded 2D shape, (B) Final model, 3D shape 18

Figure 12 - Wing hinges modeled as soft (low modulus) material 19

Figure 13 - Realistic wing deflection in FE Model: (A) Undeformed, (B) Application of force representing DVMs, (C) Resultant wing elevation 19

Figure 14 - Schematic of load versus indenter depth into surface for an indentation experiment. P_{max}: indentation load; h_{max}: indenter displacement at peak load; h_f: the final depth of the contact impression after unloading; and S: the initial unloading slope. 21

Figure 15 - Pathway for energy expenditure of a flying insect. The inertial power is required to overcome the momentum of the wings in order to flap. The aerodynamic power is the combination of all aerodynamic forces against the movement of the wings. Parasitic power is negligible for hovering. Induced power accelerates the air through the wing disc. Profile power overcomes the wing drag. (after (Casey 1981)) 24

Figure 16 - Specific power of non-fibrillar (striated, vertebrate) flight muscle (A) and fibrillar (synchronous, insect) flight muscle (B) versus flapping frequency. *M.sexta* flaps at a frequency of 25-30 Hz, which covers a power output range of 82-97 $W*kg^{-1}$ (represented by the blue rectangles drawn over the plot). The upper dotted line is the asymptote for both curves and the lower dotted line corresponds to equal volumes of mitochondria and myofibrils. Adapted from (Pennycuick and Rezende 1984) 26

Figure 17 - Two images superimposed to show thoracic compression and wing elevation angle (from (Tubbs 2011)) 31

Figure 18 - Schematic of the thorax as a mechanical system with spring 31

Figure 19 - Work as the area under a force versus displacement curve 33

Figure 20 - Work as the area under a linear force versus displacement curve 34

Figure 21 - Basic Indentation Test 37

Figure 22 - Schematic of an indentation test. The projected contact area is *A*. *P* is the applied load. *h* is the penetration depth as measured from the surface, and *hc* is the depth of actual contact between the indenter and the specimen. 37

Figure 23 - Representative force-time history for an instrumented indentation test. Contact first occurs at the origin. 39

Figure 24 - Typical load-displacement plot for an instrumented indentatino test. The segments are colored and numbered to match their counterparts from the force-time history in Figure 23. 40

Figure 25 - Pyramidal indenter tips. The Berkovich was used for the experimentation in this research project 43

Figure 26 - Schematic of indentation contact parameters 44

Figure 27 - Simple harmonic oscillator model. *K* is the stiffness of the system, *D* is the damping of the systems, and *m* is the mass undergoing oscillation 47

Figure 28 - Expression of solution for a simple harmonic oscillator model (after (Hay 2009)). ... 49

Figure 29 - Schematic of a nanoindentation machine 50

Figure 30 - Simple harmonic oscillator model accommodating both instrument and contact with specimen 52

Figure 31 – Simple harmonic oscillator model with instrument and contact parameters combined into equivalent expressions 53

Figure 32 - Static load device in use (note: raised platform in front of the device is where the camera rests) 57

Figure 33 – Original concept sketch and constructed device 58

Figure 34 - Schematic of the thorax as a mechanical system with spring 58

Figure 35 - Main components and constructed device 59

Figure 36 - Importance of mounting angle: (A) Original orientation, tergum tilted forward; (B) Elevated 14 degrees, tergum is now horizontal. End of push rod fits flush against the tergum. . 60

Figure 37 - Stack of quarters on push rod weight platform 63

Figure 38 – Depiction of cantilever beam load cell with moth 64

Figure 39 - Example of load cell calibration 65

Figure 40 - Edited images from 2nd iteration: Compressive displacement is now being tracked. The dot is located in the lower right corner of the small white-bordered boxes. The actual small black dot is not readily visible so its location on the push rod is indicated with a yellow circle. The vertical distance used in the calculations is the distance between that dot and the edge of the ruler (top of white-bordered box) 65

Figure 41 - Locations and order of selection for wing angle and thorax vertical compression calculation. Note that points 2 and 3 can be selected anywhere along their respective leading edge lines, which had been traced along the straightest portion of the leading edge of the specimen's forewings. 66

Figure 42 - Portion of the code for wing angles and displacement (note addition of points 4 and 5 over code for first iteration) 66

Figure 43 - Calculation of approximate wing elevation angle as viewed from the perspective of the high-speed camera 68
Figure 44 - Dynamic force experiment SolidWorks design and realized device 70
Figure 45 - Schematic of dynamic load application experiment 70
Figure 46 - Labeled photo of dynamic load experimental setup 71
Figure 47 - Initial Designs: (A) load cell mount; (B) push rod; (C) thin-beam load cell 72
Figure 48 – Proof-of-concept phase of dynamic load experiment. Note paper scraps glued to wings for tracking wing angles. This practice was subsequently deemed unnecessary. 72
Figure 49 - Modified for original cantilever beam load cell: (A) Load cell mount; (B) Updated push rod; (C) Assembly with circuit board for load cell signal amplification and power 72
Figure 50 – Load cell calibration for dynamic load experiment 73
Figure 51 - Portion of code which converts voltage signals from the load cell (*data_ai*) into force in newtons. The tare period is an 80 millisecond period of load readings before the shaker is actuated. The average reading from that period is applied to the force data in order to provide a baseline for the function. 73
Figure 52 - Final iteration of the push rod with angled tip for improved fit 74
Figure 53 - Input for signal code 75
Figure 54 - Typical gap between tergum and push rod at bottom of vertical displacement cycle 76
Figure 55 - Output signals for camera trigger and shaker actuation 77
Figure 56 – Example of force versus time function obtained with the dynamic load application experiment. Note tare portion at outset of test. 78
Figure 57 - Mounted specimen. Note the red wax above and below the moth. The “happy face” was used track the vertical displacement. The blue rectangle with white lines is a piece of a metric ruler with mm markings, used for determining pixels to mm conversion factors. 78
Figure 58 – Matlab code which creates a plot of vertical displacement of the specimen versus time. Note data is cleaned up with a conversion factor and the application of the tare value.... 83
Figure 59 - Plot of vertical displacement of the specimen versus time (or frame number). A negative bias had been applied to this run, inducing a positive displacement of approximately 1mm versus a negative displacement of approximately 0.8 mm. 83
Figure 60 - Force versus time plot from Moth 7 showing initial contact point and the point of maximum powered compression. The force continues to increase after maximum displacement due to inertial forces. 85
Figure 61 - Displacement of Moth 7 showing the locations used for power calculation. Note that the maximum displacement is found using this plot. 85
Figure 62 - Beginning of power calculation code. Inputs p1 and p2 are from the plots, and an array of displacement data is created for this data range. 86
Figure 63 - Code portion which plots the force versus displacement. This function is then used to calculate work. 86
Figure 64 - Force versus displacement plot. The work done on the system (the thorax) is the integral of the force with respect to distance, or the area under the curve. 87

Figure 65 - Calculation of work and power 87

Figure 66 - Representations of tergum movement during flight. (A) Side view of actual tergum; dorsolongitudinal muscle contraction bows the center of the tergum upward and depresses the wings. (B) Dorsoventral muscle contraction (yellow arrows on blue) brings the tergum toward the sternum and bends the sides of the tergum inward to induce wing elevation. 89

Figure 67 - Modulus versus penetration up to 2000 nm. Convergence improves significantly beyond 1000 nm 91

Figure 68 - Cross-section of the tergum. The subject was excised from a specimen and immediately encased in Crystalbond, a thermoset polymer described in subsequent sections of this document. The surface of the cross-section was polished until smooth which enhanced microscopic viewing. The thin, dark line is the tergum and the rest of the tan/brown material is muscle. The red markings on the right indicate locations where the thickness was measured with the microscope's software. 92

Figure 69 - Magnification of outer surface of tergum. The scales have been brushed off, leaving an apparently smooth surface which actually quite rough. The microscopic images on the right were captured with the Nano Indenter G200's video handset feature. 93

Figure 70 - *M.sexta* tergum side view and comparison with intact specimen. The phragma are extensions of the cuticle which support the dorsolongitudinal muscles. Despite how it may appear, the tergum is essentially all one continuous piece. 94

Figure 71 - Tergum mounted to puck with Crystalbond Hot Melt. The thermoplastic polymer completely fills and supports the cavity created by the removal of the flight muscles. The tergum is thin enough for light to pass through, giving the specimen the appearance of amber. 96

Figure 72 - Magnification of tergum using the Nano Indenter G200's video function. The top left corner of the 10x image is out of focus, which was a common due to the curved structure of the tergum. The flattest portions of the tergum were evidenced by an image in which the entire frame was in focus. When defining an array of sample points, the first point was located at the center of the image and the array was populated down and to the right. 97

Figure 73 – Importance of removal of aberrant sample points from the results. (A) Plot of all 36 of the data sets from a test performed at 1000 nm depth. (B) Same test with 14 aberrant data sets removed. Notice the scale changes significantly due to the removal of the outliers and the grouping of the results becomes apparent. 99

Figure 74 - Beginning of nanoindentation data processing code. Matlab makes contact with Excel and reads in the data specified by the min-max range of columns 1 (depth) and 6 (modulus). The for-loop also calculates the mean value for the modulus data for each sample point or run. .. 100

Figure 75 – Portion of code which calculates average modulus for the entire test then plots the original data as a failsafe 101

Figure 76 - Modulus versus depth into surface over the range specified by *min* and *max*. This plot was used to ensure grouping of results was acceptable. Occasionally, data from an errant sample point would make it through the elimination phase but would show up here as a major outlier. 102

Figure 77 - Example of the compression of the thorax related to the force applied to the tergum. 104

Figure 78 - Example of the wing angle induced by the applied force during the second iteration of the static load experiment. Here, the load data was accurately recorded with a load cell. .. 104

Figure 79 - Compilation of all force-compression data from the second iteration of the static load experiment. 104

Figure 80 - Combined load vs. compression data with linear fit 105

Figure 81 - Combined wing angle data from static load experiment 105

Figure 82 - Averaged wing angle data from static load experiment 106

Figure 83 - Theoretical representation of the wing and hinge mechanism. The centroid of the wing is located at the red dot, which is distance *L* from the hinge. The push rod (or a DVM) applies a force *F* to the base of the wing, located a distance *d* from the hinge. The weight of the wing *mg* acts as a force through the center of gravity, which must be counterbalanced by the applied force *F*. 108

Figure 84 - Results (above) compared with a plot of Eqn. 58 with C2 set equal to 1. The shape is very similar, demonstrating that the 2nd-order fit is an appropriate approximation of the real wing angle response to DVM loading. 110

Figure 85 - This plot of Eqn. 59 shows the range of possible power densities for the DVMs assuming that flight muscle mass is 20% of the total body mass. The ratio of DVMs to flight muscle mass is represented by the horizontal axis. The author estimates that the DVMs comprise 15% to 30% of the flight muscle mass. That region is circled. 116

Figure 86 - Typical *M.sexta* pupa. The wins are small and wrapped around the thorax and upper abdomen. In the wild, these pupa use the segmented abdomen to burrow under soil or leaves for protection from the elements until it is time to eclose. 130

Figure 87 - Two freshly-eclosed *M.sexta* specimens. One is only 10 minutes old and has not inflated its wings. 131

Figure 88 - Enclosure for the pupae: (A) Closed box creates day/night conditions with a timer controlling the LED lights, shown in part (B) 132

Figure 89 - Adult enclosure: (C) Moths sit dormant on the mesh wall, (B) Lid closed, light can pass through. The cage sits inside a cardboard box lined with paper bags to facilitate cleaning. Adults often emit meconium hours or even days after eclosion. 133

Figure 90 – 200x Magnified image of moth scales (Jenikova 2005) 134

Figure 91 - All data from first round of static load tests. No load cell was used and the data is not reliable. 142

Figure 92 - Compilation of complete force-angle results of first iteration 143

Figure 93 - Defective results removed 144

Figure 94 - Array of data used for the production of the plot of average wing angle versus force 144

Figure 95 - Average wing angle for right and left wings for the first iteration. 145

Figure 96 - Average wing angle versus applied force (first iteration of static load experiment) 145

Figure 97 - Comparison of original dynamic DVM load device (left) and the modified DVM/DLM load concept (right) 147

Figure 98 - Location of longitudinal compressive force simulating DLM contraction. This image shows only the tergum, but the entire thorax would be intact for this experiment. The head and abdomen must be removed for access to the load application points at the front and rear phragma. 148

Figure 99 - Side view of the conceptual mechanism for bi-directional load application. The location of the tergum (front facing right of page) is indicated on the left. The equivalent four-bar linkage is given on the right. The top is anchored and the bottom piece simply moves up and down just like in the original dynamic load experiment. 148

Figure 100 - Sequential representation of one full cycle. From left to right: Shaker is at lowest displacement and DLM compression is complete; shaker travels upward; shaker is at maximum displacement with full DVM compression; shaker travels downward; longitudinal compression begins again. 149

Figure 101 - Geometric model of the thorax-wing system (Demasi, Palazotto and Hollenbeck 2012)..... 154

Figure 102 - Finite element model of the thorax-wing mechanism (Demasi, Palazotto and Hollenbeck 2012)..... 155

Figure 103 - Distributed loads applied to the tergum (DVM simulation) and the phragma (DLM simulation), (Demasi, Palazotto and Hollenbeck 2012) 156

LIST OF TABLES **PAGE**

Table 1 - Summary of power density estimations for the hawkmoth *M.sexta*. Some researchers reported their results as power per body mass. These have been converted to power per muscle mass by assuming a flight muscle to body ratio of 20% [19]. The power per muscle mass numbers indicated in bold font are the most pertinent values for this study, as they have been obtained directly from analyses of the flight muscles. The power input is also presented below. Stevenson and Josephson report power consumption based on metabolic analysis of the hawkmoth in flight and the 20% flight muscle to body mass ratio. Theirs is likely the most accurate power input value. 29
Table 2 - Nanoindentation settings and user inputs 90
Table 3 - Complete results from the nanoindentation experiment. The "*time run began*" row points out the passing of time before the initiation of the test after the preparation of the tergum. The "*# good samples*" row gives the actual number of samples used to determine the average modulus after the erroneous samples were removed. The "*depth range*" is the range from which the average modulus was calculated. 111
Table 4 - Summary of elastic modulus values of the tergum found by nanoindentation 112
Table 5 –Summary of power calculations. The calculated power is the absolute power required for the DVMs to fully elevate the wings at 25 Hz.....113
Table 6 - Compilation of *M.sexta* power densities including this author's contribution 117

LIST OF ACRONYMS

AFIT – Air Force Institute of Technology

AFOSR – Air Force Office of Scientific Research

CSM – Constant Stiffness Measurement

DAQ – Data Acquisition (board)

DARPA – Defense Advanced Research Projects Agency

DLM – Dorsolongitudinal Muscle

DoD – Department of Defense

DVM – Dorsoventral Muscle

FWMAV – Flapping Wing Micro Air Vehicle

fps – frames per second

IIT – Instrumented Indentation Testing

MAV – Micro Air Vehicle

M.sexta – *Manduca sexta*

RoM – Range of Motion

EVALUATION OF THE THORAX OF MANDUCA SEXTA FOR FLAPPING WING MICRO AIR VEHICLE APPLICATIONS

1. INTRODUCTION

1.1. Objective

This research effort examined a biological flight mechanism, the thorax/wing structure of the hawkmoth (*M.sexta*), as a mechanical system in order to obtain useful knowledge related to the development and construction of Flapping-Wing Micro Air Vehicles (FWMAVs). Three major experiments were carried out over the course of this research, all of which contributed valuable data to ongoing FWMAV investigations.

First, the *k* value, or linear spring constant, of the thorax/wing system under static compressive loads was determined using a force-displacement analysis. The loads were applied in such a way as to simulate the effect of contraction of the elevator flight muscles, also known as the dorsoventral muscles, or DVMs (nomenclature after Eaton 1971). This data furthers the understanding of this biological organism from a mechanical standpoint and provides a basis to which current and future FWMAVs can be compared.

Next the thorax/wing mechanism was further investigated using an innovative device which artificially induced full-elevation flapping in euthanized *M.sexta* specimens by the dynamic application of force. This experiment gathered load, compression and time data which enabled calculation of the mechanical power required to reproduce the wing-elevating function of the DVMs, thereby approximating the actual power output of that muscle group. It is well-known that flapping flight, especially in low Reynolds conditions like *M.sexta* and manmade FWMAVs experience (Sun and Du 2003), is

"energetically demanding" and requires a very high power density in the actuation mechanism (muscles in the case of organisms) (Ellington 1985). This constitutes a challenge to engineers searching for micro power sources and power delivery mechanisms for FWMAVs. The power density of *M.sexta*'s flight muscles will provide a much-needed benchmark which engineers can aspire to meet or surpass with their own power sources. Additionally, modifications to this device may allow full range of motion flapping to be artificially produced in the near future (see Appendix H), which would mean that trying to tether, track or somehow immobilize a living, hovering moth would no longer be necessary to study certain aspects of its steady-level hovering flapping motion such as wing kinematics and aeroelastic effects. High speed cinematography and sensory techniques can then be applied to systematically examine the biomechanics of the wing/thorax system, especially the highly complex motions of the hinge region.

A third experiment, run concurrently with the dynamic experiment, endeavored to use nanoindentation to find the elastic modulus of the largest exoskeletal component of the thorax, the tergal plate, or tergum. This component of the exoskeleton bends significantly during flapping and may be a key player in inertial energy storage. Therefore, categorizing its material properties and construction is an important step toward understanding the entirety of this species' flight mechanism. This understanding, in turn, will lead to more informed decisions related to FWMAV design in the near future.

1.2. Motivation

Small, autonomous and agile MAVs are sought because the modern battlefield often presents soldiers with a rapidly changing combat environment where quick and covert

surveillance of enemy movements is not always available. Insect-sized MAVs, with dimensions on the order of a few inches or less, will be able to perform close-quarters reconnaissance missions, which formerly put troops and airplanes in harm's way, by flying unobserved over the enemy in broad daylight or landing inconspicuously on a wall or a telephone pole. In addition to providing video or still images, these robots will be capable of sensing the presence of chemical, biological or nuclear weapons (McMichael and Francis 1997). A disposable MAV can be used as a sacrificial targeting device, attaching itself as a homing beacon to an enemy vehicle (Bonsor 2012).

The Department of Defense (DoD), in cooperation with the Defense Advanced Research Projects Agency (DARPA) is pursuing the development of an insect-sized MAV in the near future (DoD 1997). These MAVs will be smaller than 15cm in any dimension, affordable to mass-produce and highly capable. In addition, these vehicles will have a range of up to 10 kilometers with a mission duration of 20 to 120 minutes. These missions will require real-time imaging, bio-chemical sensing, targeting, communications, and surveillance (DoD 1997). The size constraint exists because:

> *The reconnaissance application is a primary driver behind the first generation of MAVs. Micro sensors…suggest the possibility of reduced latency and greatly enhanced situational awareness for the small unit or individual soldier. This is partly attributed to the direct connectivity envisioned between these systems and the "user" in emerging operational concepts. Direct connectivity means the user has to carry it. So the MAV must trade favorably with other soldier assets - like water and ammunition. The system must also be affordable. It must have a vanishingly small logistics tail, and for many missions it must be intrinsically covert. All this points to a highly compact, small system. (McMichael and Francis 1997)*

The scope of MAV applications extends beyond military requirements. Small, nimble, autonomous or semi-autonomous flying robots will be useful for gathering information in nearly any dangerous scenario which precludes direct human participation. For example, a MAV equipped with air-quality sensors could enter a contaminated building or area, enabling rescuers to determine the nature of the contaminant and whether it is or when it will be safe to enter. Firemen might send a MAV into a burning building to search for people. Similarly, a MAV could enter small or dangerous crevices in a collapsed and unstable building. Police might use a MAV in much the same way the military will, thereby reducing the risk of human casualties (Alexander 2002).

1.3. Biological Inspiration

A conventional approach to aircraft design, where subsystems are secondarily fitted inside a predetermined airframe, is not currently viable in the emerging and complex world of MAVs. These miniscule flying machines require fast-response controls, integrated lift and propulsion devices, flexible structures and micro-machinery, all of which must operate in low Reynolds aerodynamics (Reeder 2011). Figure 1 delineates this functional complexity (McMichael and Francis 1997).

Biological organisms are usually optimized under a broad range of constraints that might not necessarily apply to an engineered device with very specific requirements. For example, the wings of *M.sexta* are likely not optimally designed for maximum lift under a specific flight regime. Instead, the shape and size of these wings are the result of compromise between the requirements of hovering flight, evasive maneuvers, forward

flight and takeoff. The structure of the wings is also limited by their development within the pupa casing and their need to unfurl and harden upon eclosion[1].

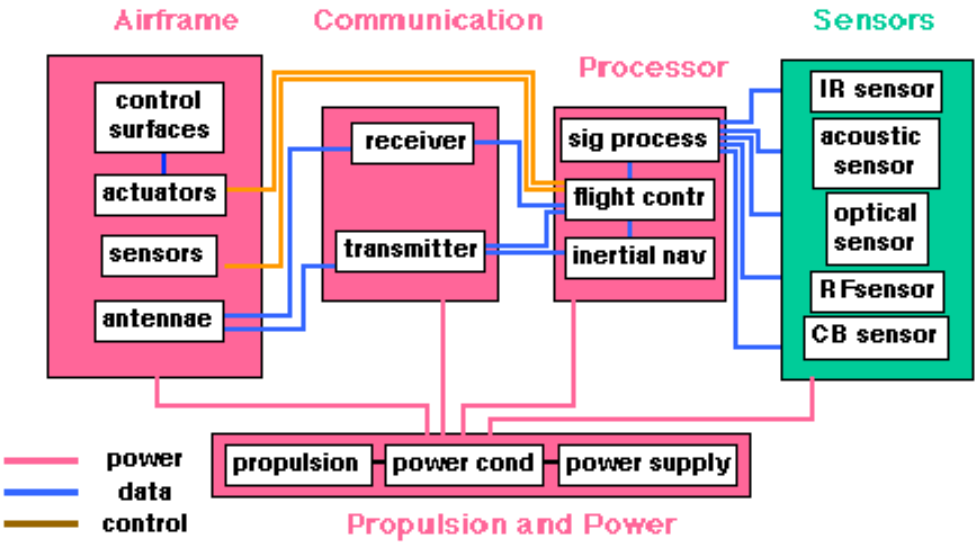

Figure 1 - System Elements Required for MAVs (McMichael and Francis 1997)

A biological organism, therefore, should not be reverse-engineered with intent to duplicate all of its functions. Instead, engineers involved in biomimetics (the field of applying biological functions to manmade designs) should approach this problem with the understanding that their design constraints are often less demanding, or at least more specific, than those of nature, which enables deviations from the way the organism is designed. With this in mind, the goal of engineers in the FWMAV field is not to create a mechanical analog of *M.sexta* or some other insect. Instead, the aim is to characterize the design and functions of a species in order to apply that knowledge toward a well-tailored solution for the specific design problem. The approach to this characterization may then be generalized for any flapping-wing insect species, such as dragonflies, butterflies or

[1] *Eclosion* is the act of emerging from the pupa as an adult

bumblebees, in order to further increase the knowledge base of natural FWMAV technology.

1.3.1. Flapping Wings

Small, lightweight aircraft traveling at low speed experience very unstable flight conditions. An aircraft which weighs merely a few ounces does not have significant inertia so even a slight wind gust can trigger relatively large aerodynamic forces and changes in momentum (Ashley 1998). Highly-sensitive flight control systems are required to maintain stability at such low Reynolds number conditions. Ifju has successfully shown that is possible to overcome some instability issues, such as wind gusts, with fixed but flexible wings using bio-inspired adaptive washout (analogous to the rigid but flexible wings of a gliding bird) on his propeller-driven MAVs (Ifju, Stanford and Kyu-Ho 2008). However, the dual challenges of providing low speed stability *and* producing propulsive thrust are solved simultaneously in nature each time an insect or a bird flaps its wings to get airborne:

> *Interestingly, nature's flyers of the same scale [less than 15cm] use another source of unsteady aerodynamics, flapping wings, to create both lift and propulsive thrust.* (DoD 1997)

There are currently many bio-inspired FWMAVs in various stages of development. Some are already capable of self-powered, semi-autonomous flight. Wright State University has created at least 8 different FWMAVs between 2009 and 2011, having studied the kinematics of dragonflies (Figure 2.a), cicadas, butterflies, and ladybugs (WSU 2011). Some of their MAVs are capable of flying for up to 20 minutes at a time, and a few have carried small cameras.

The Harvard Microrobotics Laboratory has been in existence since 2000. Their research consists of soft actuators, sensors, ambulatory microrobots, and flapping-wing microrobots, or FWMAVs. They have had many successes in these areas, including the design and construction of a fly-sized FWMAV the bee-inspired flier shown in Figure 2.b (Harvard 2012). Their fly achieved the first lift-off of a biologically-inspired at-scale FWMAV in 2008 (Wood 2008).

AeroVironment, Inc., an engineering company which has had successes in a diverse range of challenging design problems, is developing a hummingbird-inspired FWMAV (Figure 2.c). They were awarded a Phase II contract extension for their "nano" air vehicle development program by DARPA in 2009 (AeroVironment 2012), and have since met or exceeded all of the technical milestones, which are (AeroVironment 2009):

1. Demonstrate precision hover flight.
2. Demonstrate hover stability in a wind gust flight which required the aircraft to hover and tolerate a two-meter per second (five miles per hour) wind gust from the side, without drifting downwind more than one meter.
3. Demonstrate a continuous hover endurance of eight minutes with no external power source.
4. Fly and demonstrate controlled, transition flight from hover to 11 miles per hour fast forward flight and back to hover flight.
5. Demonstrate flying from outdoors to indoors and back outdoors through a normal-size doorway.
6. Demonstrate flying indoors 'heads-down' where the pilot operates the aircraft only looking at the live video image stream from the aircraft, without looking at or hearing the aircraft directly.
7. Fly the aircraft in hover and fast forward flight with bird-shaped body and bird-shaped wings.

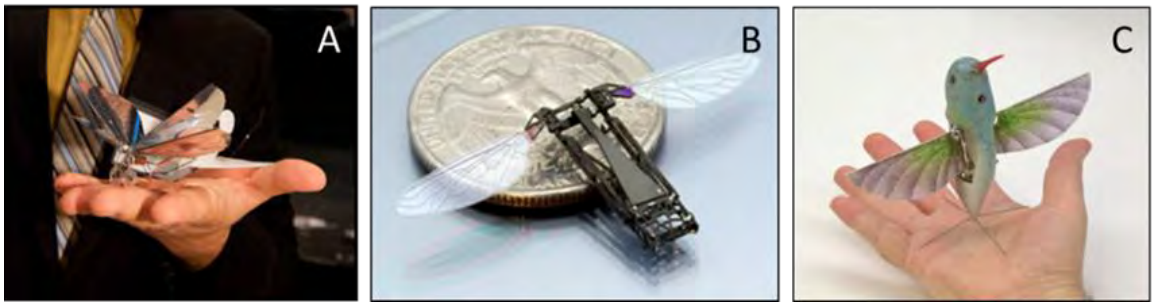

Figure 2 - Examples of current bio-inspired FWMAV technology: **(A)** Wright State's dragonfly (WSU 2011), **(B)** Harvard's monolithic bee (Harvard 2012), **(C)** AeroVironment's hummingbird (AeroVironment 2012)

This hummingbird FWMAV was named among the "50 Best Inventions of 2011" by Time Magazine in its inventions issue (FedScoop 2011). Its picture graced the cover, indicating that people really are becoming more aware of and interested in this technology (FishbowlNY 2011).

1.4. Why Manduca Sexta?

Many flying insects exhibit the type of hovering agility necessary for FWMAVs. While hummingbirds and bats are also capable of true hovering flight, insects like *M.sexta* are closer to the target size range for MAVs. Because they are naturally adept at hovering in place during feeding even in gusty conditions, hawkmoths display a remarkable ability to hover in small, enclosed spaces, making them an excellent model for FWMAVs with high degrees of stability and control (Casey 1981). In addition, only insects possess an exoskeleton with elastic proteins (called *resilin*) which enable the entire thorax to function as a mechanical spring-damper system capable of efficiently operating at resonance during flapping flight (Bolsman 2010). *M.sexta* stands out among the flying insects for its large size and relatively simple design. A member of the moth family *Sphingidae* and Hawkmoth genus *Manduca*, this species is designated *sexta* for the six

pairs of orange dots on the abdomen (Figure 3) (butterfliesandmoths.org 2012), and is often referred to by the common name Tobacco Hornworm Moth. They are easy to rear (see Appendix A), readily available in the wild (in fact they are often considered a pest species), and provide a suitable platform from which to study a basic flying insect. Their flight motor system consists of a simple arrangement of two sets of massive flight muscles which are easily distinguished in dissection. *M.sexta* are sturdy and robust, with large larval and adult stages. These insects are sometimes referred to as the white lab rat of the entomology field (Tubbs 2011).

Figure 3 – Dorsal view of *M.sexta* coloration (scale is centimeters)

1.4.1. The Thorax

The body of *M.sexta* is composed of three main sections common to any insect: the head, thorax and abdomen (Figure 4). The head contains the brain, two large compound eyes, and the coiled proboscis, used for feeding on plant nectar. The abdomen contains most of the organs related to digestion, reproduction, and circulation. Between them, the thorax serves as a powerhouse for muscular activity related to locomotion.

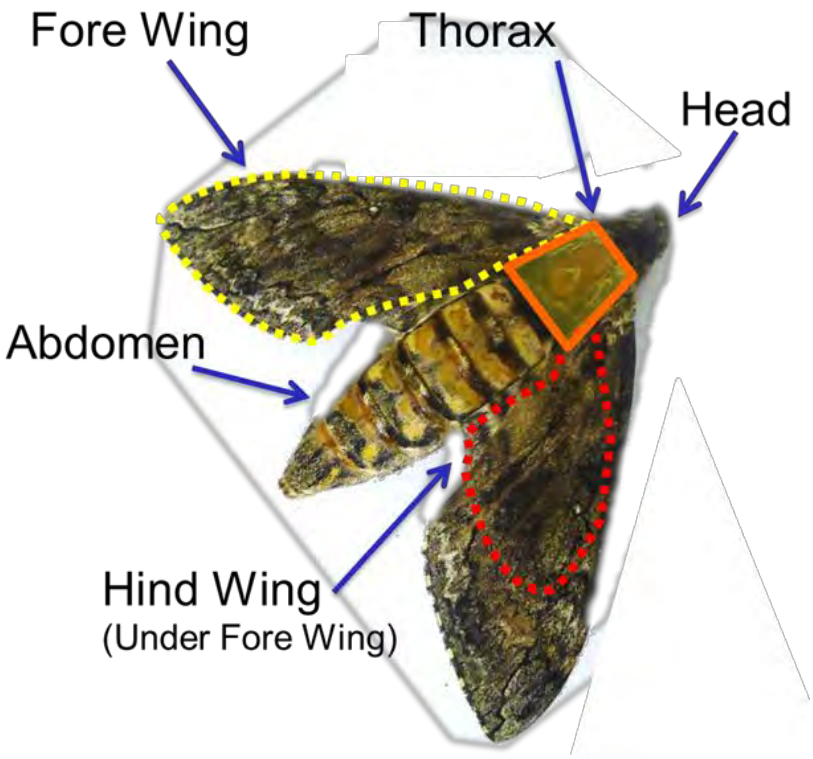

Figure 4 - Major body components of *M.sexta*

1.4.2. Flight Muscles

All four wings and all six legs protrude from the thorax and are controlled by the muscles therein. Therefore the thorax is the prime area of interest for research centered on power generation and the mechanical nature of power transfer related to flight. Figure 5 shows a cross-sectional schematic of the thorax, highlighting the major muscle groups (Wasserthal 2001), and a photograph of a cross-section of an *M.sexta* specimen with the muscle groups clearly visible.

There are two large muscle groups in the thorax that control the flapping motion through a method known as indirect flight. The term arises from the fact that the flight muscles do not act directly on the wing. Instead, they push and pull on the thoracic exoskeleton which transfers energy to the wings through a complex hinge system (Stevenson and Josephson 1990).

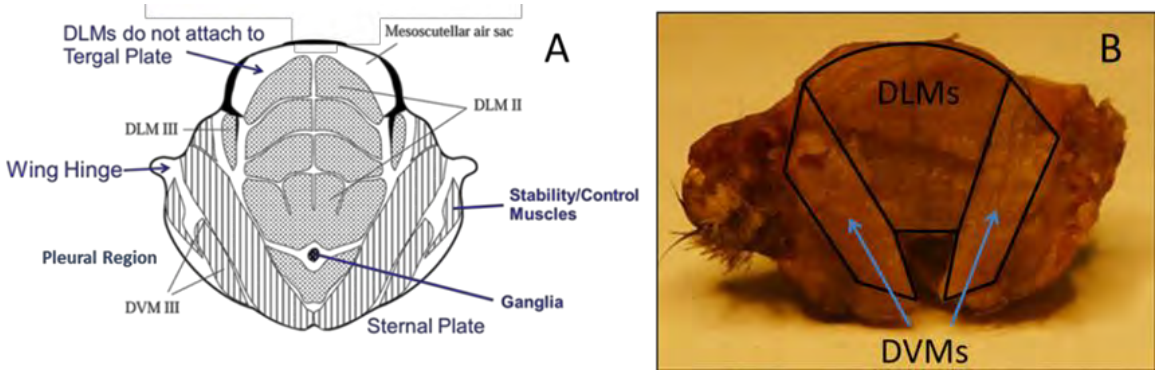

Figure 5 - Hawkmoth flight muscles: **(A)** Schematic of M.sexta thorax highlighting flight muscles (adapted from [19]), **(B)**. Photograph of flight muscles in cross-section of thorax.

The powerful, lift-inducing downstroke is caused by the contraction of the largest muscle group in the thorax, the Dorsolongitudinal Muscles (DLMs) (nomenclature after Eaton 1971). These muscles span the length of the thorax along the inner surface of the tergum (or tergal plate) and connect to extensions called *phragma* at the front and rear of the thorax. The tergum is the largest plate of the exoskeleton and is located on the top of the thorax (Figure 6).

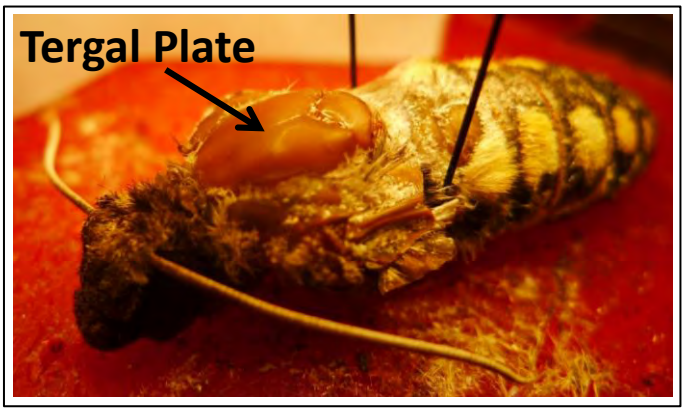

Figure 6 - View of tergum with scales removed

Contraction of the DLMs pulls the phragma toward one another and bows the tergum upward, bringing the inner hinge of the wing with it, which swings the wings

downward to a maximum displacement of about 30 degrees below horizontal in the stroke plane during hovering flight (Willmott and Ellington 1997).

The wings are similarly elevated by the contraction of the DVMs which span vertically, at a slight angle, from the left and right sides of the tergum to the center of the sternum. Contraction of these muscles vertically compresses the thorax and lowers the inner hinge at the base of the wings, raising the wings to a maximum angle of approximately 65-75 degrees above horizontal in the stroke plane during hovering flight (Willmott and Ellington 1997). Figure 7 shows a schematic of these flight muscles in action.

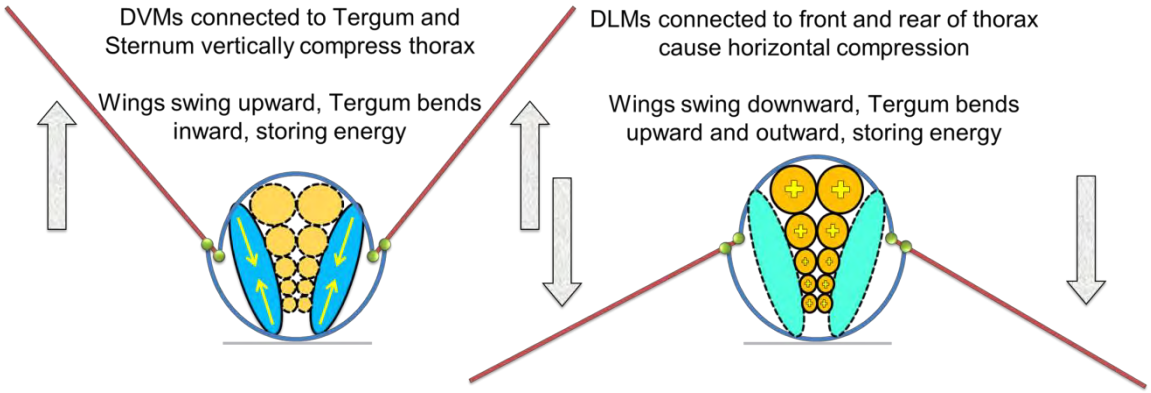

Figure 7 - Schematic of the dorsoventral (DVM) and dorsolongitudinal (DLM) indirect flight muscles of *M.sexta* in action

This vertical compression of the thorax by the DVMs, and the subsequent elevation of the wings, is the primary subject of research for the static and dynamic load experiments of this thesis. The nanoindentation experiment seeks the elastic modulus of the tergum due to that component's crucial bending role during flight.

1.4.3. The Exoskeleton

M.sexta, like all insects, has its structural support on the outside of the body in the form of an exoskeleton, or cuticle. The exoskeleton of flying insects must be lightweight and

efficient while still resilient enough to provide protection from predators and the elements. The cuticle is a composite of extremely strong, high-modulus crystalized chitin nano-fibers bound by a soft protein matrix along with small quantities of polyphenols and lipids (Vincent and Wegst 2004), (Wainwright, et al. 1982). Water is also present in the cuticle and influences the material properties by acting as a plasticizing agent (Hillerton 1984). The cuticle, in one form or another, makes up nearly every outer part of an insect, including wings, shells, structural stiffeners, veins and joints.

In *M.sexta*, as with any insect with an indirectly-powered flight system, the thorax almost certainly absorbs and returns significant amounts of inertial energy with each wing beat (Casey 1981), (Sun and Du 2003). The rapid movement of the wings swing from their natural upper or lower extremes produces large quantities of kinetic energy. At each extreme wing position, this kinetic energy must be counteracted as the wing is slowed and the direction of movement is reversed. If the thorax consisted of a rigid-joint system, with no provision to store this excess energy, the flight muscles would be required to provide all of the energy necessary for deceleration and acceleration. This would represent a major inefficiency is the flight mechanism and, as will be shown in the literature review, would probably require more power than these muscles are capable of producing. Therefore, the entire muscle/cuticle/wing system likely makes use of the energy-storing ability inherent in elastic materials and composites. It is also apparent that the insect flaps at or near the resonant frequency of the system, a quality which indicates, as expected, that flapping efficiency is ideal for flight (Khan and Agrawal 2011). Because the tergum is the largest single piece of the thoracic exoskeleton, and bends significantly during flight, it is seen as a crucial component whose mechanical properties are of

interest. The elastic modulus of this component found by nanoindentation may be used in the future for mechanical energy storage calculations as well as Finite Element (FE) modeling.

2. LITERATURE REVIEW

2.1. Research Outline

This chapter provides investigations of three key subjects pertinent to the present research. The first is one which is currently underutilized in FWMAV design: finite element modeling of biological components and systems. Some FE modeling and analysis of the hawkmoth thorax was performed early in the project and subsequent research efforts were partially based on that experience. Ongoing FE models of the thorax/wing system of *M.sexta* are incorporating much of the knowledge gathered through these endeavors (Demasi, Palazotto and Hollenbeck 2012). This research is described in Appendix J.

Next, nanoindentation for determining material properties is discussed. Particular attention is paid to the use of nanoindentation to investigate biological materials because this is the avenue through which the elastic modulus of the tergum of *M.sexta* was investigated. The value of evaluating insect cuticle as an engineering material is also explained in depth.

Finally, the various aspects of power production, measurement, and calculation are discussed as they relate to historical research and analyses of flying insects. That section lays out the definitions of different classifications of power requirements regarding flapping wing flight. As this current work is interested in the mechanical power

output of *M.sexta* flight muscles, particular attention is placed on previous calculations, measurements and estimations of that insect's mechanical power output.

The details and mathematics of energy storage, nanoindentation and power calculation, as they pertain to these experiments, are dealt with in Chapter 3 of this document. The experiments are thoroughly set forth in Chapter 4 and discussions of the experimental results and of the subsequent conclusions are presented in Chapters 5 and 6, respectively.

2.2. Finite Element Modeling

Some FE modeling was accomplished near the outset of this project as an exploration into the possibilities of modeling the thorax/wing system of *M.sexta* and as a way to build an understanding of parameters which may be useful for future models. However, the bulk of the author's research did not focus on modeling, so the background of FE analysis and its current use in biological modeling is discussed only briefly here. The concepts behind the FE method have been employed in various forms since the 1940's, though the term "finite element" was not coined until 1960 (Hillerton 1984), (Cook, et al. 2002). The original method allows simple structural calculations regarding stress and strain to be performed by hand for basic structural problems, but any practical applications require the computational power of a computer. Advancements in computer technology have led to a surge in FE analysis using ever-improving software programs. A biological organism is extremely complex and cannot be accurately modeled without the use of these highly advanced FE analysis techniques. Researchers have only recently undertaken to model components or subsystems of various biological organisms (Dumont, Grosse and Slater 2009).

Few FE models of insect components have been created. In 1998, before the advent of highly-powerful FE modeling technology, a code was written for modeling a portion of a cockroach exoskeleton (Flannigan 1998). More recently, members of the FWMAV research effort at AFIT have created and analyzed FE models of *M.sexta* forewings.

Norris examined the mode shapes of the forewing (Figure 8) (Norris, Palazotto and Cobb 2006). That work was subsequently expanded with the creation of an improved model of the forewing (Figure 9) and comparison of its results to the performance of an actual *M.sexta* forewing as it "flapped" through a natural range of motion on a flapper device (Sims 2010), (Sims, Palazotto and Cobb 2010).

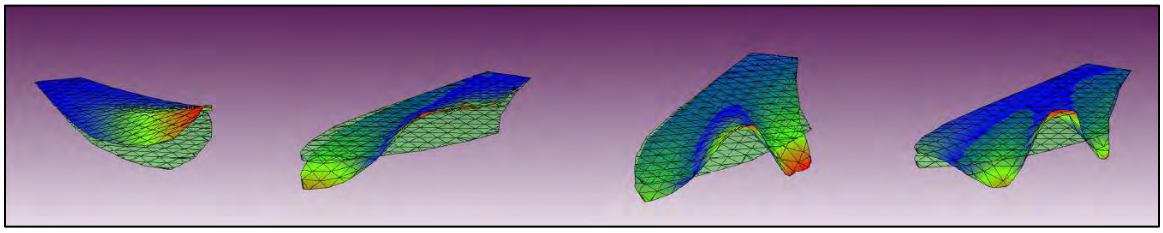

Figure 8 - Mode shapes of *M.sexta* forewing (Norris, Palazotto and Cobb 2006)

Similarly, FE models of the forewing have been used to examine the effects of fluid damping versus inertia in wing bending (Combes and Daniel 2003). This topic is covered in more detail as it relates to the conclusions of the dynamic load experiment given in Chapter 6 of this thesis. Another, more recent though non-biological, application of FE analysis is an examination of a hyperelastic latex membrane used on FWMAV wings (Chakravarty and Albertani 2011).

Chakravarty and Albertani were able to successfully model the deformation and energy absorption behavior of this synthetic membrane and compare it to experimentally-

derived values. Although their technique was applied to manmade materials it is conceivable that it could be extended to biological wing membranes in the future.

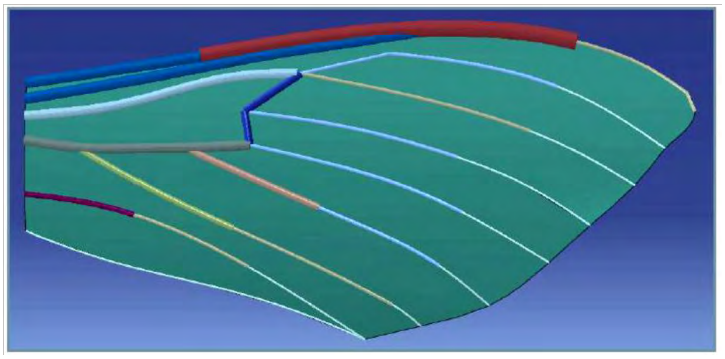

Figure 9 - Finite element model of *M.sexta* forewing (Sims 2010)

Researchers have recently devised mathematical models of an insect thorax (Khan and Agrawal 2011). However, an extensive search of the literature has turned up no evidence of FE models of a full thorax. The author developed what is most likely the first FE model of the *M.sexta* thorax in the spring of 2011 as a precursor to the present work (Hollenbeck, Palazotto and Willis 2011). The primary goal was to create a model which would provide insight into the function of the wing hinge. Effort was made to use realistic dimensions despite the inherent geometric simplifications of the model. Figure 10 shows a cross-section of an *M.sexta* thorax overlaid by a cross-section of the model. The lower half of the thoracic exoskeleton, consisting of the sternal and pleural plates, was modeled as a braced structure because it is much stiffer than the tergal plate and does not bend significantly during flight (Khan and Agrawal 2011). The first iteration involved this geometry being extended back for a few centimeters, essentially creating a "slice" of the thorax (Figure 11.a). An improved model incorporated a 3-dimensional taper more closely resembling actual thoracic geometry (Figure 11.b).

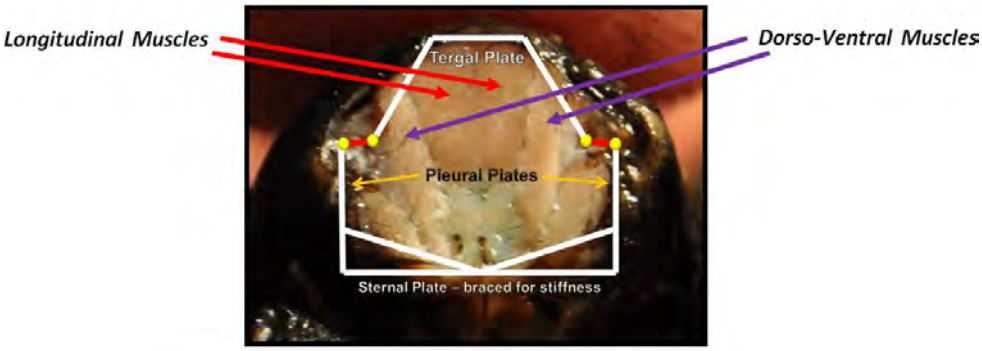

Figure 10 - Specimen cross-section and finite element model geometry overlay. Photo by Tubbs 2011

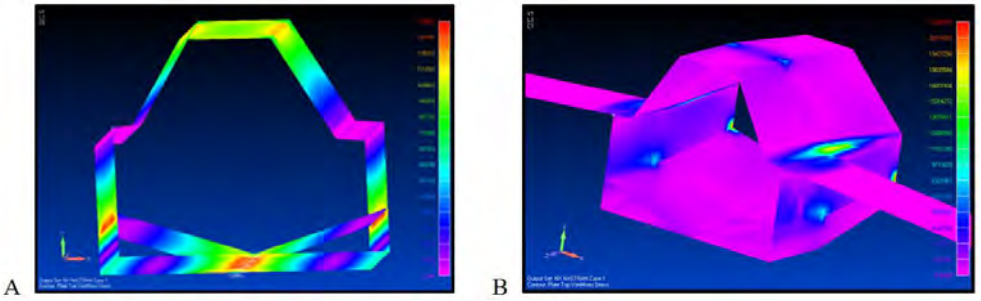

Figure 11 - FE models – **(A)** First model, thin extruded 2D shape, **(B)** Final model, 3D shape

Simplifying assumptions about the hinge allowed the production of a functional model. *M.sexta*, like all flying insects, has a resilin-filled pad of low-modulus, rubber-like cuticle separating the wing base from the hard plates of the thoracic body. This is the same material that stretches and compresses to store much of the elastic forces resulting from the inertia of the flapping wing (Jensen and Weis-Fogh 1962). These highly complex hinge regions contain small, tanned cuticle plates called *sclerites*, to which the small flight control muscles attach. These small muscles make fine adjustments to wing position for stability and control and do not provide significant lift. The simplified nature of this FE model dictated that the sclerites were left out. The hinge regions were modeled by applying low-modulus (several orders of magnitude lower than that of the body/wing material) properties to the finite elements on either side of the wing base (Figure 12).

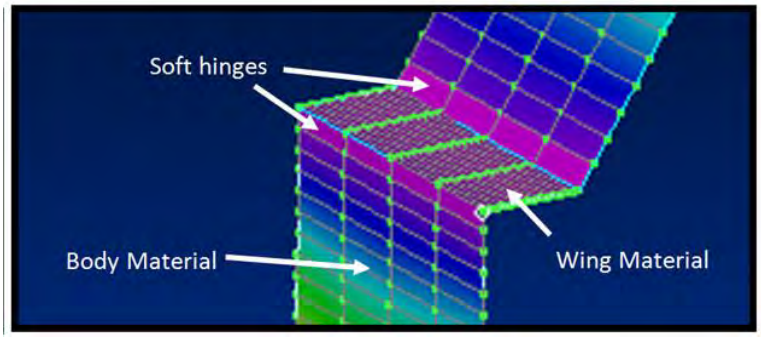

Figure 12 - Wing hinges modeled as soft (low modulus) material

These models resulted in a better understanding of the interaction between the thorax and the wings. Figure 13.a shows the model in an undeformed position before the application of a vertical compressive force on the tergum. Figure 13.b shows the deflection caused by the application of a distributed downward force on the tergum, simulating the action of the DVMs. Figure 13.c shows the position of the wings during the force application.

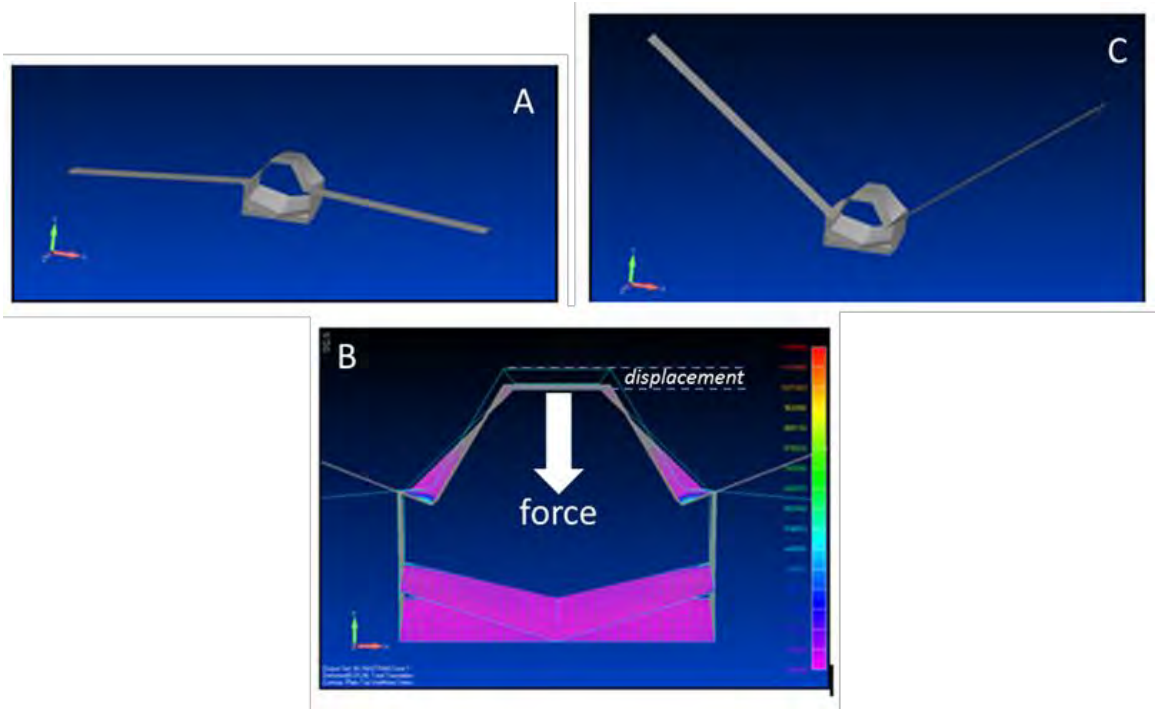

Figure 13 - Realistic wing deflection in FE Model: **(A)** Undeformed, **(B)** Application of force representing DVMs, **(C)** Resultant wing elevation

2.3. Nanoindentation for Elastic Modulus of Biological Materials

Nanoindentation has its roots in the concept of determining material hardness by scratching one material with another, a concept first described by Moh's scale of hardness. Eventually, mathematical solutions concerning the stress state of a hard material pressing into a softer material came along as more sophisticated experiments were developed (Ramesh 2009). Vickers, Knoop and Brinell are all measures of hardness that stem from the concept of indentation for determining material properties. The mathematics and theory of nanoindentation are discussed in Chapter 3 of this document.

Useful results from nanoindentation experiments require measurement of extremely small forces and displacements with great accuracy and sensitivity. Oliver and Pharr pioneered the effective use of a small-scale version of the standard indentation test (Oliver and Pharr 1992). Nanoindentation had been around for a decade at that point, but the results had not been as precise or repeatable as other, more established methods for testing material properties. One of the most significant contributions of their work was the realization that the unloading curve of the load-displacement plot was not linear, as had previously been assumed (Figure 14).

2.3.1. Nanoindentation of Insect Cuticle

The mechanical properties of the insect cuticle material have been of interest for decades. As the most structurally significant component of an insect's body, the cuticle is an engineering marvel with a diverse list of functions:

> *[T]he cuticle…has to perform all the functions of a skin and a skeleton, and that at low weight. The cuticle is, preternaturally, multifunctional: it not only supports the insect, it gives it its shape, means of locomotion, water-proofing and a range of localized mechanical specializations such*

as high compliance, adhesion, wear resistance and diffusion control. It can also serve as a temporary food store and is a major barrier to parasitism and disease. (Vincent and Wegst 2004)

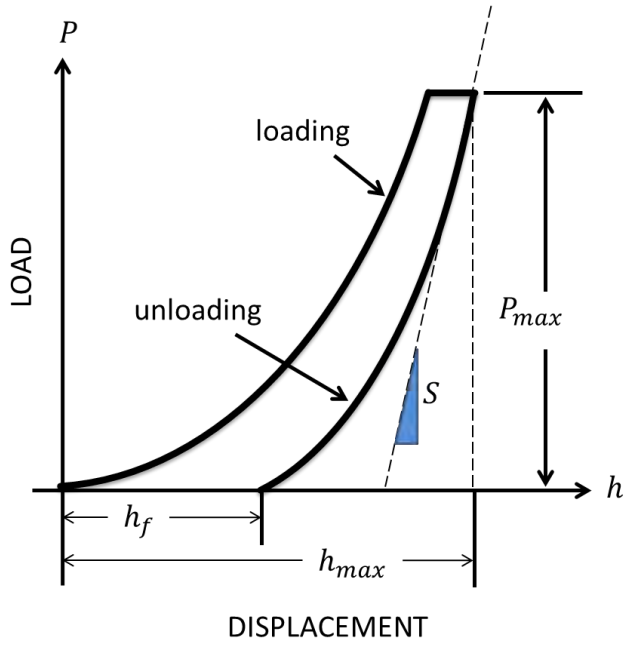

Figure 14 - Schematic of load versus indenter depth into surface for an indentation experiment. P_{max}: indentation load; h_{max}: indenter displacement at peak load; h_f: the final depth of the contact impression after unloading; and **S**: the initial unloading slope.

Engineers can look to insects to gain valuable knowledge about functional integration, which is especially applicable in the world of MAV design. The various sensors, flight controls, energy sources and circuitry will all need to be integrated into a small package with enough room left over for a payload. It currently seems unlikely that all of these components can be designed to fit in or on a stand-alone fuselage that is not integrated with these functions. Additionally, provisions for inertial energy storage during flapping will probably be necessary, as it is apparent that most large insects would not be able to fly without inertial power storage (Ellington 1984). Understanding how *M.sexta* accomplishes functional integration and inertial power storage will aid engineers' efforts at designing an effective FWMAV.

The relation of the flight of a locust to the mechanical properties of its cuticle had been investigated long before the advent of nanoindentation (Jensen and Weis-Fogh 1962). Though it was well-acknowledged that elasticity of the cuticle plays at least a partial role in insect flight, no relevant research had been done prior to Jensen and Weis-Fogh regarding the elastic properties of any arthropod cuticle. These researchers used tensile and compressive tests to examine both the hard cuticle and the soft, rubber-like cuticle of a locust, arriving at an elastic modulus for the hard material of between 8 and 10 GPa, consistent with modern data.

Although these researchers were able to obtain accurate results, the use of nanoindentation would have streamlined their research. More modern studies have already made use of this technique for examining the material properties of the cuticle. A few of these studies have focused on the specialized cuticle which forms the articulating joint between the thorax and the head of the beetle *Panchnoda marginata* (Enders, et al. 2004), (Barbakedze, et al. 2006). These efforts produced significant insight into the effects of desiccation on the hardness and elastic modulus of insect cuticle. The hardness and modulus of that highly-flexible, low-modulus articulating cuticle both increased significantly with desiccation. Water had comprised 15-20 percent of that component's mass prior to drying. It is interesting to note that the elastic modulus of the fresh cuticle was found to be 1.5 GPa, which is much lower than the modulus of *M.sexta*'s tergum at 5 GPa (see Chapter 5 of the present work). It is likely that the hinge material at the base of *M.sexta*'s wings exhibits similar material properties to the *P.marginata* articulation cuticle.

2.4. Power Estimation and Measurement

Flapping flight is more energetically demanding that the standard fixed-wing variety with which aeronautical engineers are most familiar. The demand for actuators with a high power density is further reinforced by the weight and size constraints of a FWMAV. Evaluations of the power requirements of natural flappers like *M.sexta* provide an order-of-magnitude goal for FWMAV developers. Methods for calculating and measuring energetic input and output of flying insects have been around since the 1970's, while research on the energetic properties of the flight muscles dates back to the 1950's (Weis-Fogh 1956). Mechanical power output ($P_{o,m}$) is defined as the sum of the *inertial power* ($P_{o,i}$) and the *aerodynamic power* ($P_{o,a}$) required for hovering flight. $P_{o,i}$ is the power needed to oscillate the wings through each wingbeat, though the actual net value depends on the amount of elastic storage present (Ellington 1985). Perfect elastic storage means that there will be no inertial power requirement ($Po, i = 0$). $P_{o,a}$ can be further broken down into profile, induced, and parasite power, which are detailed by Casey and will not be closely examined here (Casey 1981). He provides a diagram (Figure 15) of the energy expenditure pathway of a flying insect.

Theoretically, if all of the energy from the rotating wing mass is stored in the stretching flight muscles and bending thoracic exoskeleton, then there exists perfect elastic storage. In this case the mechanical power is simply equivalent to the aerodynamic power requirement: $P_{o,m} = P_{o,a}$. On the other extreme, zero elastic storage would mean the wings would have to be slowed down, stopped, and accelerated at each half-stroke maximum (maximum angles above and below horizontal) by the action of the flight muscles alone, which would greatly increase the total mechanical power output required

in large flyers like *M.sexta*. The reality is that elastic storage lies between these two extremes (Ellington 1985).

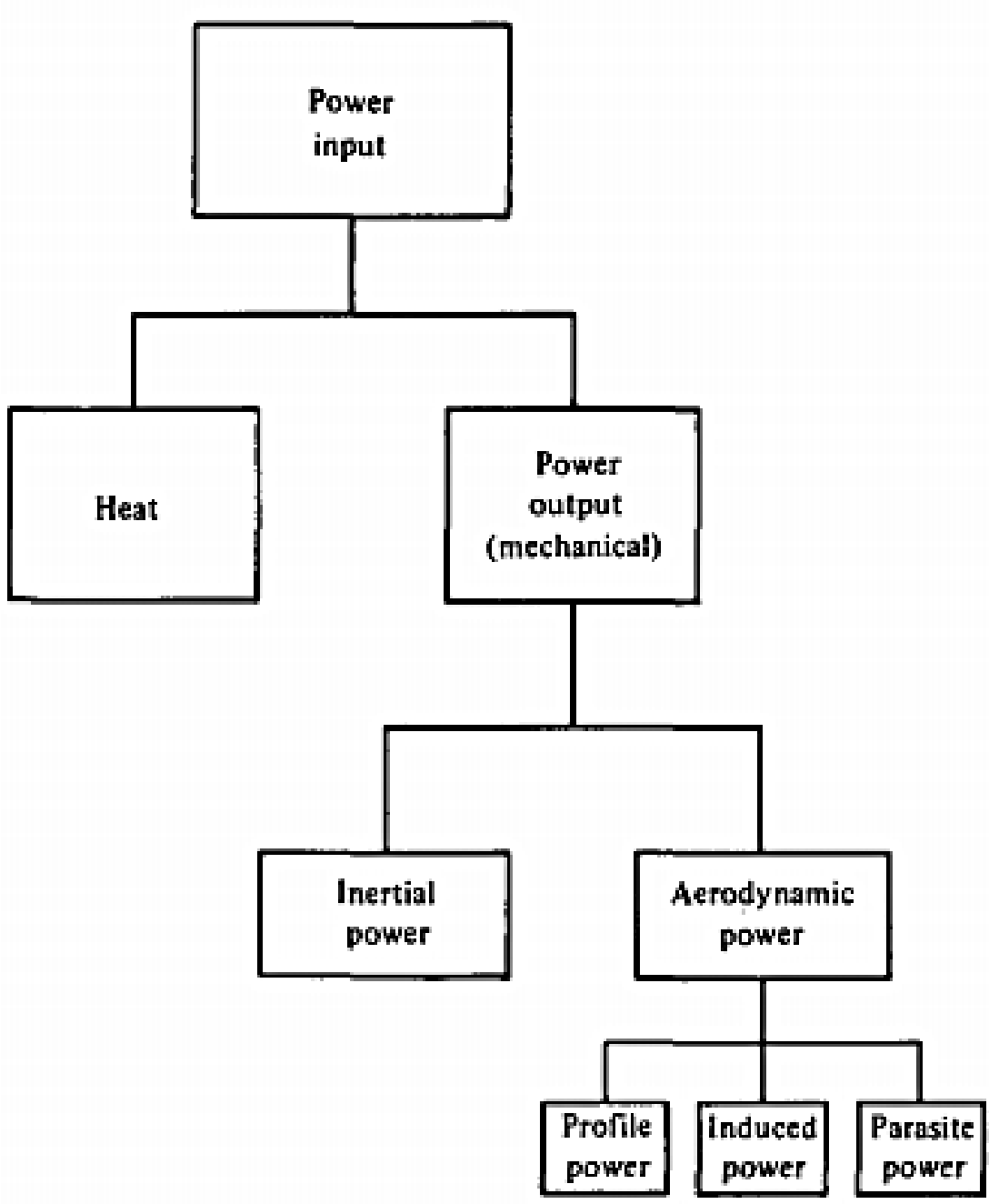

Figure 15 - Pathway for energy expenditure of a flying insect. The inertial power is required to overcome the momentum of the wings in order to flap. The aerodynamic power is the combination of all aerodynamic forces against the movement of the wings. Parasitic power is negligible for hovering. Induced power accelerates the air through the wing disc. Profile power overcomes the wing drag. (after (Casey 1981))

$P_{o,m}$ can also be estimated by dividing the required metabolic power input (P_i) by the muscle efficiency (E_m). Estimates for muscular efficiency in insects are based on measurements of oxygen consumption which can be related to energy expenditure or power requirement and compared with the measured or estimated mechanical power output. The metabolic power input requirement for *M.sexta* in hovering flight has been reported as 237 $W*kg^{-1}$ body mass (Casey 1976) and 1170 $W*kg^{-1}$ muscle mass (Stevenson and Josephson 1990). Ellington used this method and the aerodynamic/inertial summation and compared the $P_{o,m}$ results to gain insight into the nature of the elastic storage (Ellington 1985).

Ellington then concludes that the evidence for elastic storage is high, which meant that the efficiency of the flight muscles was much lower than previously thought, around 5-8 percent assuming perfect elastic storage. That value increased to 11-17 percent if elastic storage was entirely neglected. Previously accepted values for insect muscle efficiency were between 20 and 30 percent (Ellington 1985). However, other estimates of the power output of insect muscle, based on the wingbeat frequency, have been set forth (Pennycuick and Rezende 1984). These researchers directly studied the physical construction of muscle fibers and were able to correlate the specific power output with the contraction frequency, which is the same as the flapping frequency for insects like *M.sexta* that have synchronous muscle fibers. Their method yields an estimated power output of approximately 82-97 $W*kg^{-1}$ (muscle mass) for *M.sexta*, whose wingbeat frequency is between 25 and 30 beats per second (shown as intersecting blue rectangles drawn over the plot in Figure 16). Their higher estimation of power output meant that E_m

for insect flight muscle would be between 11 and 17 percent with perfect elastic storage (Ellington 1985).

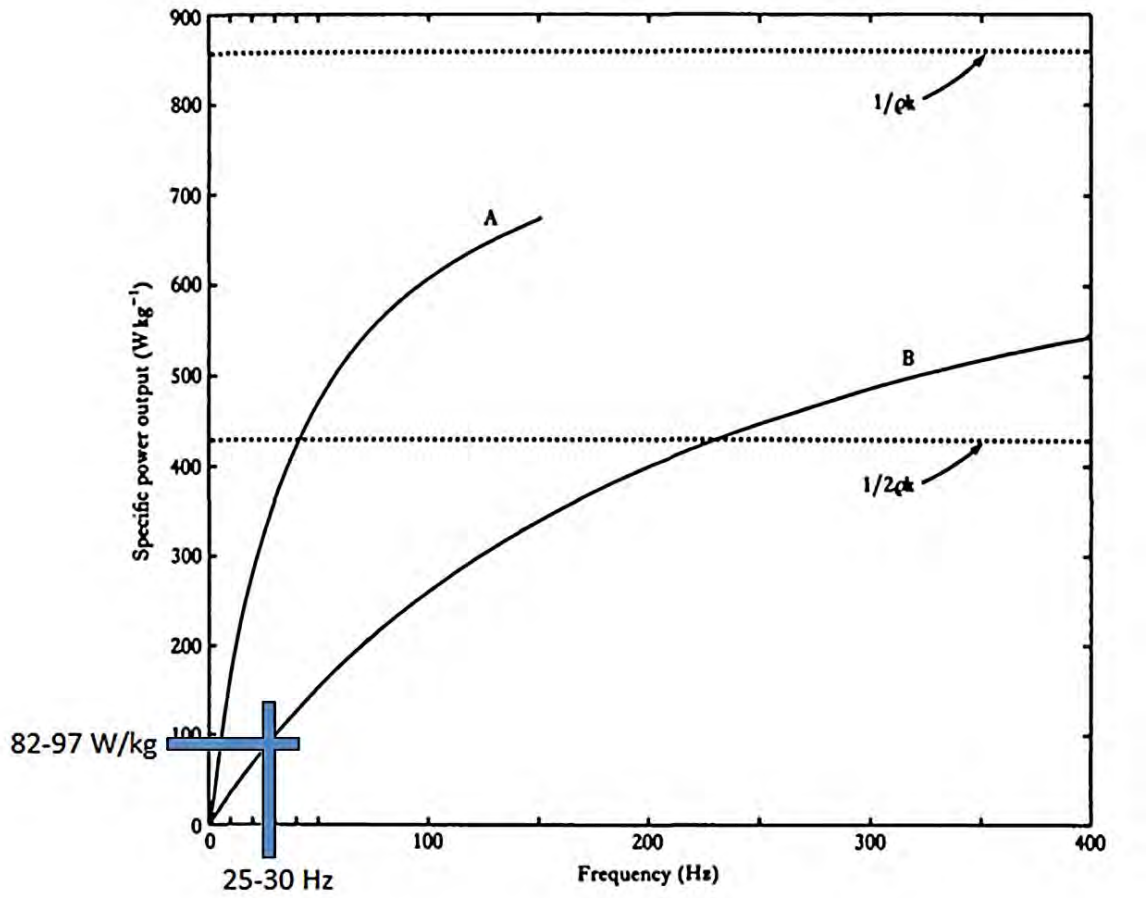

Figure 16 - Specific power of non-fibrillar (striated, vertebrate) flight muscle **(A)** and fibrillar (synchronous, insect) flight muscle **(B)** versus flapping frequency. *M.sexta* flaps at a frequency of 25-30 Hz, which covers a power output range of 82-97 $W*kg^{-1}$ (represented by the blue rectangles drawn over the plot). The upper dotted line is the asymptote for both curves and the lower dotted line corresponds to equal volumes of mitochondria and myofibrils. Adapted from (Pennycuick and Rezende 1984)

Mechanical work output of the major flight muscles in *M.sexta* has also been measured using a work loop technique first developed by Machin and Pringle and later adapted for synchronous muscles like *M.sexta*'s by Stevenson and Josephson (Machin and Pringle 1959), (Stevenson and Josephson 1990). Using electrical stimulation and an imposed sinusoidal length change, Stevenson and Josephson determined that the DVMs

of *M.sexta* produce an average maximum power output of 90 $W*kg^{-1}$ at a temperature range of 35-40 °C. This measurement fits well with the rest of the data available for power output of insect muscle as well as with the ideal internal thoracic temperature of *M.sexta*'s thorax during flight. A more recent experiment using a similar approach arrived at an average maximum power output of 83.3 $W*kg^{-1}$ for the DLMs (Daniel and Tu 2004). This is consistent with previously measured and estimated values.

Advancements in high-lift generation at low Reynolds conditions have led to increasingly accurate predictions of power requirements in insect flight (Sun 2003). The theory of unsteady high-lift fluid mechanics is described in Sun's paper and will only be briefly mentioned here. Basically, delayed stall, in the form of leading edge vortices held attached by span-wise flow, works as the high-lift device for flapping wings of insects. Pronation and supination of flexible wings can also create rotational circulation and wake capture which creates aerodynamic forces during stroke reversals (Wu, Stanford and Ifju 2009).

Sun and Du computed the specific power requirement of 8 insect species, ranging from fruit fly to hawkmoth, by numerically solving Navier-Stokes equations (Sun and Du 2003). They arrived at a power output for *M.sexta* of 39 $W*kg^{-1}$ (body mass) without elastic storage and 33 $W*kg^{-1}$ with elastic storage. For a *M.sexta* specimen with flight muscles comprising 20% of body weight (Stevenson and Josephson 1990), these values correlate to approximately 164 and 194 $W*kg^{-1}$ (muscle mass) respectively, which is slightly higher than the previous data. They concluded that large insects like *M.sexta* benefit greatly from elastic storage, because a large portion of this power requirement was due to inertial force from the wings (Sun and Du 2003).

Liu and Aono studied the low-Reynolds hovering of insects using a computational method (Liu and Aono 2009). They arrived at a power output of 39.5 $W*kg^{-1}$ (body mass) for a different species of hawkmoth (*Agrius convolvuli*). This correlates to about 197.5 $W*kg^{-1}$ (muscle mass). Their value is based on the aerodynamic power, having determined that the inertial power is minimal. This conflicts with Sun's and Du's result regarding inertial power, which they found to be about 6 $W*kg^{-1}$ or about 20% of aerodynamic power.

Most recently, Zhao and Deng have investigated the aerodynamic and inertial power distribution in *M.sexta* (Zhao and Deng 2009). Known hovering kinematics were combined with forces and torques measured with model hawkmoth wings to calculate the power values. They determined that inertial power requires nearly half of the total power expenditure assuming zero elastic storage. The specific power was determined to be 19.7 $W*kg^{-1}$ (body mass) and 16.4 $W*kg^{-1}$ for aerodynamic and inertial forces, respectively. This means that if *M.sexta* stores a large portion of this inertial power with elastic action, the power output should be close to 20 $W*kg^{-1}$ (body mass) or 100 $W*kg^{-1}$ (muscle mass). If the moth must overcome all inertial forces, these results require a power output of 36.1 $W*kg^{-1}$ (body mass) or 180 $W*kg^{-1}$ (muscle mass). All of the power output and input (consumption) values reported in this chapter are summarized in Table 1 and are repeated in Chapter 5 with the results of the present research.

The research work performed for this thesis involved measuring the actual aerodynamic and inertial power required to replicate the wing-elevating portion of the wingbeat using fully-intact *M.sexta* specimens, which will provide insight into the true mechanical power output ($P_{o,m}$) of the DVMs.

Table 1 - Summary of power density estimations for the hawkmoth *M.sexta*. Some researchers reported their results as power per body mass. These have been converted to power per muscle mass by assuming a flight muscle to body ratio of 20% [19]. The power per muscle mass numbers indicated in bold font are the most pertinent values for this study, as they have been obtained directly from analyses of the flight muscles. The power input is also presented below. Stevenson and Josephson report power consumption based on metabolic analysis of the hawkmoth in flight and the 20% flight muscle to body mass ratio. Theirs is likely the most accurate power input value.

***M.sexta* Power Output**		**power density ($W*kg^{-1}$)**		
researcher/year	**method**	**body mass**	**muscle mass**	**notes**
Casey 1976	estimation from power input	41-54	*205-270	Based on measurements of power input and estimate of 20% efficiency. We now know that actual efficiency is much lower
Pennycuick, Rezende 1983	muscle study	-	**82-97**	Estimated power density of muscle based on a known value for power density of mitochondria
Stevenson, Joesephson 1990	work-loop	-	**90**	Mean maximum power. Absolue max reached 130 in two specimens. 50-80 determined to be min. power req'd for flight
Sun, Du 2003	numerical	33-39	*164-194	With elastic storage - without elastic storage
Tu, Daniel 2004	work-loop	-	**83.3**	Specifically studied the DLMs
Liu, Aono 2009	computational	39.5	*197.5	Diff. species of hawkmoth, *Agrius convolvuli*
Zhao, Deng 2009	kinematics and aerodynamics	19.7 (aero) 16.4 (inertial)	*98-180	With elastic storage (no inertial power) - Without elastic storage (must overcome all power requirements)

*indicates equivalent value based on 20% muscle mass

***M.sexta* Power Input**		**power density ($W*kg^{-1}$)**		
researcher/year	**method**	**body mass**	**muscle mass**	**notes**
Casey 1976 (Reporting Heinrich 1971)	metabolic	191-289	478-722	Moth flies in closed jar and depletion of oxygen is measured/correlated to energy by assuming fat utilization during flight
Casey 1976	metabolic	237	694	Based on oxygen consumption
Stevenson, Joesephson 1990	metabolic	-	**1170**	Derived from Heinrich's 0_2 consumption. Most reliable number based on newer data

3. THEORY

Physical and mathematical theory behind the present investigations of the energetics of hawkmoth flight are detailed in this chapter. Section 3.1 explains the concepts relevant to the first experiment, which involved the evaluation of the thorax as a mechanical spring system. Work, or the amount of energy put into the system with a given force and displacement, was a key element of this phase of the project. The following section (3.2) defines and describes power, or work performed over time, the calculation of which is the end result of the dynamic force application experiment. Finally, the theory and mechanics of nanoindentation are presented in detail (3.3) as they relate to characterization of the elastic modulus of a material as a function of indentation depth. This procedure was performed on the tergum of *M.sexta* in the third experiment.

3.1. Static Force and Work

The idea of relating the compression of the thorax to wing elevation, and measuring both for the calculation of energy requirements, originated with Tubbs when he demonstrated that the wings elevate when the thorax is vertically compressed (Figure 17) (Tubbs 2011). He surmised that this change in wing angle could be used to determine the amount of energy, or work, needed to compress the thorax through a given displacement and cause a certain wing elevation. His work in this area was limited but still provided the impetus for two of the experiments carried out in this project. One especially important note is that this process was static, that is, the wing was held in position by a constant force and displacement. Therefore the dynamic energetics of flapping wings did not factor into the calculations.

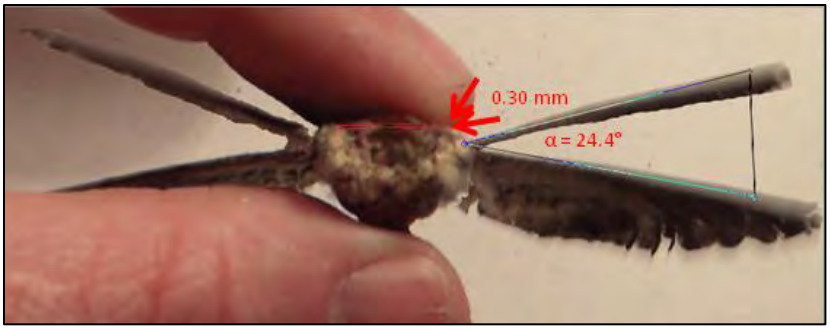

Figure 17 - Two images superimposed to show thoracic compression and wing elevation angle (from (Tubbs 2011))

3.1.1. Spring Constant

The present work expands the scope of Tubbs' preliminary research by conducting a thorough investigation of the thorax/wing mechanism both statically and dynamically. The first experiment was very similar to the original squeezing of the thorax. However, while Tubbs calculated the energy required to move the wings based on the displacement of their center of gravity, this experiment concentrated on the compression of the thorax itself. Figure 18 shows a schematic of this concept.

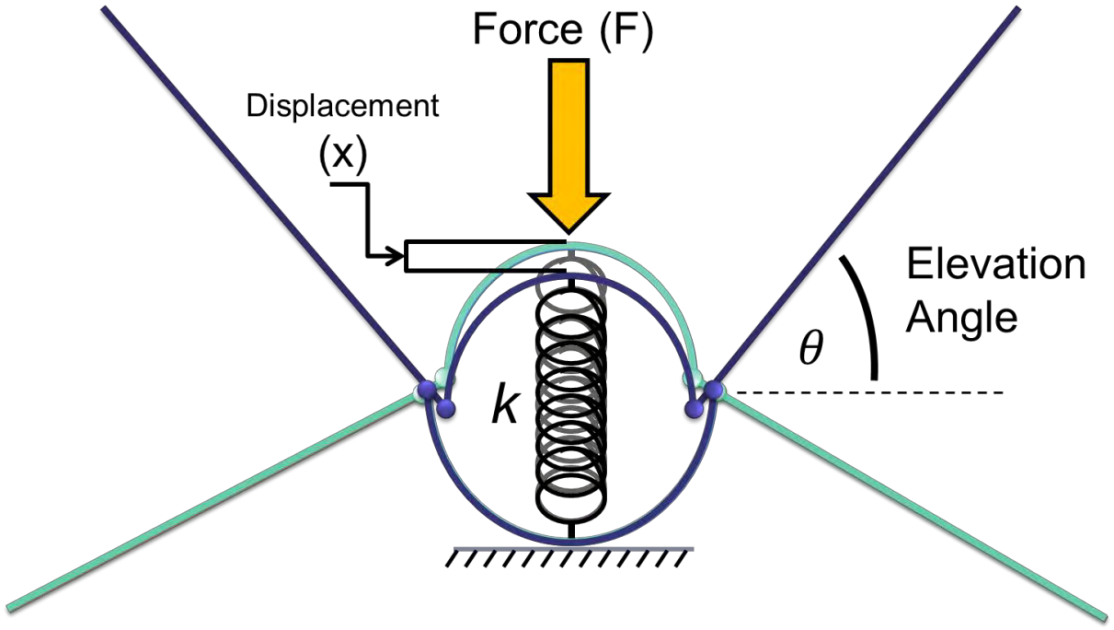

Figure 18 - Schematic of the thorax as a mechanical system with spring

If the base of the thorax, the sternal plate or sternum, is considered to be fixed, the compression of the entire thorax is represented by the vertical displacement x of the tergum. The resistance of this entire system to that compression can be modeled by a simple, linear spring inside the thorax, as in Figure 18. A force F applied vertically downward at the center of the tergum will compress the thoracic box, but the compression of the muscles, stretching of the tergum and the weight of the wings will resist this motion much like a spring resists compression. Correlating the applied force and subsequent displacement provides insight into the nature of the system by producing a spring coefficient k. If this correlation is linear, then the system has a constant value k for any given F and x found simply by:

$$\mathbf{F} = \boldsymbol{k} \cdot \mathbf{x} \qquad (1)$$

3.1.2. Work

Work (denoted in this document by italic W), measured in joules, can be calculated by determining the area under the curve of a force versus displacement plot. It can be physically described as the product of a force multiplied by the distance or displacement over which that force was applied (Figure 19). A function of force in terms of distance can be integrated to determine the work performed:

$$\boldsymbol{W} = \int_{x_1}^{x_2} \boldsymbol{F}(\boldsymbol{x})\boldsymbol{dx} \qquad (2)$$

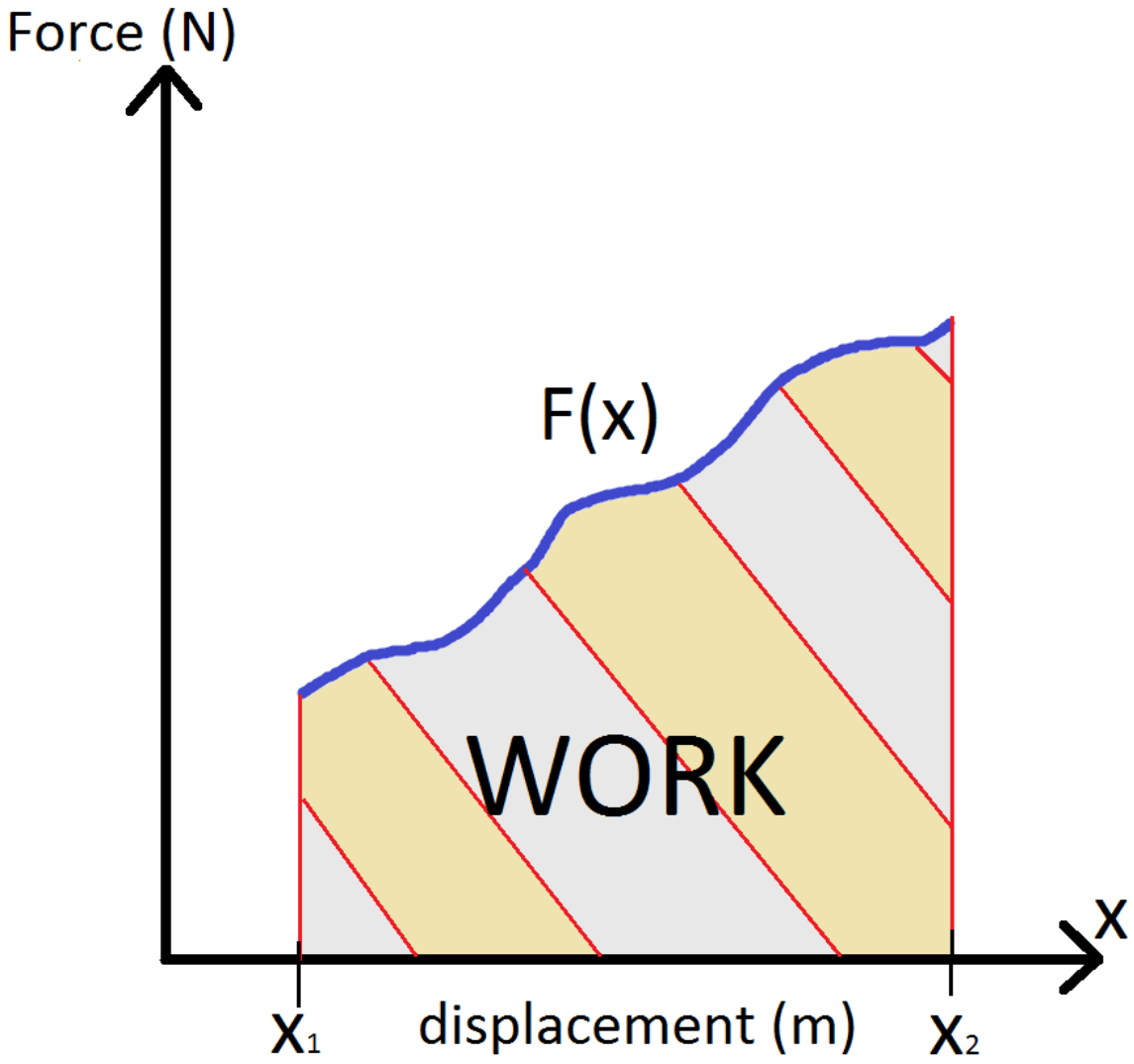

Figure 19 - Work as the area under a force versus displacement curve

If the force curve is linear (Figure 20) then the formula for work simply becomes:

$$W = \frac{F_1 \cdot x_1}{2} \qquad (3)$$

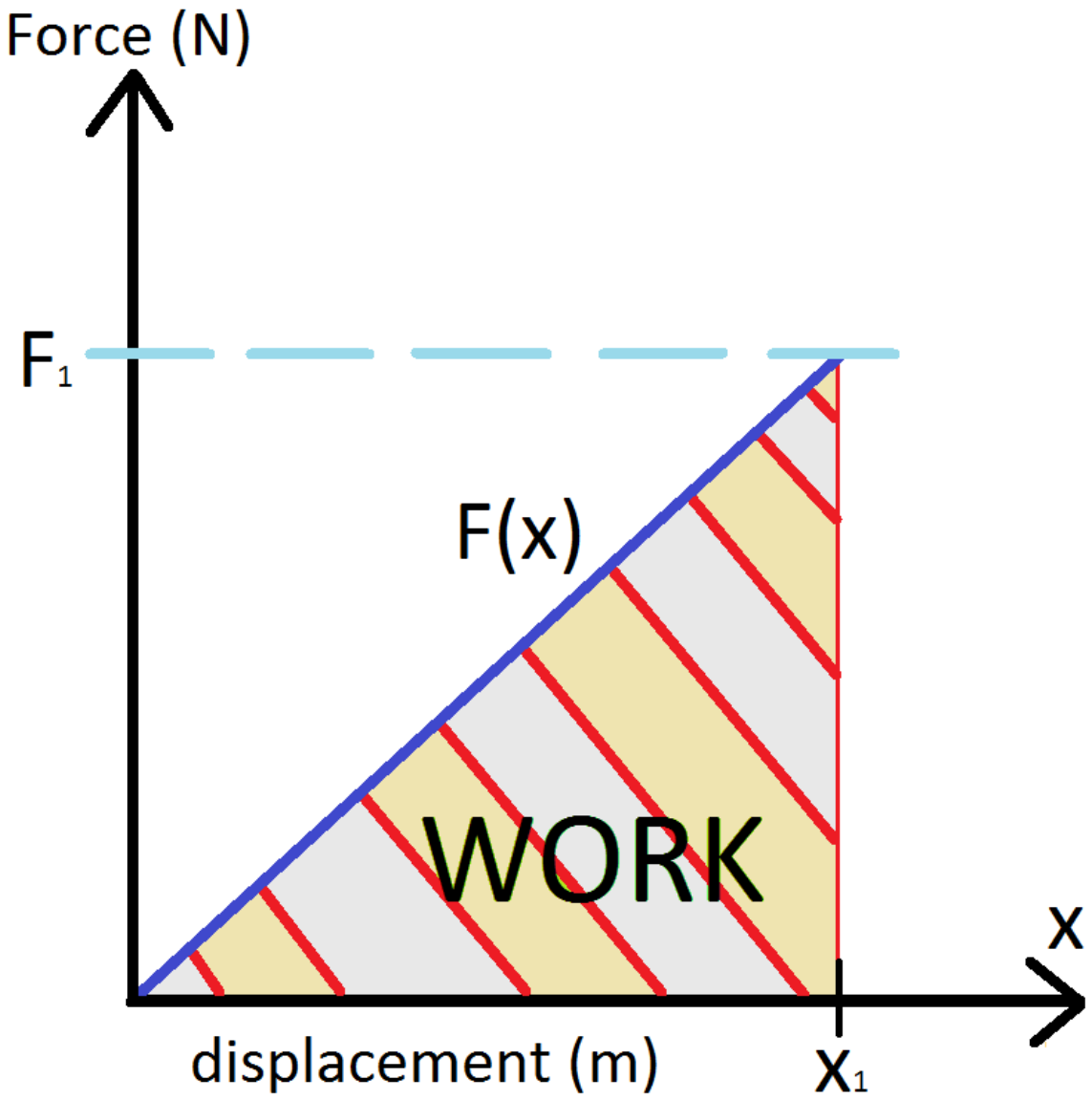

Figure 20 - Work as the area under a linear force versus displacement curve

3.2. Power

Power can be thought of as the time rate of doing work. The unit of power used throughout this thesis is the watt (non-italicized W, not to be confused with *W* used for work). One newton is equivalent to one kilogram (kg) multiplied by one meter per second squared. Therefore, the watt can be symbolically expressed in multiple ways:

$$\textbf{Watt (W)} = \frac{\boldsymbol{Work}}{\boldsymbol{time}} = \frac{\boldsymbol{J}}{\boldsymbol{s}} = \frac{\boldsymbol{N \cdot m}}{\boldsymbol{s}} = \frac{\boldsymbol{kg \cdot m^2}}{\boldsymbol{s^3}} \quad (4)$$

Calculating power after the work value has been determined is as simple as dividing that work by the amount of time over which the work was performed (Δt). In general:

$$\boldsymbol{P} = \frac{\int_{x_1}^{x_2} \boldsymbol{F(x)dx}}{\boldsymbol{\Delta t}} \quad (5)$$

If the force varies linearly with displacement, then the calculation for power becomes:

$$\boldsymbol{P} = \frac{\boldsymbol{W}}{\boldsymbol{\Delta t}} = \frac{\boldsymbol{F_1 \cdot x_1}}{\boldsymbol{2 \cdot \Delta t}} \quad (6)$$

This concept can be used to evaluate the mechanical power output of the *M.sexta* thorax. Refer back to Figure 18 (pp.31), and let the force, instead of being held statically against the tergum, be applied 25 times per second (the approximate frequency at which *M.sexta* flaps (Willmott and Ellington 1997), (Sun 2003). Real-time measurements of the compression of the thorax, the force applied to the thorax, and the time in which this compression occurs during each simulated wingbeat enables the calculation of the mechanical power output of *M.sexta* subject to realistic hovering dynamics. This is the objective of the dynamic load experiment, which appears to be the first physical analysis of the entire hawkmoth thorax and wing system (or that of any insect) from a mechanical perspective. The results compare favorably with previously published data obtained

through mathematical modeling and biological investigations of the musculature, indicating the likelihood that this new method is worthy of pursuit for further research (see results and conclusions in Chapters 5 and 6, respectively).

3.3. Nanoindentation for Elastic Modulus of the Tergum

The content of the following section on nanoindentation theory, unless otherwise specified, is derived from a combination of the Nano Indenter® G200 system user's manual (MTS 2007) and two highly-informative papers by Hay and her associates (Hay 2009), (Hay, Agee and Herbert 2010). The Nano Indenter® G200 machine was used throughout this research project, so its manual is referenced here for information pertaining directly to that particular machine. The papers by Hay and Hay et al. are excellent summaries of basic indentation theory and the more specific area of continuous stiffness measurements, respectively. All figures in this section are derived from these three sources unless otherwise specified.

3.3.1. Basic Indentation Process

An indenter, which has a significantly higher modulus and lower Poisson ratio than the specimen, causes a material to deform both elastically and plastically. The result is a hardness impression which conforms to the shape of the indenter tip down to a contact depth h_c. Withdrawing the indenter allows the material to recover the elastic displacement, though the plastic displacement (if any) remains as residual impression of the indenter tip (Figure 21). The parameters of this indentation are shown in Figure 22.

A traditional hardness test, which involves pressing an indenter into a material at a given force, measures only one value of deformation at that one applied force.

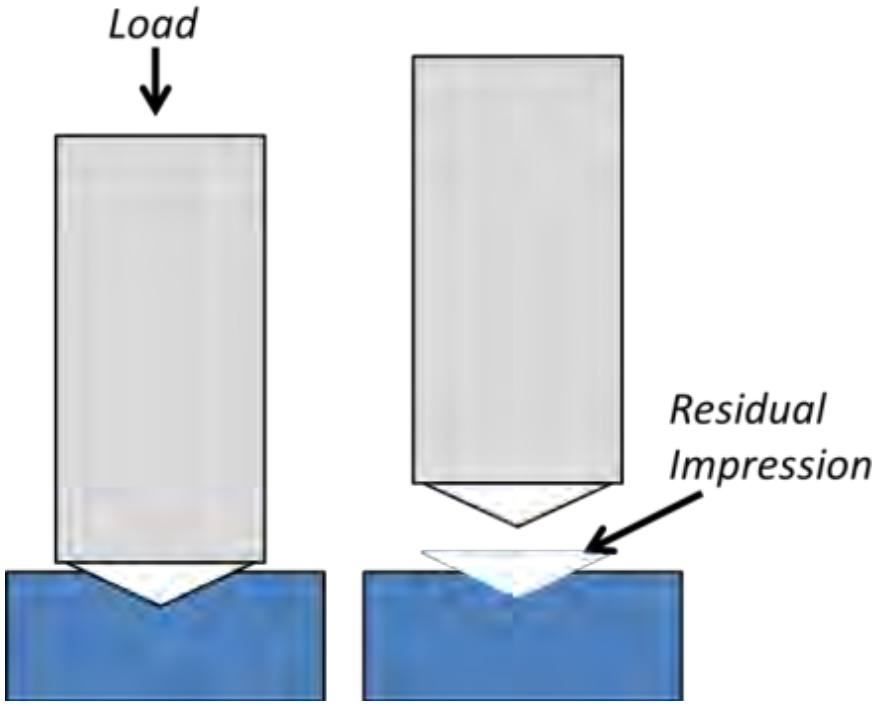

Figure 21 - Basic Indentation Test

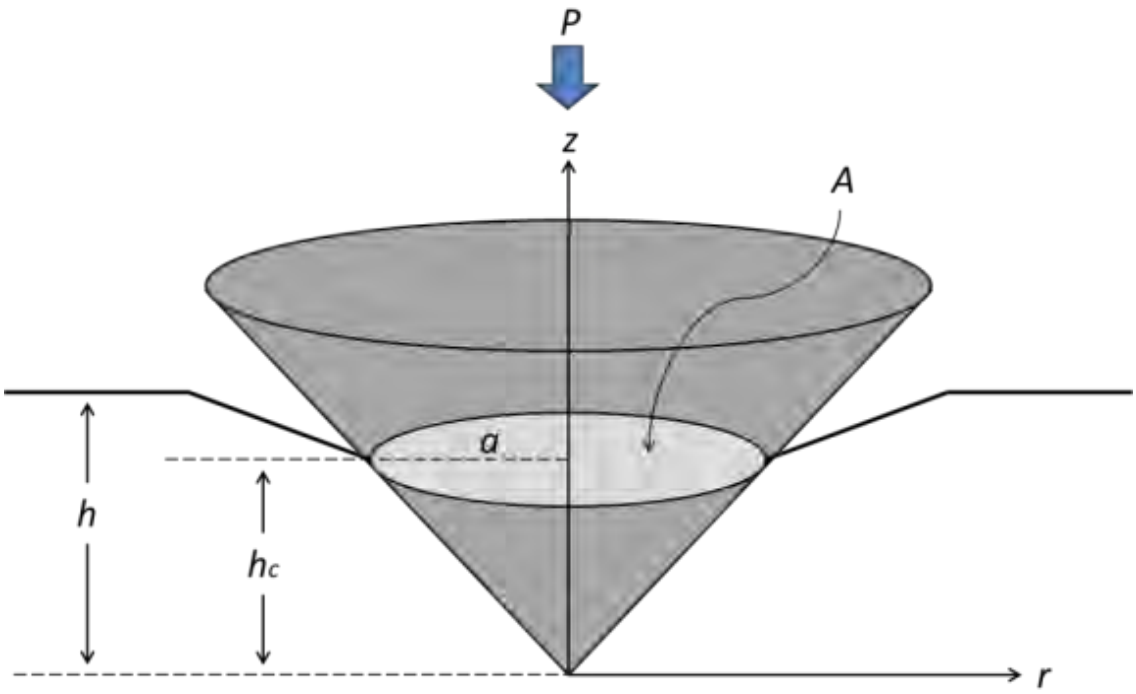

Figure 22 - Schematic of an indentation test. The projected contact area is *A*. *P* is the applied load. *h* is the penetration depth as measured from the surface, and *hc* is the depth of actual contact between the indenter and the specimen.

Automation of this test is called Instrumented Indentation Testing (IIT). IIT enables measurement of penetration and force throughout the duration of the contact between the indenter and specimen. This kind of testing is especially effective on a small scale and is used to determine material properties of thin films and small objects. This is the driving concept behind nanoindentation, or the technique of measuring the material properties of a specimen using extremely small (on the order of nanometers) and precise movements with sensitive equipment.

3.3.1.1. Typical IIT Test Chronology

A typical IIT test consists of a six step process. Figure 23 is a plot of a typical force-time history and is labeled with numbers corresponding to the following test segments:

0. The indenter is slowly lowered until the device senses that contact with the specimen has been made. This point is determined by a change in the stiffness of the system caused by contact with the specimen. The detection sensitivity and the approach rate are set by the user.

1. The indenter is then pressed into the material to either a maximum force or maximum distance specified by the user. The rate at which the force or displacement increases is also a user input.

2. Once the specified load or displacement is reached the indenter is held at a constant force for a dwell period. This is also a user-defined variable and usually lasts for 20-30 seconds. The displacement will continue to increase under this constant force.

3. The indenter is then withdrawn at a rate similar to the pressing rate until the load has reached about 10% of maximum.

4. Another dwell time, this one lasting about 60 seconds, is then performed in order to aquire data related to the thermal drift (or thermal expansion/contraction of the specimen/equipment). The amount of thermal drift will be factored into the calculations done by the software to arrive at the hardness and modulus of the specimen. Displacement will increase under this constant load during the dwell period.

5. The indenter is then completely withdrawn from the specimen.

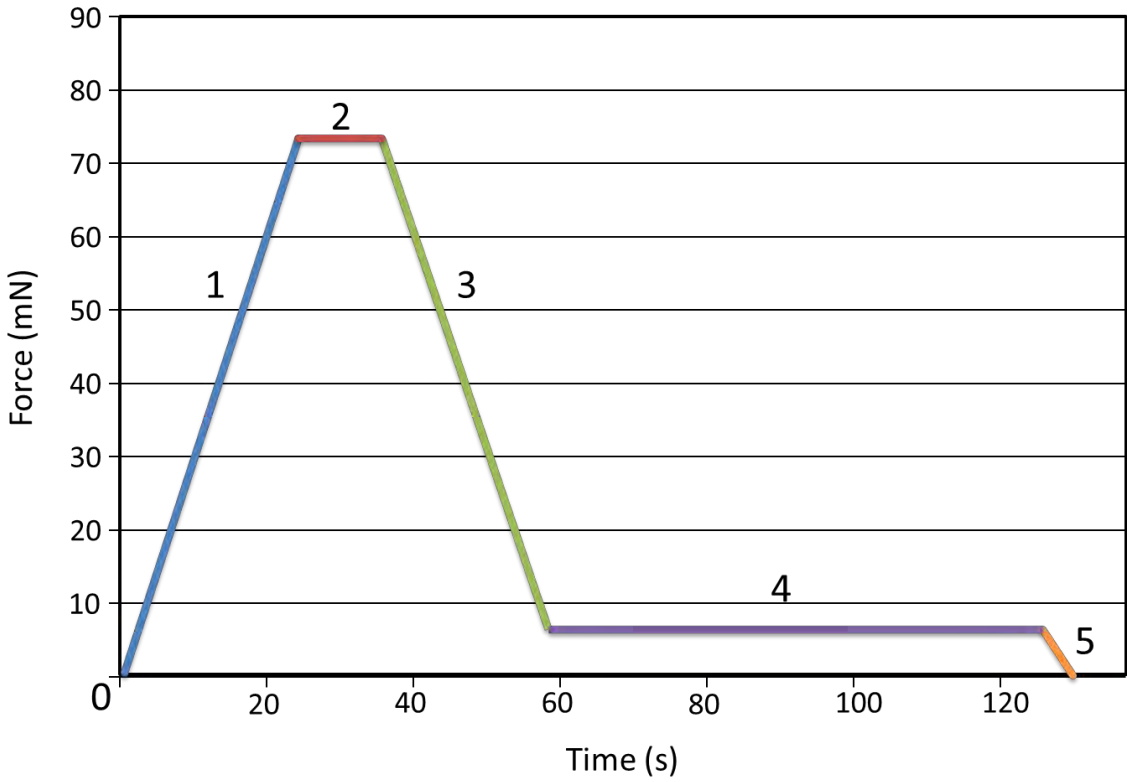

Figure 23 - Representative force-time history for an instrumented indentation test. Contact first occurs at the origin.

3.3.1.2. Load-Displacement Curve

Analysis of the data from the indentation test begins with the creation of a force-displacement plot, an example of which can be found in Figure 24. Just like the force-time history plot, the stages are labeled and colored to correspond with the test segments. The indenter contacts the surface at the origin of the plot and the displacement and applied force increase until the peak load or displacement is reached. The displacement continues to increase under a constant load during stage 2. The majority of the elastic portion of the displacement is recovered during the 90% unloading phase in stage 3, but for most materials there will be some plastic (permanent) deformation. If the material were perfectly elastic then the unloading curve would coincide perfectly with the loading

curve. If it were perfectly plastic then the unloading curve would be a vertical line and all deformation would be permanent. Stage 4, the thermal drift correction segment, occurs near the end of the test and is used to account for thermal expansion or contraction of the specimen due to the potential heat-loading effects of plastic deformation. The indenter is then withdrawn through the final 10% of elastic deformation in stage 5.

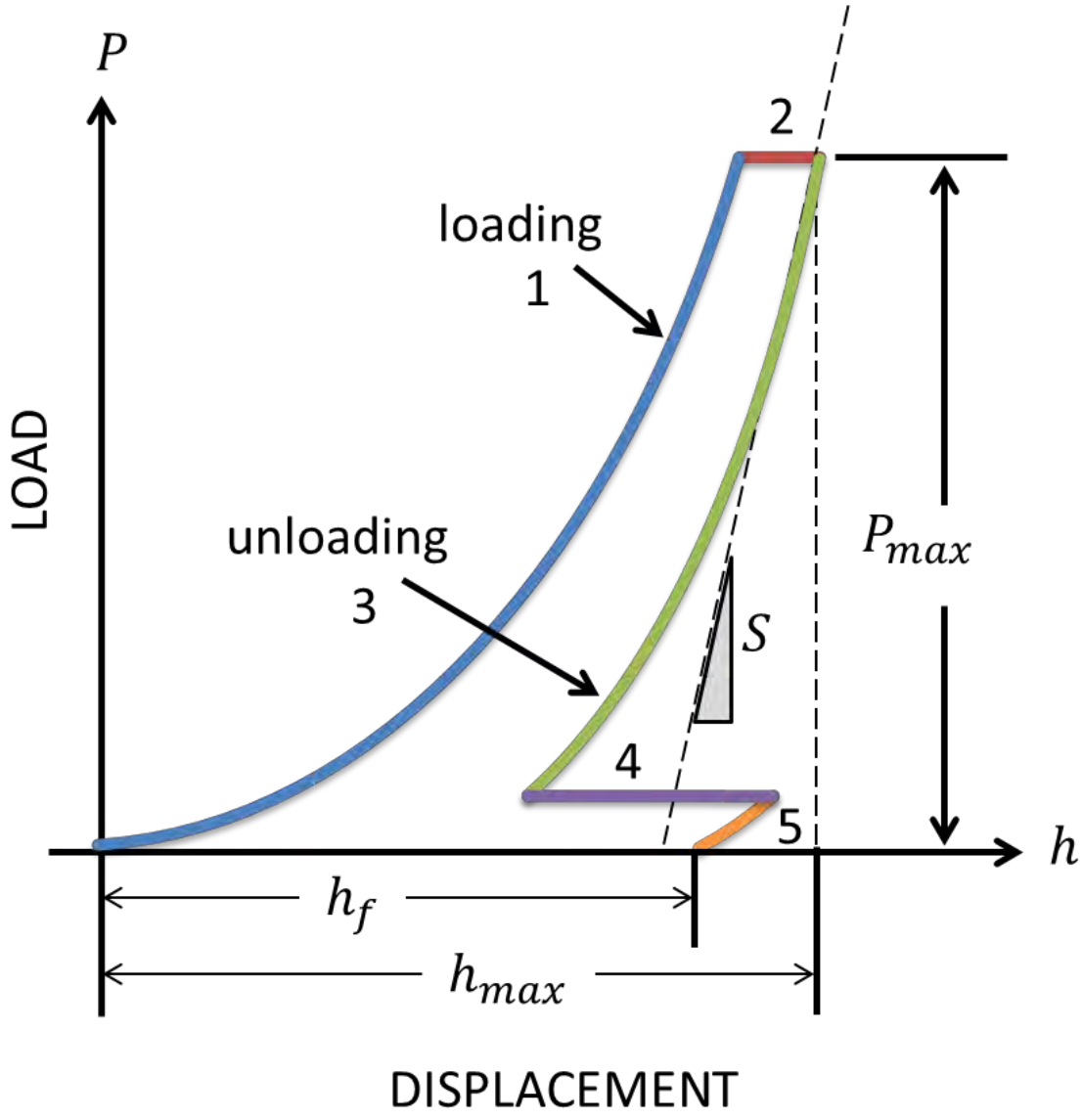

Figure 24 - Typical load-displacement plot for an instrumented indentatino test. The segments are colored and numbered to match their counterparts from the force-time history in Figure 23.

3.3.1.3. Calculating Material Properties

The data from the load-displacement curve is used to calculate the material properties of the specimen. This section begins with the equations for the desired properties (hardness H and elastic modulus E) and then presents the supporting calculations for those equations.

Hardness is found by:

$$\boldsymbol{H = \frac{P}{A}} \tag{7}$$

where P is the applied force and A is the projected contact area (defined in Eqn. 11). The Young's modulus (the modulus of elasticity, E) of the specimen is calculated from the reduced modulus E_r with:

$$\boldsymbol{E = (1 - \nu^2)\left[\frac{1}{E_r} - \frac{1 - \nu_i^2}{E_i}\right]^{-1}} \tag{8}$$

where E_i and ν_i are the modulus and Poisson ratio of the indenter tip, respectively, and ν is an estimated Poisson ratio for the specimen. The reduced modulus E_r is found by the following equation, first proposed by Oliver and Pharr, (Oliver and Pharr 1992)):

$$\boldsymbol{E_r = \frac{(\sqrt{\pi} \cdot S)}{2\beta\sqrt{A}}} \tag{9}$$

where S is the initial slope of the unloading curve, also referred to as the contact stiffness, and β is the slope of the indenter tip.

Although Eqn. 8 requires the Poisson ratio of the specimen (which is often not known) there is very little sensitivity to that value. Estimates of 0.2 for glasses, 0.3 for metals, and 0.45 for polymers are generally sufficient. The reason that the specimen's Poisson ratio is negligible is the disparity between the diamond tip (very high E and very low ν) and the specimen (relatively low E and high ν) (Martin, et al. 2008). Therefore, in relation to the other terms, the rightmost term of Eqn. 8 can be considered negligible, yielding a reduced form:

$$\boldsymbol{E = E_r(1 - \nu^2)} \qquad (10)$$

Eqn. 10 represents a possible simplification of the calculations, but the computational analysis automatically performed by the software makes use of the original, expanded form (Eqn. 8).

The contact area A from Eqns. 7 and 9 is a function of the contact depth h_c:

$$\boldsymbol{A = f(h_c)} \qquad (11)$$

the form of which depends on the geometry of the indenter tip.

One of the most common indenter geometries is the Berkovich Pyramid, shown in Figure 25. It is a three-sided pyramid with approximately the same area function as a four-sided Vickers Pyramid. This research was carried out with a Berkovich indenter made of diamond, which is the most common material for an indenter tip due to its high modulus (1170 GPa) and low Poisson ratio (0.07) (Martin, et al. 2008). There are several benefits attributed to the Berkovich indenter by Hay:

- Well-known mechanical properties
- Robust and durable
- Relatively easy to manufacture (compared to a spherical or cone shaped indenter)
- Induces plasticity under very low loads which is conducive to hardness testing
- Large included angle minimizes effect of friction between the indenter and specimen

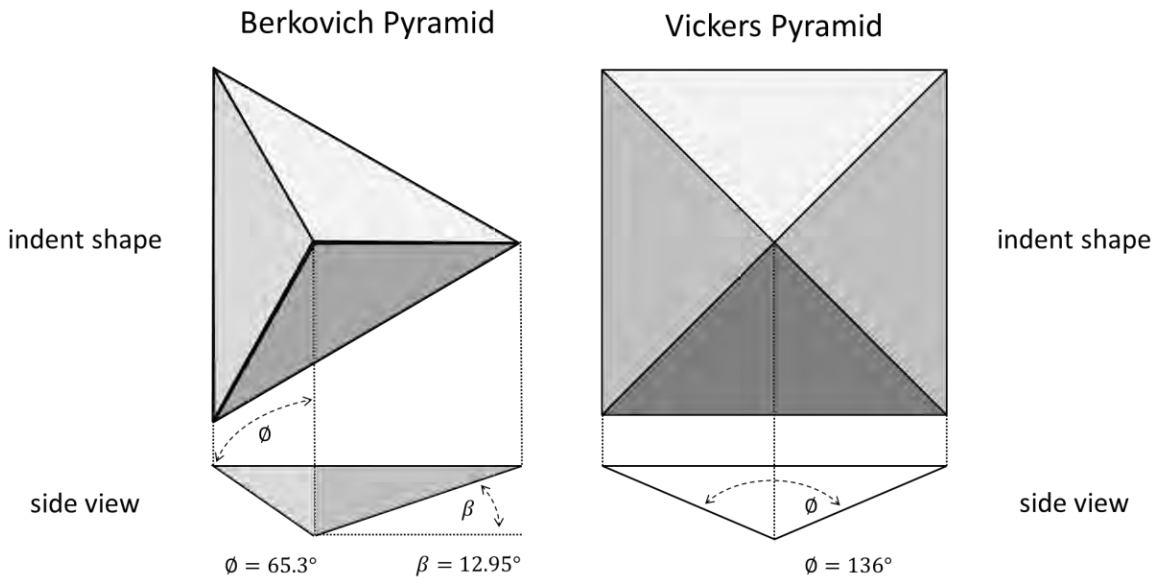

Figure 25 - Pyramidal indenter tips. The Berkovich was used for the experimentation in this research project

According to Hay, an ideal Berkovich indenter has the following area function for indentations of more than 2 microns ($2x10^{-6}$ m):

$$\boldsymbol{A = 24.56 \cdot h_c^2} \qquad (12)$$

A correction factor must be included to account for rounding at the apex of the indenter if the depth of indentation is less than 2 microns. In other words, the geometry

can no longer be assumed to be ideal for such small and sensitive indentation tests. The area-function calibration constant C is determined empirically by indentation of a material with known properties such as fused silica. The area function equation then becomes:

$$\boldsymbol{A = 24.56 \cdot h_c^2 + Ch_c} \qquad (13)$$

The value of C for a Berkovich indenter is around 150 nm. The area functions for other geometries and their calibration constants are compiled by Hay, (Hay 2009).

The contact depth h_c must be known in order to use Eqns. 12 or 13. This is the depth of physical contact between the indenter tip and the specimen, as opposed to the absolute depth from the surface, h (Figure 26).

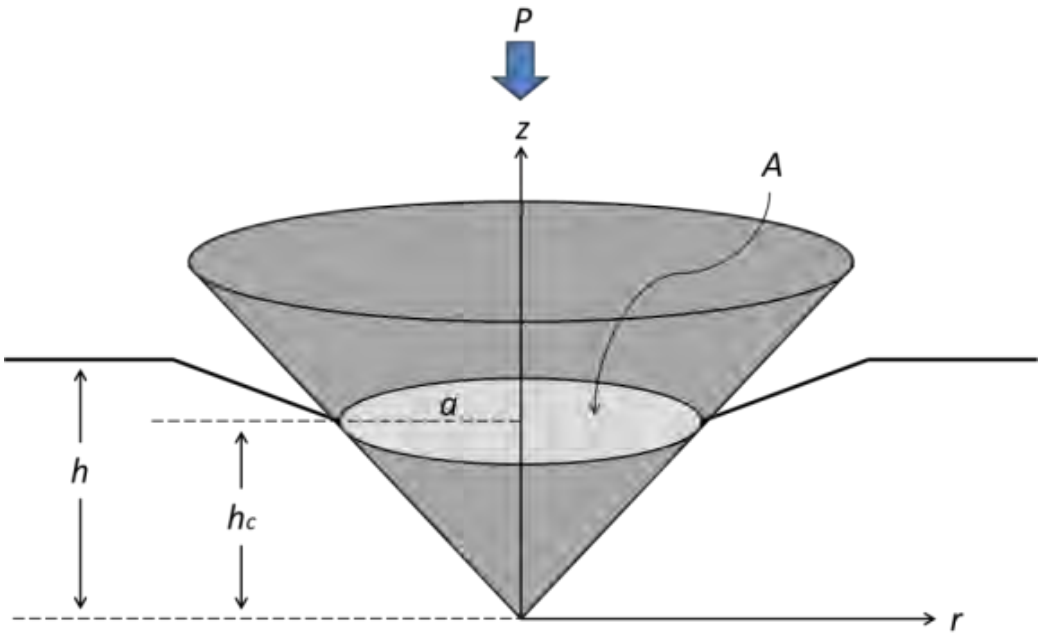

Figure 26 - Schematic of indentation contact parameters

The contact depth for conical, spherical and pyramidal indenters is calculated with:

$$h_c = h - 0.75\frac{P}{S} \quad (14)$$

The contact stiffness S is the relationship between displacement and force during the entirely elastic portion of step three, that is, when the indenter is first being retracted from the sample. Its value is derived from the data of the load-displacement curve using the following power law relation (Oliver and Pharr 1992):

$$P = B(h - h_f)^m \quad (15)$$

where the constants B, m, and h_f (final displacement after complete unloading) are all estimated by least-squares fitting of the unloading data from the stiffness measurement. The term (h-h_f) is known as the elastic displacement. Once these variables have been calculated, the contact stiffness S can be found by differentiating Eqn. 15 and evaluating the resulting expression at the maximum penetration:

$$S = \left.\frac{dP}{dh}\right|_{h=h_{max}} = Bm(h - h_f)^{m-1}\Big|_{h=h_{max}} \quad (16)$$

This equation is very accurate for the initial 25% to 50% of the unloading curve; beyond that it may provide inadequate results. Therefore only the initial portion of the unloading curve data is used to determine the contact stiffness.

3.3.2. Continuous Stiffness Measurement

The previous set of equations allows the calculation of the elastic modulus and hardness of a material at a predetermined depth of penetration. If, as in the case of biological materials, thin films, polymers and other composites, the modulus may change with

depth, it becomes necessary to use the continuous stiffness measurement (CSM) option. This technique determines the hardness and elastic modulus of the test material as a continuous function of surface penetration by including a small, high-frequency oscillation force over the main loading signal and using a frequency-specific amplifier to analyze the system's response to that oscillation. In order to understand how CSM testing is carried out it is necessary to begin with the concept of simple harmonic motion.

3.3.2.1. Simple Harmonic Oscillator

Nanoindentation machines can be modeled as a simple harmonic oscillator because all of the motion is restricted to one dimension, and therefore there is only one mode of oscillation. A simple harmonic oscillator involves a spring constant (or stiffness), a damping factor and a mass, as shown in Figure 27. The following sections explain the process of arriving at the dynamic contact stiffness K_c which is then used in place of the semistatic contact stiffness S for all IIT testing calculations.

Exciting this simple-harmonic oscillator system by an applied force:

$$\boldsymbol{F(t) = F_o e^{i\omega t}} \qquad (17)$$

causes a vertical displacement represented by the particular solution:

$$\boldsymbol{z(t) = z_o e^{i(\omega t - \phi)}} \qquad (18)$$

where the mass oscillates at a frequency ω, but lags by phase angle ϕ. The relationship between force and response is given by the differential equation:

$$\boldsymbol{m\ddot{z} + D\dot{z} + Kz = F(t)} \qquad (19)$$

The first and second derivatives of z are:

$$\dot{z}(t) = z_o i\omega e^{i(\omega t-\phi)} \quad (20)$$

$$\ddot{z}(t) = -z_o \omega^2 e^{i(\omega t-\phi)} \quad (21)$$

Substituting Eqns.17, 18, 20 and 21 into Eqn.19 yields:

$$m\left(-z_o \omega^2 e^{i(\omega t-\phi)}\right) + D\left(z_o i\omega e^{i(\omega t-\phi)}\right) + K\left(z_o e^{i(\omega t-\phi)}\right) = F_o e^{i\omega t} \quad (22)$$

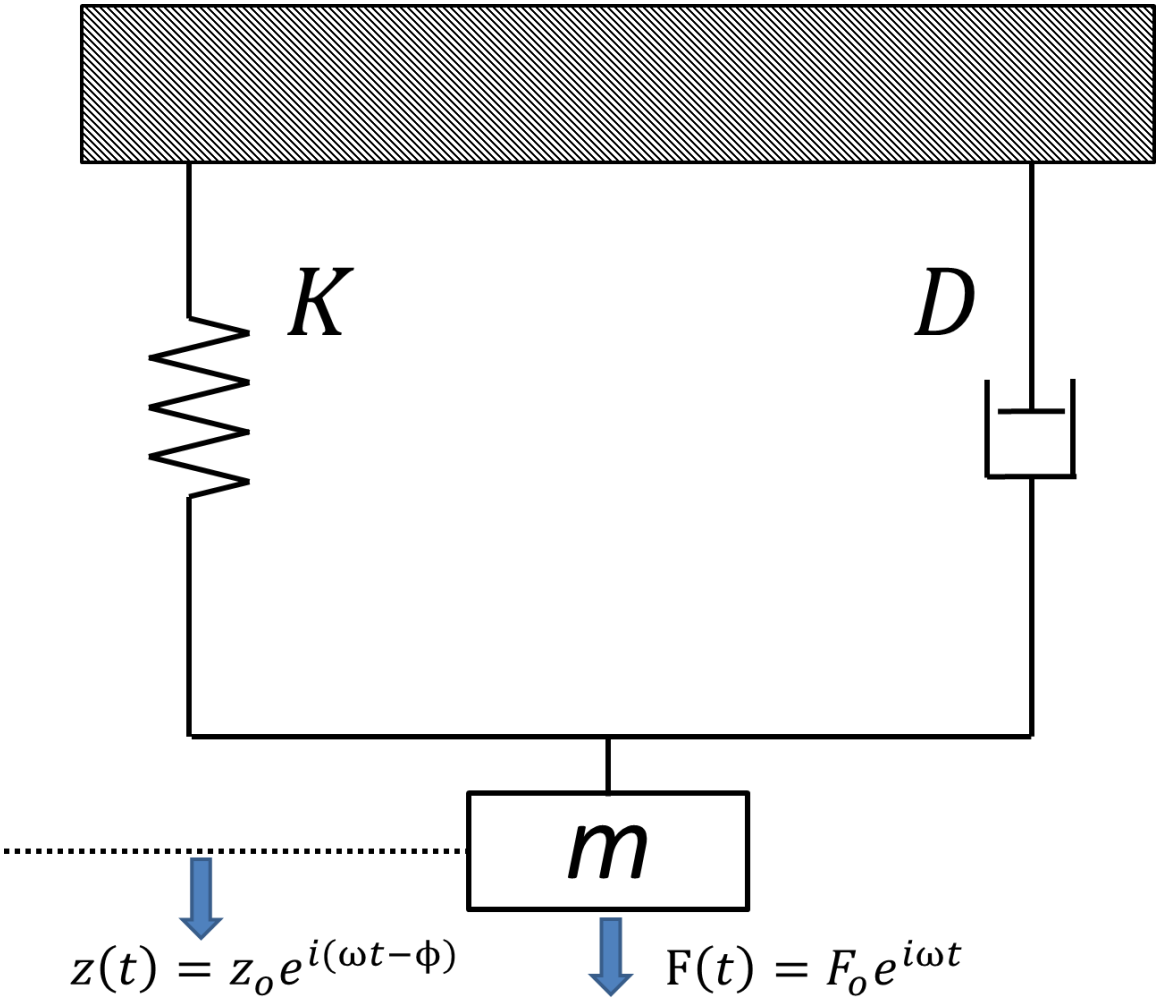

Figure 27 - Simple harmonic oscillator model. *K* is the stiffness of the system, *D* is the damping of the systems, and *m* is the mass undergoing oscillation

Multiply all terms in Eqn. 22 by $\frac{e^{i\phi}}{z_0 e^{i\omega t}}$ to arrive at:

$$-m\omega^2 + iD\omega + K = \frac{F_0}{z_0} e^{i\phi} \quad (23)$$

Invoking Euler's formula to substitute for $e^{i\phi}$ yields:

$$-m\omega^2 + iD\omega + K = \frac{F_0}{z_0}(\cos\phi + i\sin\phi) \quad (24)$$

Equating the real parts of Eqn. 24 gives:

$$K - m\omega^2 = \frac{F_0}{z_0}\cos\phi \quad (25)$$

Likewise, the imaginary parts yield:

$$D\omega = \frac{F_0}{z_0}\sin\phi \quad (26)$$

Eqns. 25 and 26 can be combined to form the relationship between stiffness and damping by the phase angle by which the response lags the excitation:

$$\tan\phi = \frac{D\omega}{K - m\omega^2} \quad (27)$$

This solution can be expressed by Figure 28 and by the Pythagorean theorem:

$$(K - m\omega^2)^2 + (D\omega)^2 = \left(\frac{F_0}{z_0}\right)^2 \quad (28)$$

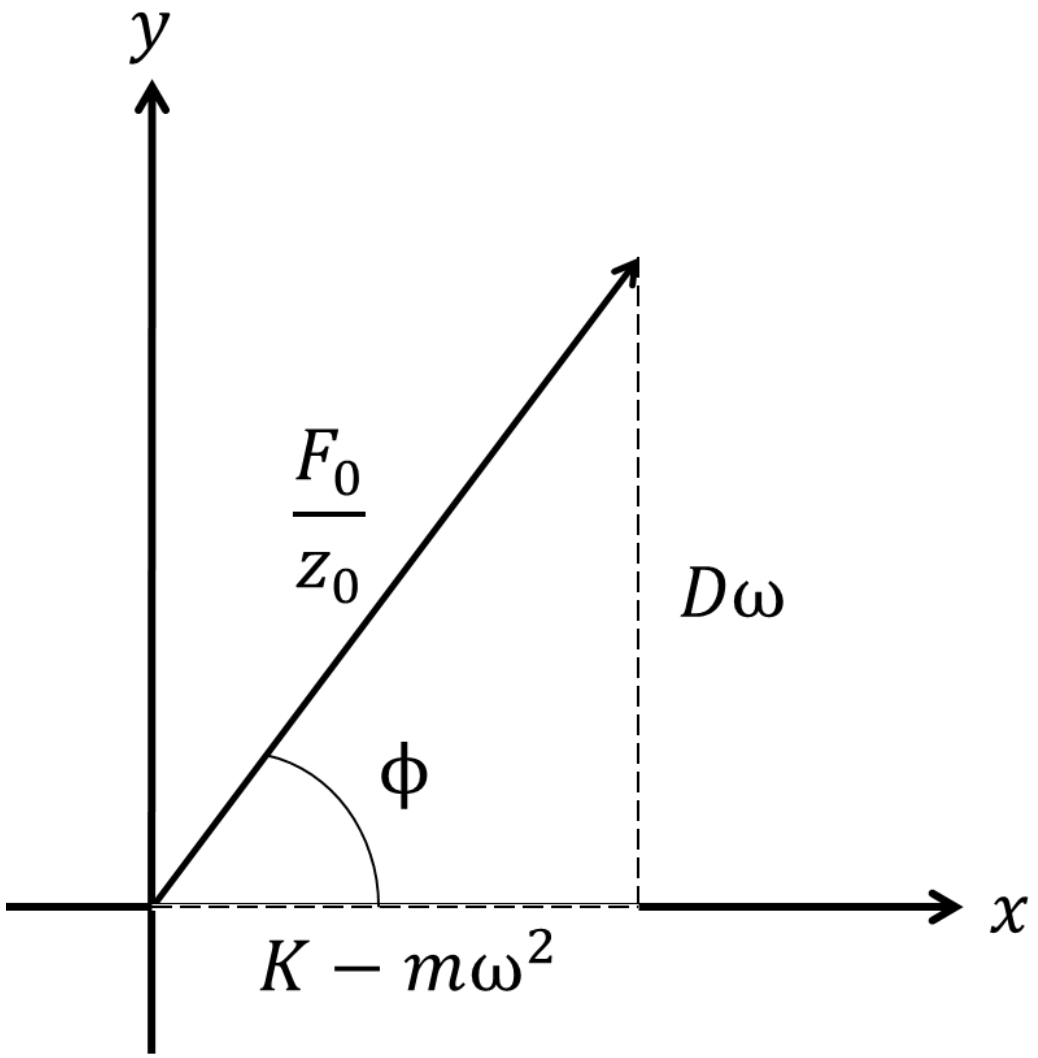

Figure 28 **- Expression of solution for a simple harmonic oscillator model (after (Hay 2009)).**

The slope of the hypotenuse in Figure 28 is known as the dynamic compliance, which is the ratio of the amplitude of the displacement oscillation to the amplitude of the excitation, and has the dimensions of length per unit force. This ratio peaks at resonance if the system is underdamped. The value of this ratio decreases monotonically with frequency for any frequencies greater than resonance. Solving Eqn. 28 for dynamic compliance yields:

$$\frac{z_o}{F_0} = \frac{1}{\sqrt{(K - m\omega^2)^2 + (\omega D)^2}} \quad (29)$$

3.3.2.2. Modeling the Indenter Prior to Contact

A basic simple-harmonic oscillator model consists of an indenter which is not in contact with a specimen (indenter said to be free-hanging). In this case the components of the model are those of the indenter only: $K=K_i$, $m=m_i$ and $D=D_i$. The springs supporting the indenter shaft (shown in Figure 29) and the capacitive displacement gauge are the main contributors to K_i and D_i, respectively. The indenter shaft corresponds to m_i.

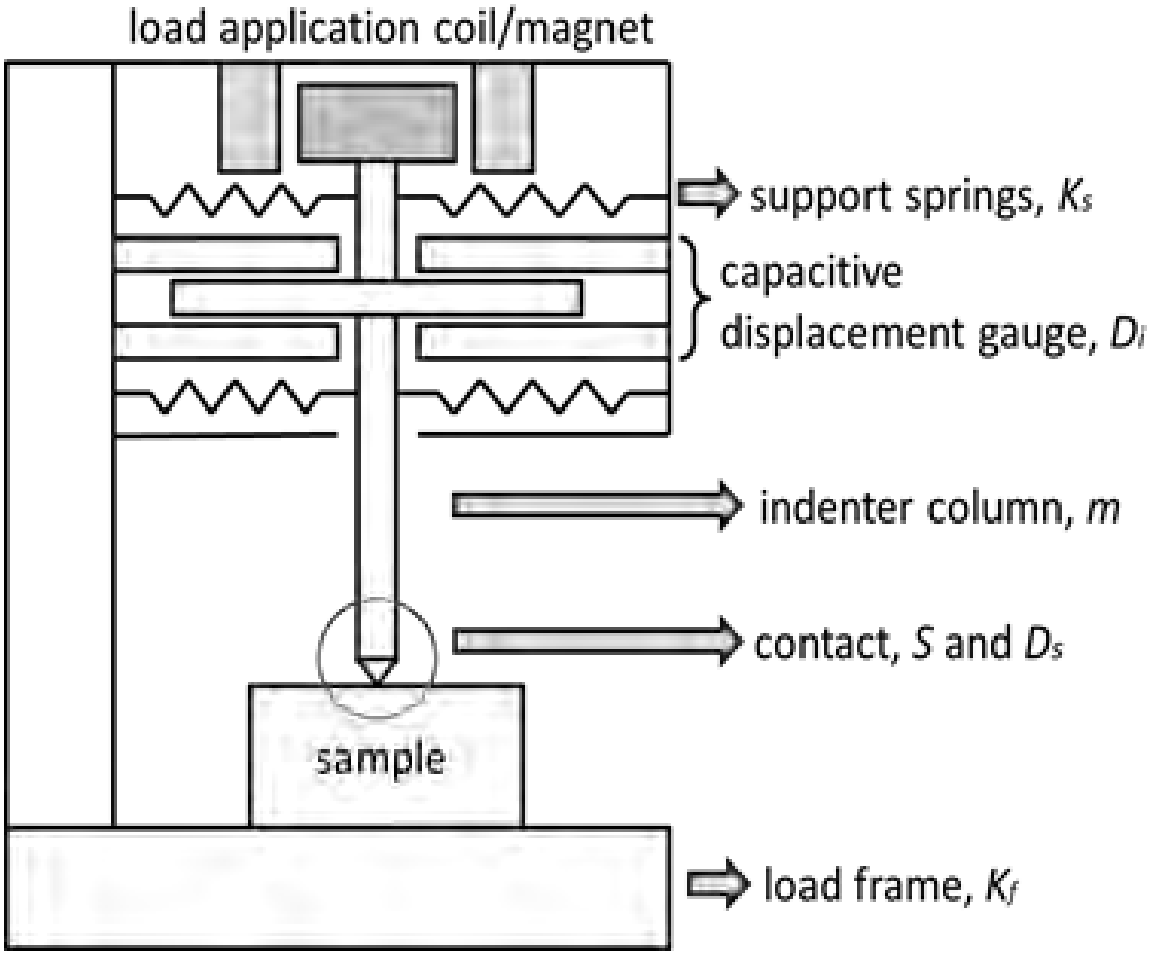

Figure 29 - Schematic of a nanoindentation machine

Substituting these variables into Eqns. 25, 26 and 29 yields:

$$K_i - m_i\omega^2 = \frac{F_0}{z_0}\cos\phi\Big|_{free-hanging} \quad (30)$$

$$D_i\omega = \frac{F_0}{z_0}\sin\phi\Big|_{free-hanging} \quad (31)$$

$$\frac{z_o}{F_0} = \frac{1}{\sqrt{(K_i - m_i\omega^2)^2 + (\omega D_i)^2}} \quad (32)$$

These dynamic components are determined for a given indenter by oscillating it over a range of frequencies and plotting the compliance versus frequency, curve-fitting the data to the form of Eqn. 32.

3.3.2.3. Natural Frequency

The natural (or resonant) frequency of a free-hanging indenter is given by a relationship of the mass and stiffness:

$$f_n = \left(\frac{K_i}{m_i}\right)^{\frac{1}{2}} \quad (33)$$

Systems with higher natural frequencies are desirable for performing dynamic indentation because of two factors:

- Background vibrations, originating from ventilation, foot traffic, doors and ground motion, tend to occur at low frequencies (usually less than 10 Hz). Operating above this range mitigates the machine's sensitivity to these sources of interference.
- A higher natural frequency means the device can accommodate a wider range of frequencies for testing frequency-dependent samples.

3.3.2.4. Modeling Indenter in Contact with Specimen

The simple-harmonic oscillator model must now be adjusted to include the effective stiffness and damping of the contact between the indenter and the test material (Figure 30).

This model can be simplified into equivalent stiffness and damping components by combining the effects of the indenter, frame, and contact:

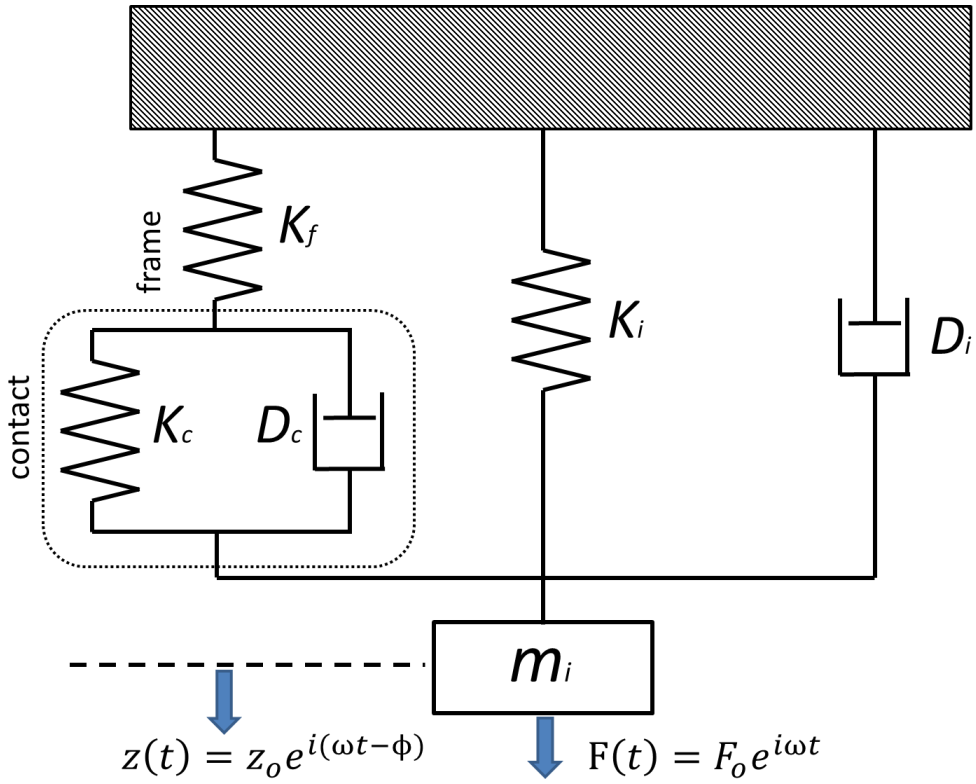

Figure 30 - Simple harmonic oscillator model accommodating both instrument and contact with specimen

$$\boldsymbol{K_{eq}} = \left(\frac{\mathbf{1}}{\boldsymbol{K_f}} + \frac{\mathbf{1}}{\boldsymbol{K_c}}\right)^{-\mathbf{1}} + \boldsymbol{K_i} \qquad (34)$$

$$\boldsymbol{D_{eq}} = \boldsymbol{D_i} + \boldsymbol{D_c} \qquad (35)$$

The simplified model is shown in Figure 31 in the form of a basic simple harmonic oscillator system. Rearranging Eqns. 34 and 35 to solve for stiffness and damping of the contact yields:

$$\boldsymbol{K_c = \frac{K_f(K_e - K_i)}{K_f - (K_e - K_i)}} \quad (36)$$

$$\boldsymbol{D_c = D_e - D_i} \quad (37)$$

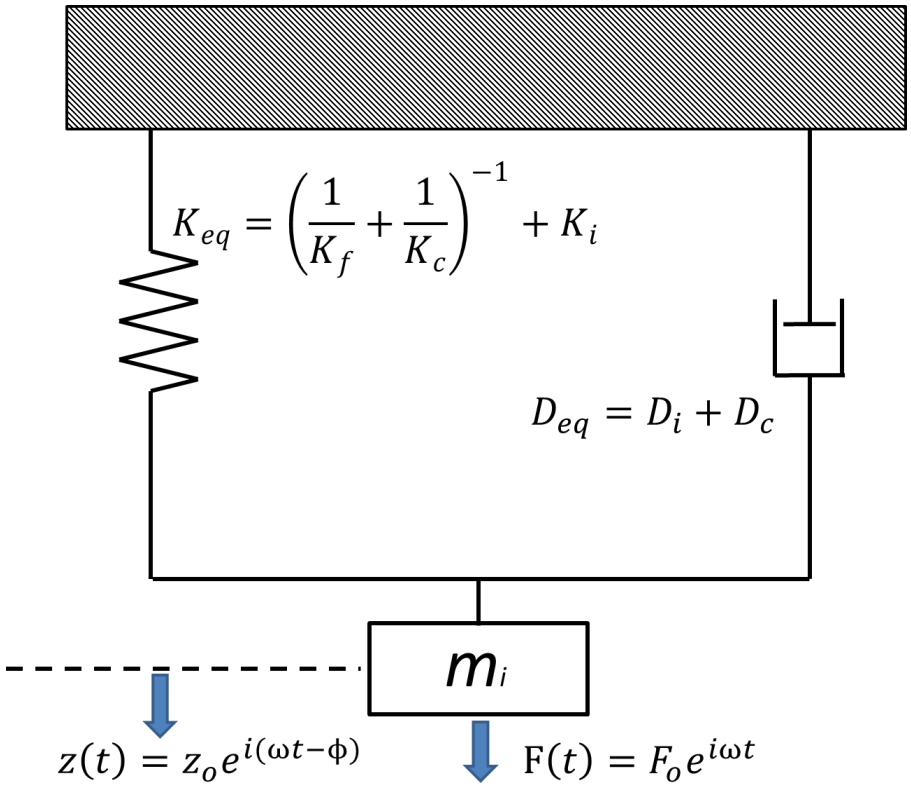

Figure 31 – Simple harmonic oscillator model with instrument and contact parameters combined into equivalent expressions

Substituting these equivalent components into Eqns. 25 and 26 yields:

$$\boldsymbol{K_e - m\omega^2 = \frac{F_0}{z_0}\cos\phi} \quad (38)$$

$$D_e\omega = \frac{F_0}{z_0}\sin\phi \tag{39}$$

The stiffness of the contact, K_c, can now be found by substituting Eqns. 30 (K_i) and 38 (K_e) into Eqn. 36:

$$K_c = \frac{K_f\left[\frac{F_0}{z_0}\cos\phi - \frac{F_0}{z_0}\cos\phi\Big|_{free-hanging}\right]}{K_f - \left[\frac{F_0}{z_0}\cos\phi - \frac{F_0}{z_0}\cos\phi\Big|_{free-hanging}\right]} \tag{40}$$

Notice that the mass of the indenter does not affect the contact stiffness, which is entirely dependent on the frame stiffness and the real portion of the amplitude ratio (right side of Eqn. 25. If, as in nanoindentation, the contact area is very small, the frame can be considered infinitely stiff in regard to the contact stiffness. Eqn. 40 then simplifies to:

$$K_c = \frac{F_0}{z_0}\cos\phi - \frac{F_0}{z_0}\cos\phi\Big|_{free-hanging} \tag{41}$$

The damping of the contact is determined by substituting Eqns. 39 (D_e) and 31 (D_i) into Eqn. 37, which shows that the contact damping is the value of the imaginary part of the amplitude ratio (right side of Eqn. 26) minus that same parameter just before contact:

$$D_c = \frac{F_0}{z_0}\sin\phi - \frac{F_0}{z_0}\sin\phi\Big|_{free-hanging} \tag{42}$$

The dynamic contact stiffness K_c can now replace the semistatic contact stiffness S in Eqns. 9 and 14 in order to determine the elastic modulus and hardness as a function of penetration. The elastic modulus is now found with:

$$E_r = \frac{(\sqrt{\pi} \cdot K_c)}{2\beta\sqrt{A}} \quad (43)$$

$$E = (1 - \nu^2)\left[\frac{1}{E_r} - \frac{1 - \nu_i^2}{E_i}\right]^{-1} \quad (44)$$

And the hardness is calculated with:

$$h_c = h - 0.75\frac{P}{K_c} \quad (45)$$

$$A = 24.56 \cdot h_c^2 \quad (46)$$

$$H = \frac{P}{A} \quad (47)$$

All of these calculations are carried out automatically when using the Nano Instruments® MTS Nano G200 machine. The TestWorks software processes the data from a test run and outputs modulus and hardness data.

4. EXPERIMENTS

Concepts, construction, execution and processing of each of the three experiments carried out in the present research are presented in this chapter. The first experiment involved an increasing static load applied vertically to the tergum to mimic various stages of contraction of the DVMs. This effort established a spring constant for the thorax-wing system and determined the approximate compression of the thorax for the maximum wing elevation angle. The second experiment improved upon the first by dynamically applying a vertical compressive force through the thorax with the appropriate frequency and displacement to create an artificially induced, full-elevation

flapping motion. An extensive review of the literature revealed that neither of these experiments has a precedent. A third experiment examined the elastic modulus of the tergum using a nanoindentation technique called constant stiffness measurement.

4.1. Static Load Experiment

This experiment was conceived as a proof of concept which would ultimately lead to an effective design for the dynamically-actuated load experiment. It was initially thought that the data was not going to be particularly useful because there was no need to characterize static forces and wing angles. It became evident as the experiment progressed that the results would in fact be applicable to FE models which require a benchmark for static load/displacement values.

The device was designed to determine the approximate static vertical compressive force, applied vertically through the thorax to simulate DVM contraction, required to hold the wings at various angles throughout the maximum natural range of elevation. This experiment also enabled the derivation of a mechanical spring constant for the thorax/wing mechanism. Eventually, the force and vertical compression displacement data were enlisted to provide a guideline for the construction of a device which mimicked the action of the static model but with an automated and dynamic application of the load. Figure 32 shows the static load experiment setup.

4.1.1. Design of the Experiment

A *M.sexta* specimen is placed horizontally on a raised, solid block which is affixed to the lowest level of the rig. A vertical rod centered over the thorax rests on the tergum. This rod passes through a sheath which is held steady by two platforms above the

specimen. The upper end of the rod supports a platform for holding weights. A digital point-and-shoot camera is positioned in front of the moth and centered on the longitudinal axis.

Figure 32 - Static load device in use (note: raised platform in front of the device is where the camera rests)

An image is captured each time a weight is added to the push rod. The angles of the wings relative to horizontal and the vertical compression of the thorax can then be correlated to the applied force throughout the full range of motion of the upstroke. Figure 33 compares the initial concept with the device as built. The theoretical representation of the thorax/wing mechanism from Chapter 3 is repeated here (Figure 34) to reinforce the concept of the thorax as a mechanical system.

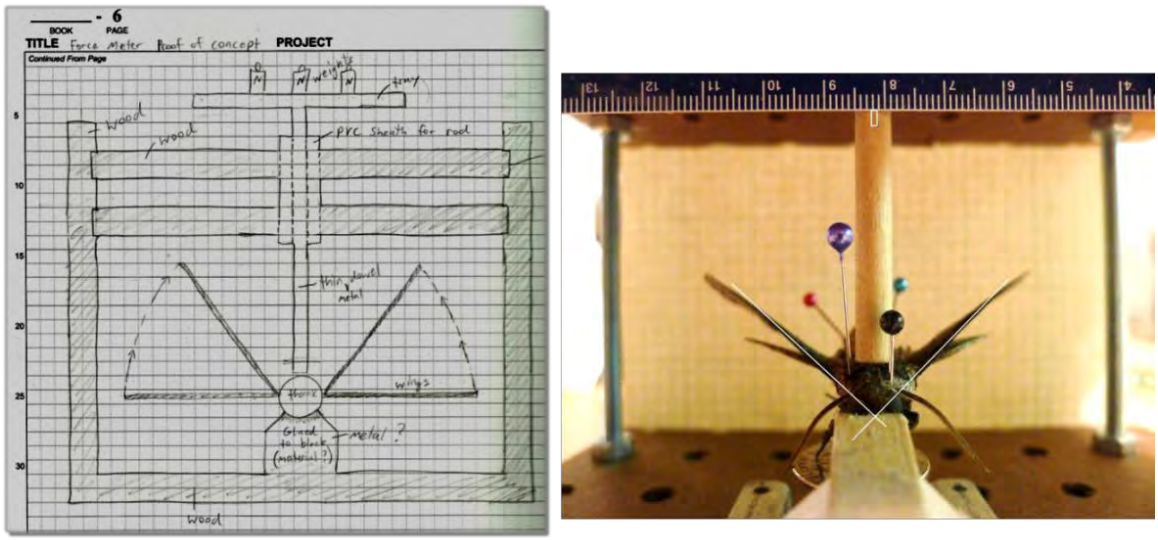

Figure 33 – Original concept sketch and constructed device

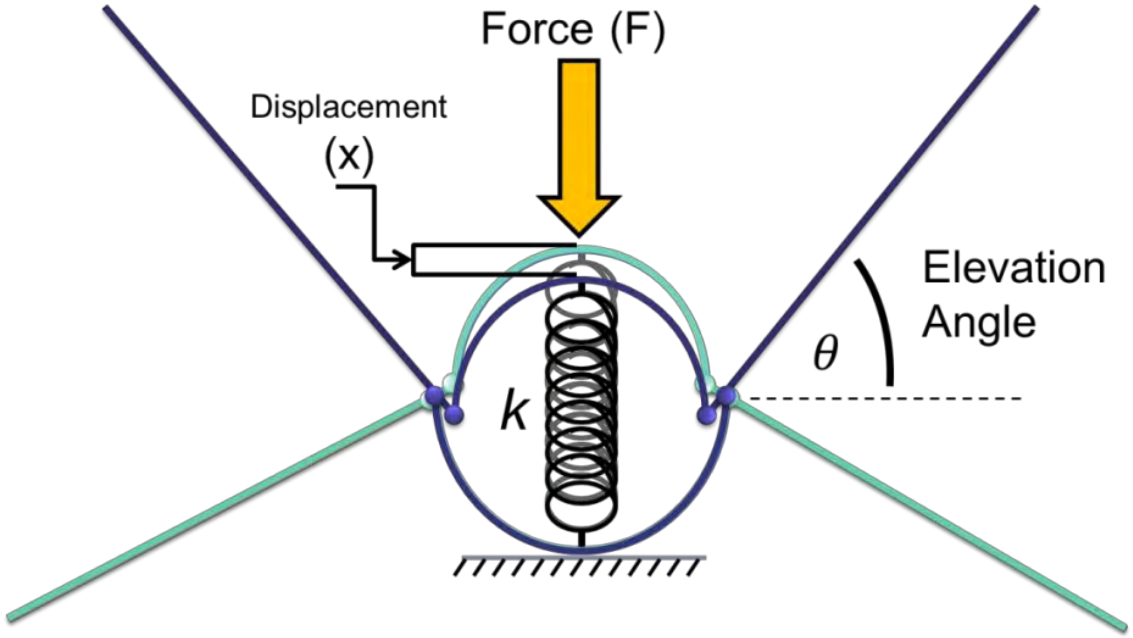

Figure 34 - Schematic of the thorax as a mechanical system with spring

4.1.2. Construction

The main body of the device was constructed from three 15 by 19 cm pegboard rectangles held in place by nuts on four vertical bolt shafts. Assembled, it was 14 cm tall.

A 5 mm diameter wooden dowel rod was used for the push rod, with one end pressed into a hole drilled into a piece of wood. The width of this dowel rod was chosen to as large as possible without impeding the motion of the wing hinges, in order to prevent bending or compression of the rod. The platform for the moth was a wooden block measuring 4cm tall, 1.3 cm wide and 10 cm long attached to the lowest level of the rig. The major components and the constructed device are shown in Figure 35. Note the pair of upper platforms with a sheath for the push rod. These platforms gave the structure stability and provided a conduit through which the push rod could be straightly tracked.

Figure 35 - Main components and constructed device

4.1.2.1. The Mount

At the outset of exploratory testing, the specimens were mounted directly onto the horizontal top of the wooden block shown below the push rod in Figure 35, but this method was found to be unreliable in terms of stability. It was challenging to get pins into the hard wood, and the horizontal orientation of the block meant that the tergum was

slanted forward (Figure 36). To remedy this problem, a wooden clothes pin was dismantled and glued together in such a way as to create a ramp on which the specimen could be mounted.

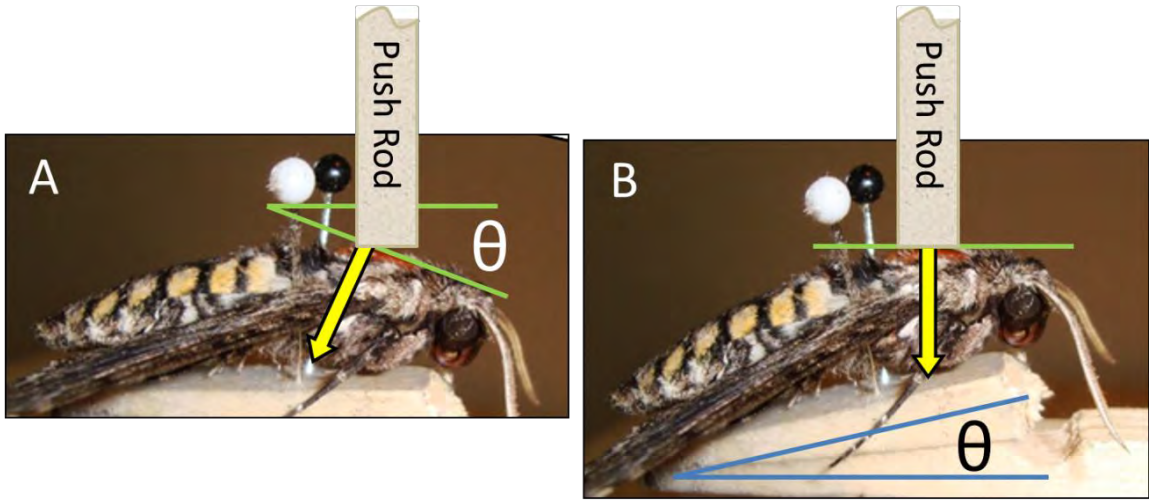

Figure 36 - Importance of mounting angle: **(A)** Original orientation, tergum tilted forward; **(B)** Elevated 14 degrees, tergum is now horizontal. End of push rod fits flush against the tergum.

The ramp then sat atop the wooden block. By coincidence, the angle created by the glued-together end pieces of the clothes pin happened to be reasonably close to the slope of the tergum (14 degrees). Additionally, the soft wood of the clothes pin facilitated easier usage of pins to prevent slipping. Figure 36 demonstrates the reason for elevating the angle of the mount. In part A, a horizontal arrangement shows how the force from the push rod is directed down and back due to the forward tilt of the tergum, and is originating from the edge of the push rod instead of the center. This can cause the specimen to slip rearward and, in some cases, buckle the tergum due to the concentrated force from the edge of the rod. In part B, the specimen has been angled so that the tergum is horizontal and parallel with the bottom of the push rod. This elevated position

distributes the force evenly and focuses it vertically downward in the direction of the natural contraction of the DVMs.

4.1.2.2. Refining the Experiment

The initial version of this experiment did not make use of a load cell to determine the force transferred through the thorax by the rod. Instead, increasing numbers of US quarters, which have a known mass of 5.670 grams, were successively placed on the weight platform and used as an approximation of the applied force. There was no provision for determining frictional losses in the system. The data obtained in this manner served as a proof of concept to show that the experiment would work, even if the actual numbers are unreliable.

4.1.2.3. Improved Design with Load Cell

The final version, after the first had shown that the experiment was feasible, made use of a load cell beneath the moth to accurately record the total force transmitted through the thorax, thereby accounting for frictional losses. For example, if a load of 0.5 N were placed on the platform, but the sheath produced a frictional loss of 0.1 N, then the specimen would experience a compressive force of 0.4 N on the thorax and that is what the load cell would measure.

4.1.3. Procedure

After being prepared for testing (see Appendix A), each moth was photographed for record-keeping. The scales were then removed from the thorax and the moth was positioned on the mount. A piece of a wooden clothespin served as a suitable mount. Pins held the moth in place on the mount, surrounding the thorax at the waist and neck, or the

narrow transitions between the abdomen/thorax, and thorax/head, respectively. These pins did not pierce any part of the moth, but adequately prevented movement of the specimen during testing. The mount, along with the specimen, was then positioned in its place on the device and aligned so the push rod rested on the top of the thorax. The mount was then secured to the wooden block with tape. The camera, a digital point-and-shoot Panasonic Lumix DMC-LX5, was positioned in front of the device so that the center of the image was aligned with the longitudinal axis of the specimen and the leading edges of the forewings were clearly visible. The lighting was adjusted using two flashlights to ensure proper illumination of the specimen and a few practice images were captured to confirm satisfactory performance.

4.1.3.1. Load Measurement

A baseline image was captured before applying any load to the specimen. The push rod alone was lowered into place on top of the thorax for the second image. After that, one US quarter, with a mass of 5.670 grams, was added to the push rod's platform for each successive image until 10 quarters rested on the platform (Figure 37). Next, 2 quarters were added for each of the subsequent 3 images. Finally, 4 quarters were added for a total of 20 quarters on the platform. This ensured the full range of motion of the upstroke would be achieved. The quarters and the push rod were then removed.

The force transmitted through the thorax was recorded by a load cell positioned beneath the specimen. The load cell was a 3 kg cantilever beam type which had been removed from an off-the-shelf food scale by O'Hara. The signal was amplified and transmitted to a laptop computer via a circuit board designed by O'Hara and the author.

Figure 37 - Stack of quarters on push rod weight platform

The signal from the load cell was processed by software called PICkit2, which recorded the amplified voltage from the strain gauge on the load cell. The theory of load cells and strain gauges is well-established and will not be expounded here (Hoffmann 1989), (loadcelltheory.com 2012), (Omega 2012). Figure 38 shows a schematic of a specimen mounted on the load cell.

Calibration was performed prior to each new specimen by stacking quarters onto the load cell and recording the voltages produced for a given set of weights. Figure 39 is a typical plot from one of these calibrations, demonstrating that the result can be approximated with a linear function. The force, therefore, was derived from a given reading using that test run's calibration equation.

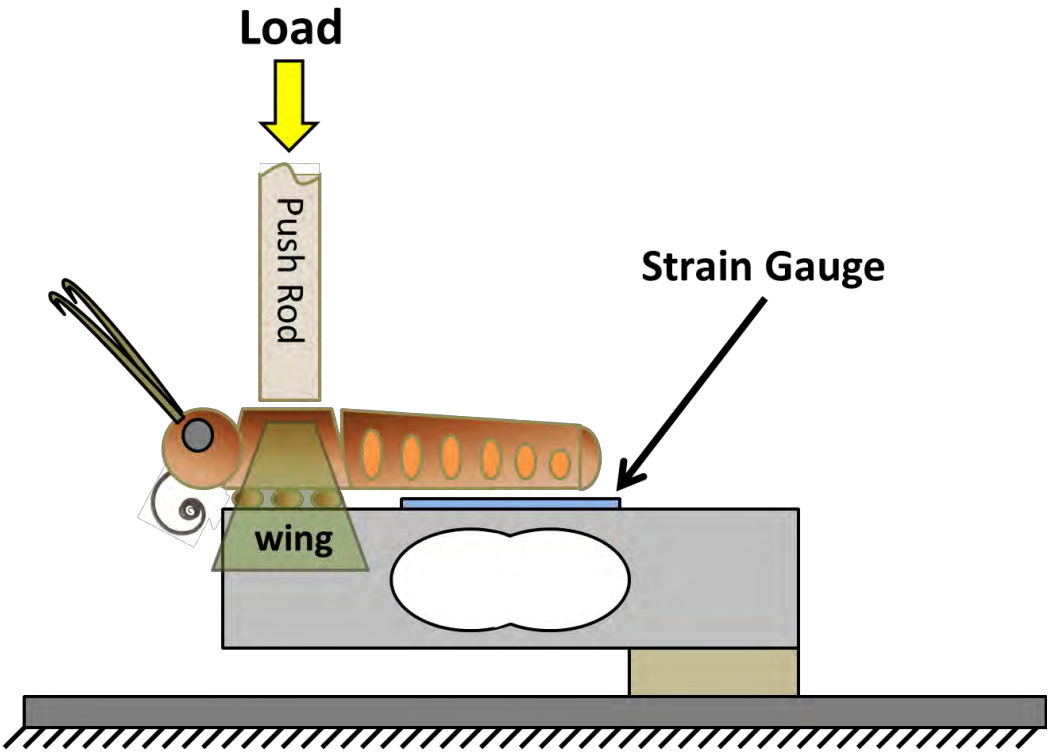

Figure 38 – Depiction of cantilever beam load cell with moth

4.1.4. Processing

This section details the method with which the images and load data were correlated and processed. The wing angles and thoracic compression were measured from the images using a Matlab code. Some portions of this processing code will be discussed here; the entire code is presented in Appendix B.

The set of images from each specimen was uploaded to a computer and opened in Microsoft Paint. This allowed a line to be drawn along the leading edge of each forewing. These lines extended past the midpoint of the image so that they crossed paths over or near the head of the moth. Figure 40 presents a typical set of images from one of the specimens. The lines drawn over the wings' leading edges and their intersection served as a guide for calculating the angles of the wings. Additionally, the thoracic compression

was measured by determining the distance between a dot drawn on the push rod shaft and the bottom of the ruler near the top of those images. The increasing value of this distance as the force and wing angles increased characterized the compression of the thorax.

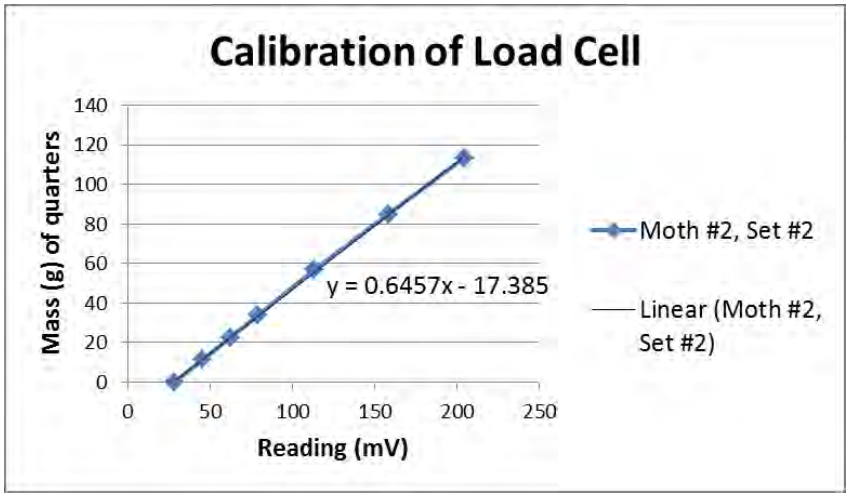

Figure 39 - Example of load cell calibration

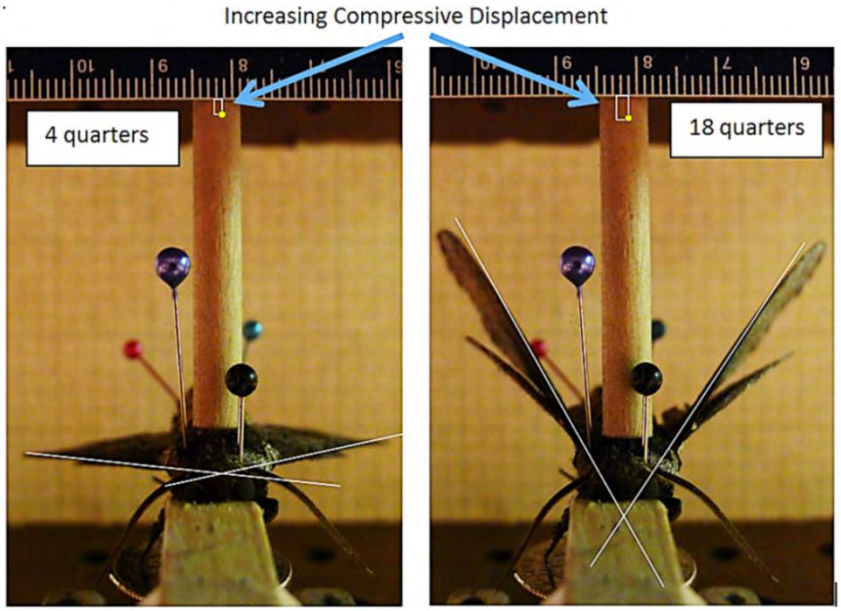

Figure 40 - Edited images from 2nd iteration: Compressive displacement is now being tracked. The dot is located in the lower right corner of the small white-bordered boxes. The actual small black dot is not readily visible so its location on the push rod is indicated with a yellow circle. The vertical distance used in the calculations is the distance between that dot and the edge of the ruler (top of white-bordered box).

These edited images were then saved and opened with a Matlab code. The code asked the user to click on the image first at the intersection of the lines and then on the left wing leading edge and right wing leading edge, respectively, followed by the edge of the ruler and the dot on the push rod. This selection sequence is shown in Figure 41. The code then calculated the angle above horizontal of each wing and the distance of the dot from the ruler based on the *x* and *y* coordinates of the five selected points (Figure 42).

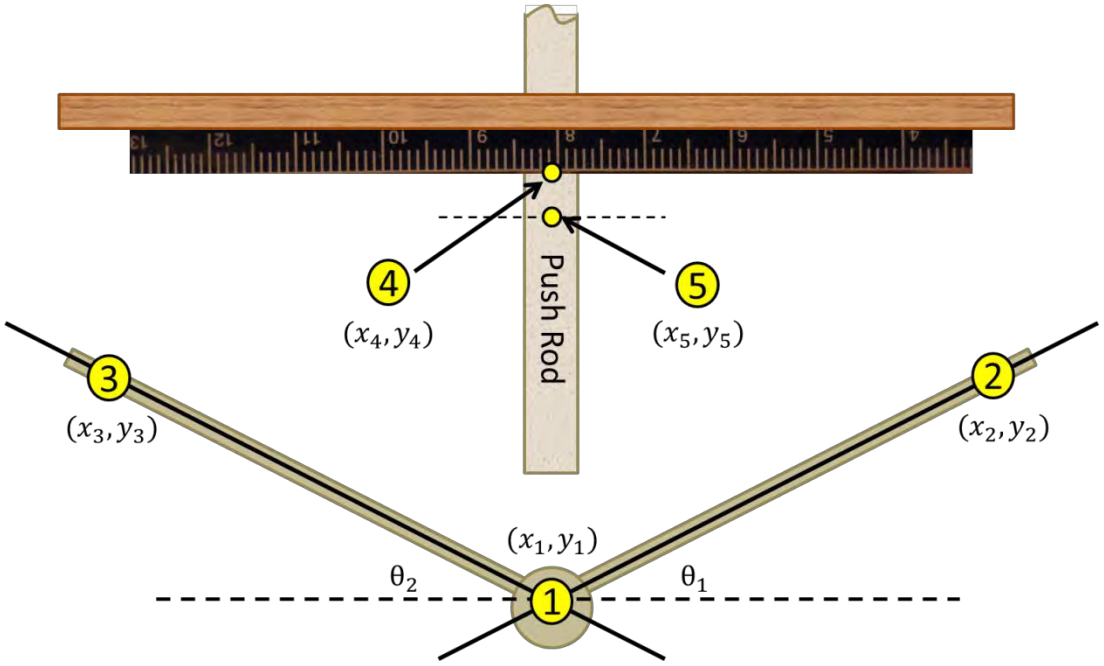

Figure 41 - Locations and order of selection for wing angle and thorax vertical compression calculation. Note that points 2 and 3 can be selected anywhere along their respective leading edge lines, which had been traced along the straightest portion of the leading edge of the specimen's forewings.

```
%% Calculate wing angles and vertical distance from ruler
Theta_Right=abs(atand((y(2)-y(1))/(x(2)-x(1))))
Theta_Left=abs(atand((y(3)-y(1))/(x(3)-x(1))))
disp=abs(mm(4,2)-mm(5,2))
```

Figure 42 - Portion of the code for wing angles and displacement (note addition of points 4 and 5 over code for first iteration)

This data set was entered into an excel file along with the load data. Plots of force versus wing angle were created for each specimen, and then combined for further analysis (see Chapter 5).

4.2. Dynamic Load Experiment

The concept of applying a vertically compressive load to the thorax, inducing a natural elevation of the wings, is the same here as in the static load experiment. However, this device mimicked the dynamic application of the DVM force of a *M.sexta* in flight. The objective was to obtain force, displacement and time functions as a vertical compressive load was applied at 25 Hz to the thorax and inducing realistic wing elevation. The application of the load at 25 Hz simulated the real-time contraction of the DVMs at the flapping frequency for hovering flight. For each specimen the amplitude of the shaker signal was varied until the device induced a maximum wing elevation angle of approximately 55 degrees above horizontal as viewed from the front, which is *M.sexta'*s natural maximum wing elevation while hovering. The elevation of the wings on the stroke plane is between 70 and 75 degrees, but the tilt of the moth's body and the non-vertical motion of the wings cause that stroke plane to deviate from vertical by an angle of 20 to 30 degrees (Willmott and Ellington 1997). Figure 43 depicts the orientation of *M.sexta* in hovering flight with the various parameters and relationships of angles and planes. Analysis of these angles with trigonometry lead to a rough estimate of 55 degrees of wing elevation as viewed from the front of the moth along the horizontal plane. This calculation was necessary to be able to use the high-speed camera to confirm that the proper Range of Motion (RoM) had been achieved during each run.

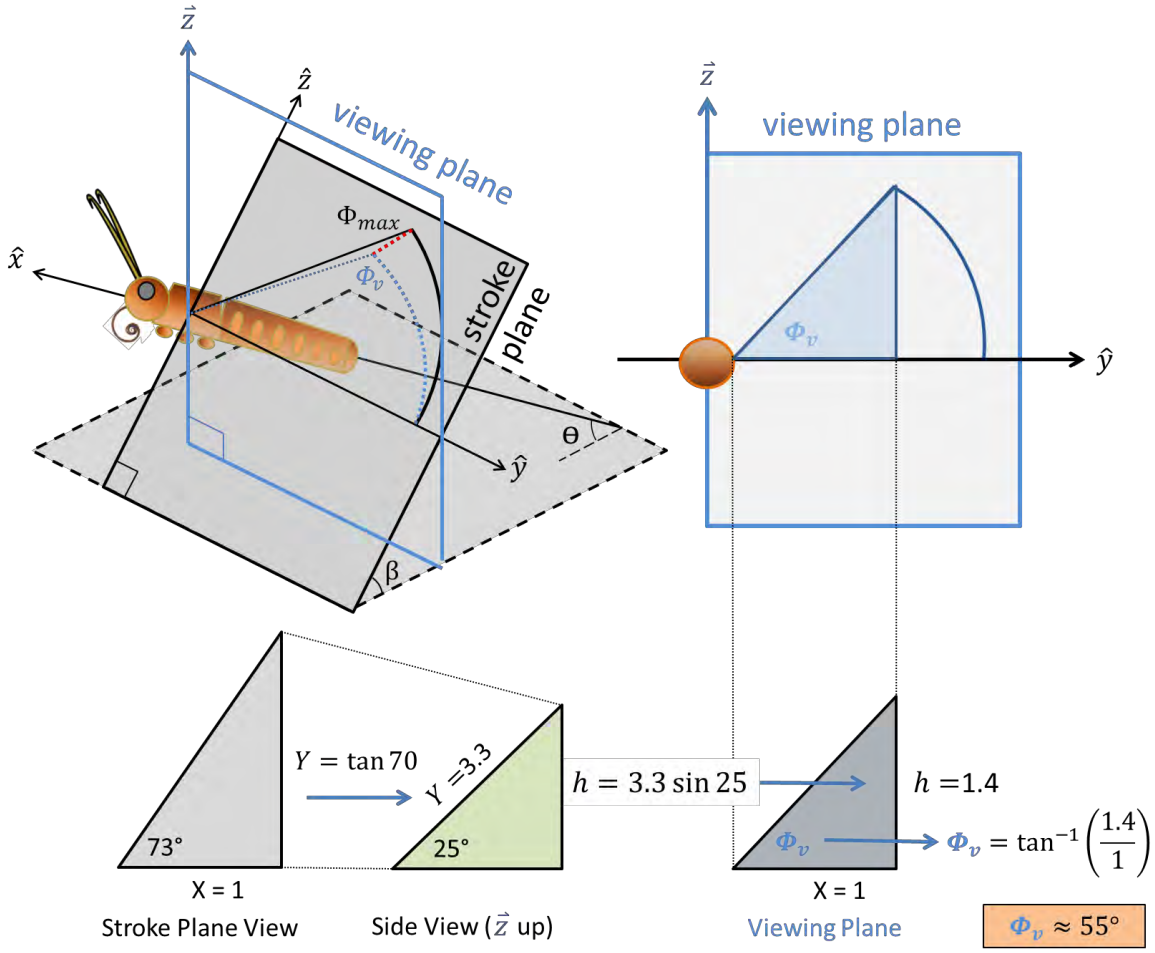

Figure 43 - Calculation of approximate wing elevation angle as viewed from the perspective of the high-speed camera

4.2.1. Design of the Experiment

This experiment was designed based on experience garnered through the static load experiment. However, there are a few significant differences between the two. Here, the load is dynamically applied from below the specimen so that the entire specimen and mount move up and down 25 times per second. The specimen rests on an adjustable mount attached to a Brüel & Kjaer Mini Shaker Type 4810 which is capable of raising and lowering through any desired vertical displacement up to 3 mm at a specified frequency. The push rod, held in a rigid position above the thorax, is attached to the same

load cell used in the static load experiment. These are held securely in place above the specimen by a frame which is bolted to the table around the shaker. Figure 44 shows a frontal view of the design and of the device as built. A Dantec Dynamics NanoSense MkII high-speed video camera with a Nikon AF Nikkor 28 mm lens captures 2500 frames per second (fps) as the moth is pressed into the push rod at 25 Hz, while the load cell records the load transmitted through the thorax at the same rate. Therefore the video frame No. 766 corresponds to load cell data point No. 766 and both occur at $time = \frac{766}{2500}$ seconds after the beginning of the run. This relationship facilitated simple processing and analysis.

4.2.1.1. Construction

The frame and mount were designed using the modeling software program SolidWorks Student Edition 2011-2012. The smaller, complex parts such as the push rod, mount pieces and frame joint structures, were printed with an Objet Eden500V™ 3-dimensional printer, while the large flat crossbeam and wall pieces were cut out of wood board. The high-speed camera required bright lighting conditions for obtaining quality images at 2500 fps, so standard white printer paper was taped to the sides and back of the frame to evenly distribute the light provided by the spotlights.

4.2.1.2. Set Up

A schematic of the power calculation experiment is shown in Figure 45. A test run begins with a Matlab code which sends two signals to the National Instruments USB-6251 Data Acquisition (DAQ) board. One is a sinusoidal wave function which is first run through a Bogen amplifier before reaching and actuating the shaker. The other signal is a trigger for

the high speed camera. While this is happening, the load cell is sending its voltage readings (a result of the compression of the thorax caused by the force application of the shaker) to the DAQ, which sends them to the laptop to be read by the code. The images captured by the high-speed camera are saved to a folder containing a processing code. An image of the experimental setup, labeled with the major components, is presented in Figure 46.

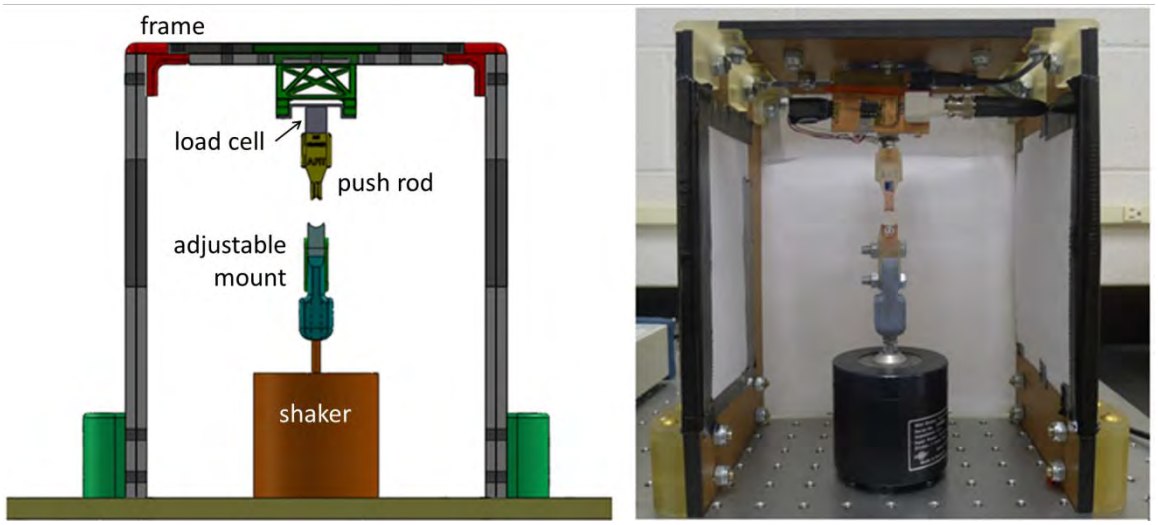

Figure 44 - Dynamic force experiment SolidWorks design and realized device

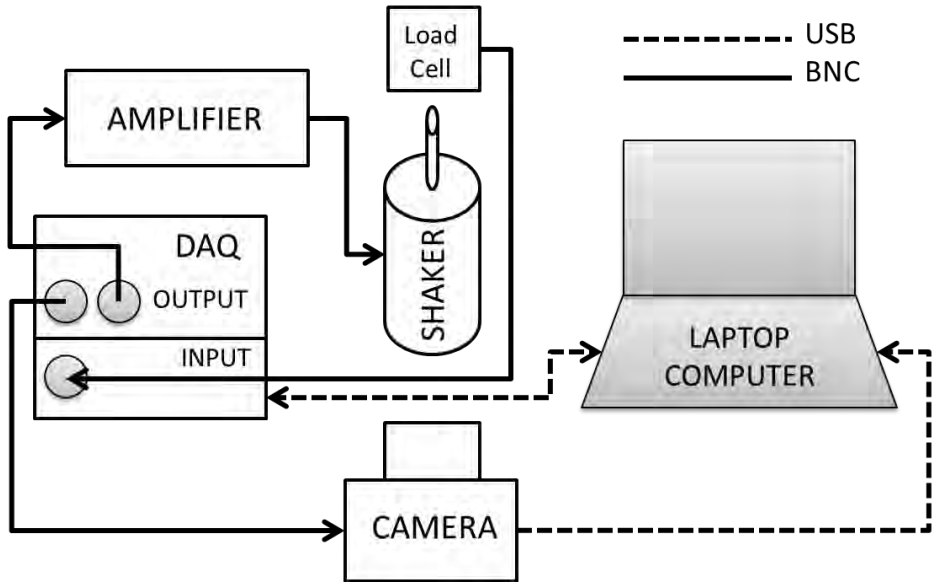

Figure 45 - Schematic of dynamic load application experiment

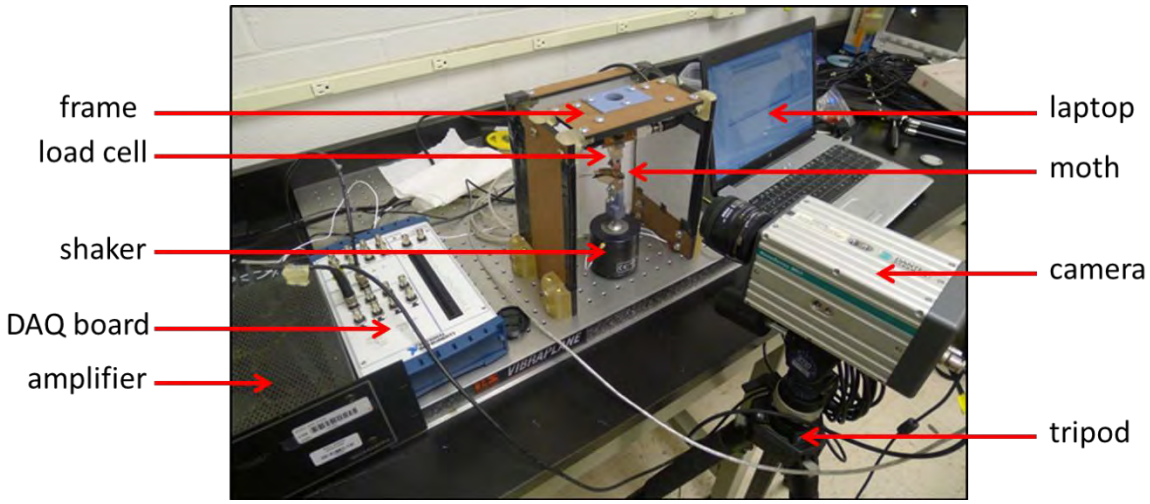

Figure 46 - Labeled photo of dynamic load experimental setup

4.2.1.3. Refining the Experiment

This experiment went through 3 phases before collection of meaningful data began. The purpose of the initial phase was to understand the nuances of the shaker and to learn how to synchronize the camera trigger with the shaker actuation. The problem of hooking up, calibrating, and successfully reading consistent data from the load cell was put aside until those initial goals had been achieved. The first iteration of the push rod and the load cell mount were designed around an Omega LCL Series thin-beam load cell. Figure 47 shows that load cell, the original push rod, and the load cell mount, and Figure 48 shows these components arranged in proof-of-concept test. This load cell was not wired to anything at this point and was subsequently set aside in favor of the larger, already-proven cantilever beam load cell from the earlier static load experiment. Once it had been decided that the original load cell from the static load experiment would suffice (a few quick oscilloscope readings had demonstrated its maximum capacity and its ability

to handle fast input) the load cell mount was significantly modified and a new push rod was designed to fit the bigger load cell (Figure 49).

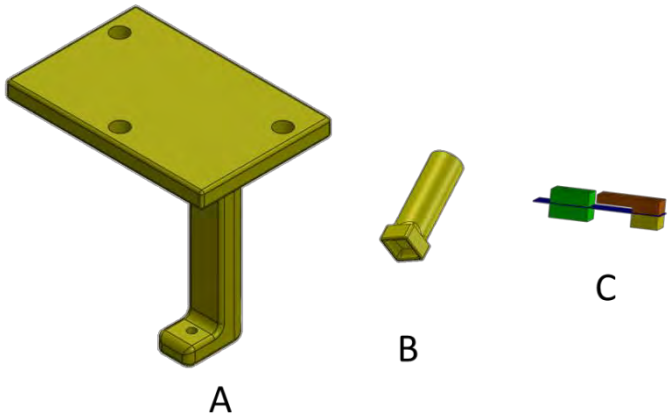

Figure 47 - Initial Designs: **(A)** load cell mount; **(B)** push rod; **(C)** thin-beam load cell

Figure 48 – Proof-of-concept phase of dynamic load experiment. Note paper scraps glued to wings for tracking wing angles. This practice was subsequently deemed unnecessary.

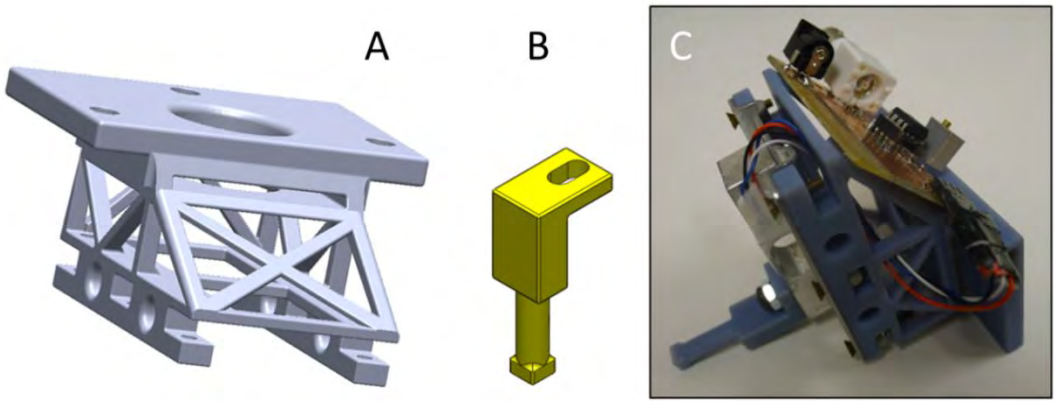

Figure 49 - Modified for original cantilever beam load cell: **(A)** Load cell mount; **(B)** Updated push rod; **(C)** Assembly with circuit board for load cell signal amplification and power

This load cell was calibrated for this experiment using an oscilloscope and known masses of 2, 10, 20 and 100 grams (Figure 50). A linear correlation of mass to volts was observed and converted to force in newtons with the portion of code shown in Figure 51. All three of the codes used in this experiment for the signal generation/force reading, video processing/point tracking and power calculation, are given in their entirety in Appendices C, D and E, respectively.

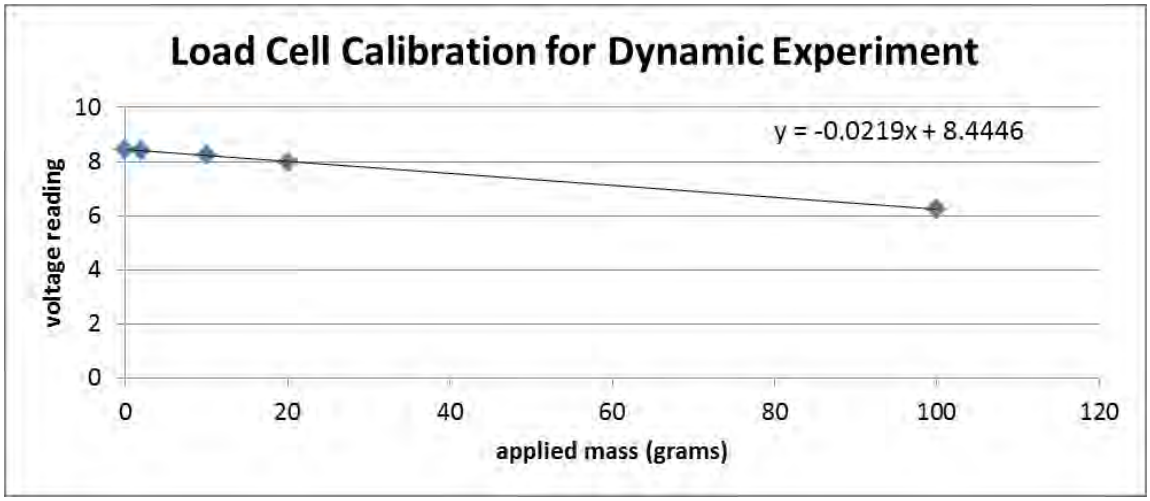

Figure 50 – Load cell calibration for dynamic load experiment

```
%% Convert voltage signal to grams and grams to Newtons
tare=sum(data_ai(1:t)/t) % ave. voltage signal from tare period
slope = 0.0219; % grams/volt slope of the load cell as calibrated
force = -45.749*data_ai + tare/slope; % converts V to g
forceN = force/101.971; % Convert g to N
```

Figure 51 - Portion of code which converts voltage signals from the load cell (*data_ai*) into force in newtons. The tare period is an 80 millisecond period of load readings before the shaker is actuated. The average reading from that period is applied to the force data in order to provide a baseline for the function.

Finally, a third push rod was designed to replace the second (Figure 52). This one had an angled lower portion, which ensured that the specimen could be lined up precisely under the push rod. This was necessary because, though the frame had been designed to

be centered over the hole for the shaker's attachment bolt, the shaker did not line up exactly as intended.

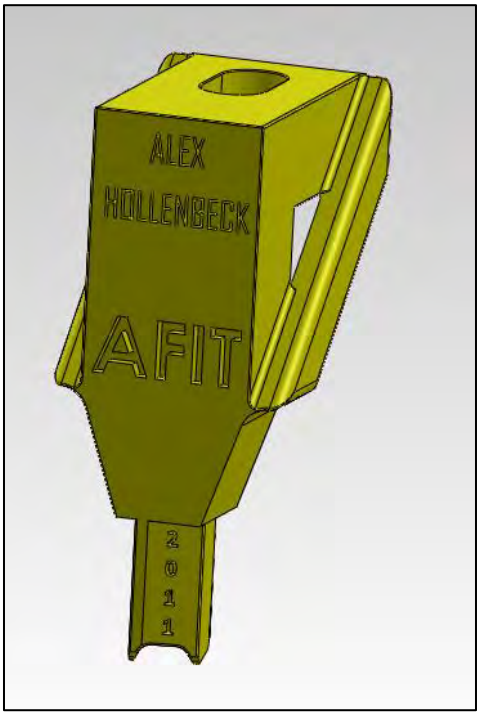

Figure 52 - Final iteration of the push rod with angled tip for improved fit

The new angled design performed well; however it tended to make things look somewhat askew in photographs of the test runs. This was simply an aesthetics issue; it did not affect the accuracy of the tests because there was no deviation from the vertical force line from the shaker through the specimen and the load cell. In other words, rotating the specimen to match the angle of the head of the push rod did not alter the alignment of the components.

4.2.1.4. Signal Code

This section details the Matlab code used to run the experiment. Only the portions of the code directly pertinent to this discussion are presented here; the entire code is

located in Appendix D. Figure 53 displays the first two segments of the code. These mainly contain variable inputs. *SampleSeconds* refers to the length of time of the test run, and *SampleRate* is the number of samples, for both output and input, per second. The gain, defined as *g*, is possibly the most important value in this code. This is the primary number that is altered, in an educated guess-and-check fashion, for each specimen in order to obtain the correct wing elevation. The gain relates to the amplitude of the signal's sine wave, which has a direct effect on the amplitude of the shaker's displacement.

```
%% Set the Sampling Options
SampleSeconds = 1; % Time in Seconds
SampleRate    = 2500; % Hz
SampleNumber = SampleRate * SampleSeconds; % Total Samples
SampleTime = linspace(0,SampleSeconds,SampleNumber); %Time Vector

%% Calculate output signal based on the SampleNumber of the data
g = 1.9;    % Gain (amplitude of sine wave)
bias=0;     % Bias for the shaker signal(neg. bias for pos. disp.)
OmegaDeg = 25;              % Frequency in Hz
OmegaRad = OmegaDeg*2*pi;   % Frequency in Radians
```

Figure 53 - Input for signal code

The bias occasionally proved useful. Its purpose was to alter the sine wave signal so the shaker would displace further in one direction than the other. For example, a negative bias value would induce a positive bias in the shaker's movement. The specimen would translate upward from its starting position further than it would recede down. This was often necessary if the starting position had to be a bit low in order to fit the moth into the device, as in the case of a few of the larger specimens. A low starting position meant that more vertical displacement was required to arrive at the desired compression of the thorax. Simply increasing the amplitude of the signal without applying a bias did create

the desired compression at the upper limit of motion but had the negative effect of creating a large gap between the specimen and the push rod at the lower limit. Practice runs had showed that a small gap was unavoidable and did not create problems (Figure 54), but large gaps of several millimeters would allow the specimen to vibrate out of place. In addition, large gaps induced a large impulse which was imparted to the specimen upon returning to contact with the push rod. This appeared to have adverse effects on the motion of the wings. These criteria are not necessarily quantifiable but were developed intuitively through scores of practice runs.

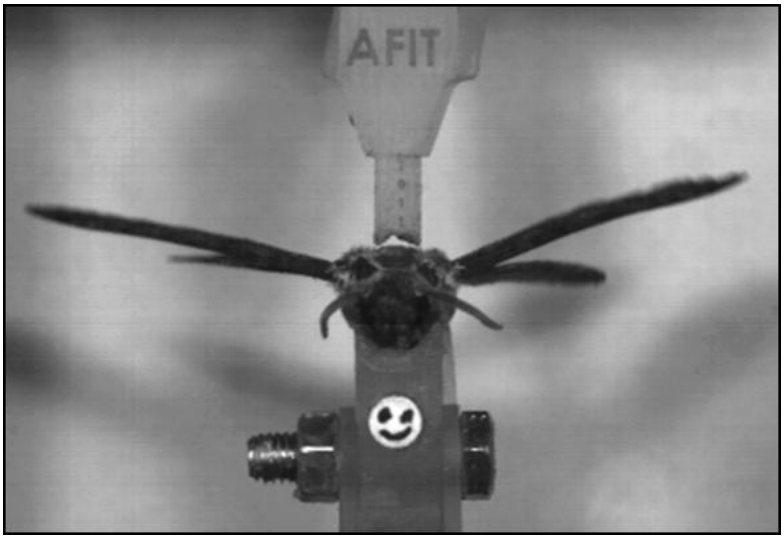

Figure 54 - Typical gap between tergum and push rod at bottom of vertical displacement cycle

The next section of the code contains the signals for the camera trigger and the shaker. The camera trigger is simple; it requires only a nonzero voltage of a high enough value to initiate video recording. Building and modifying the sinusoidal wave signal was a bit more complicated. The tare value *t* is used to determine the baseline signal from the load cell before the shaker is actuated. Refer to the caption of Figure 51 (pp.73) and to

Figure 55 for details on its usage. The sine wave signal is first created with the *sine(linspace(---))'* command, and subsequently altered with the application of the gain, bias and tare.

```
% Output 1 - Camera Trigger
data1 = 5 * ones(1,SampleNumber)';
data1(end)=0;

% Output 2 - Shaker Signal
data2=0*ones(1,SampleRate)';  %creates SampleRate:1 matrix
t=200;  % No. samples used to tare load cell before shaker starts
data2(1:t) = 0*ones(1,t);  % Signal is zero for duration of "t"

% Sinusoidal signal
data2(t+1:SampleRate) =
sin(linspace(0,OmegaRad*SampleSeconds,SampleNumber-t))';
data2 = g * data2;     % Apply Amplitude (gain)
data2 = data2 + bias;  % Apply Bias to sine wave
data2(1:t) = 0*ones(1,t);  %occurs after bias, tare remains zero
data2(end)=0;
```

Figure 55 - Output signals for camera trigger and shaker actuation

The bulk of the code following the signal definitions is used to send those signals out and read in the voltage signal from the load cell. This voltage signal then had to be converted to force (code shown in Figure 51, pp.73). Once converted, this force data was then plotted versus time. A representative plot is shown in Figure 56. Each set of upper and lower peaks represents one full flap of the wings.

4.2.2. Procedure

Each moth was weighed after being prepared for testing. The legs were then removed below the first joint to allow the body to fit snugly into the mount. A thin coating of wax between the specimen and the mount helped prevent slipping, and loop of tape over the end of the abdomen prohibited excessive movement due to vibrations during testing.

Another bit of wax on the bottom of the push rod increased friction at the contact point on the tergal plate. A mounted specimen is shown in Figure 57.

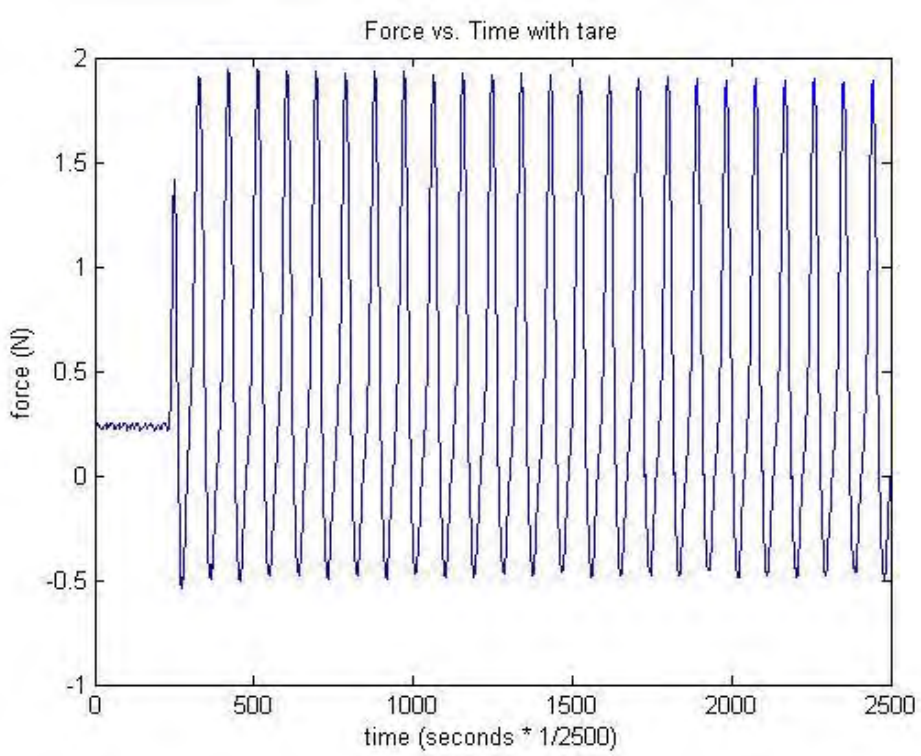

Figure 56 – Example of force versus time function obtained with the dynamic load application experiment. Note tare portion at outset of test.

Figure 57 - Mounted specimen. Note the red wax above and below the moth. The "happy face" was used track the vertical displacement. The blue rectangle with white lines is a piece of a metric ruler with mm markings, used for determining pixels to mm conversion factors.

The mount is attached to the shaker by a threaded rod, so its height was adjusted by rotating it clockwise for lowering or counter-clockwise for lifting. As each individual specimen had a slightly different mass (and therefore a different thorax size) it was often necessary to adjust this height to allow the push rod to contact the tergal plate to create the proper amount of displacement pre-load. Hundreds of practice test runs at various height positions showed that the most life-like flapping motion occurred when the neutral position of the shaker caused slight compression of the thorax. In other words, the test begins with a small compressive force already acting on the thorax and the wings elevated slightly above horizontal. This is acceptable because, as previously mentioned, the specimen will still lose contact with the push rod at the lower end of the cycle and there will be a point at which the tergum reconnects with the load cell and the force begins to swing back upward. In other words, since only the absolute increase in force during power production is desired, the only requirement is that the tergum loses contact with the push rod during each cycle. The load during the tare period will be zeroed and is therefore immaterial to the calculation of power. This idea is explained further in the processing section. Figure 57 provides a good example of the proper starting position.

The high-speed camera was then aligned with the specimen using a tripod. Two spotlights were positioned behind the camera but were not switched on until the test was ready to begin. These spotlights illuminated the specimen well enough for the camera to capture adequate images but would melt the wax around the specimen if left on for an extended length of time. The test was begun after ensuring the camera was ready to be triggered.

4.2.3. Processing

Running the signal code triggered the camera to instantly begin recording. The camera could be set to record for any desired number of frames, so after some experimentation it was determined that 1000 frames would be enough to observe a steady-state effect (refer to Figure 56, pp.78; steady state begins after only three cycles). Steady-state, in this context, refers to the equivalency of the load peaks during flapping. The shock of the shaker's sudden initiation reverberates through the first two or three cycles before the wings are moving smoothly and the peak load per cycle levels out. The processing time for 1000 frames was about 5 minutes for conversion to individual .tif files and another 5-10 minutes for tracking the vertical movement of the shaker.

4.2.3.1. Checkpoints

There were a few checkpoints leading up to data processing. The first was to examine the graph of the load and ensure the signal had not been lost or corrupted, as often occurred during practice runs due to loose circuitry before re-positioning the circuit board. Next, the video playback from the high-speed camera was observed to determine if a realistic flapping motion, with smooth wing movement with a natural wing twist, had been achieved. A sequence of video frames demonstrating a full up/down shaker cycle and the corresponding full flap of the wings is presented in Appendix I. This sequence is also marked with the initial point of contact and the point of maximum vertical displacement (maximum compression of the thorax). If the wing movement was erratic or unusual compared to natural motion, then the gain and bias of the shaker or the height and positioning of the specimen were altered and the test was run again. If the run was successful, then the angles of the leading edges of the forewings above horizontal were

examined to determine if they were within a few degrees of 55. This had initially been done by gluing small paper dots to each leading edge (refer to Figure 48, pp.72) and running a second code to trace their movement and calculate angles using the high-speed camera images, but this turned out to be very time consuming and was ultimately deemed unnecessary. Instead, a 35-55-90 degree wedge of cardboard was cut out and held against the laptop screen while the high-speed video was on slow-motion playback. There are so many parameters that must be varied for each individual specimen to achieve proper flapping that it would be ill-advised to require both wings of every specimen to reach exactly 55 degrees. Therefore, a test was considered successful if each wing came within approximately 5 degrees of the desired value, as visually confirmed with the cardboard wedge.

4.2.3.2. Processing Code

With those checkpoints cleared, the video was saved as 1000 individual .tif files so the second phase of processing could begin. These image files were placed in a folder with a copy of the code used for video processing and motion tracking (Appendix D). When run, this code reads in all of the .tif files and then asks the user to enter the number of points which require tracking and the number of image frames to be processed. This code was modified from a tracking code written by Murray, who was using his version to track over a dozen points on a flapping *M.sexta* wing (Murray, O'Hara and Palazotto 2011). The code works by computing a normalized cross correlation between one image and the next, looking for the originally selected sub-image which should have moved only a few pixels between frames. In the case of the current experiment the only pertinent motion to track was the vertical translation of the shaker and moth, so only one sub-image was

selected. A distinct shape with clear lines was found to be the most reliable tracking target, as shown in Figure 57.

The next portion of the code is a standard assembly of an .avi video file from the video frame .tif images. Coordinates from the tracking process are used here to place a marker on each frame of the video, which enables the viewer to observe the motion of the object being tracked. Again, this is a vestige of Murray's code, since in this situation it is not necessary to mark the target as it is clearly visible and the motion is entirely one-dimensional. The most useful application of the video is to pause it and click through frame-by-frame to visually verify the moment of contact between the tergum and the push rod for a given cycle (though this can be done with the original video frames as well). The point of maximum compression, which occurs when the specimen ceases to rise and begins to recede, can also be visually observed in this manner.

Finally, this code creates a plot of the vertical displacement of the selected point as a function of time. Figure 58 shows this portion of the code, which creates a zero matrix of the proper size (number of video frames) and populates it with the y-axis coordinate of the center of the selected sub-image (the target) from each frame. The result is a plot like the one in Figure 59. The value of the displacement shown on the y-axis is not as important as the absolute difference between frames. The data could have simply been converted from pixels to mm with no consideration given to the value on the y-axis. Only the absolute difference in y-location between minimum and maximum locations was necessary to determine the displacement used for power calculations. However, the plots did not make much sense without some manipulation of the data. Pixels are numbered beginning with (0,0) in the top left corner of the image and count up from

there, with the highest-numbered pixel at the lower right corner. A negative conversion value was factored into the data and the absolute value of the location of the target during the tare period was added to the entire data set. This set the starting point to zero displacement and ensured the upper peak of each cycle corresponded to the physical maximum high-point of the specimen in mm.

```
%% plot the vertical displacement
Disp = [1:998]'*0
Disp(:) = Point(1).y(:)
figure
conv=10.8 % pixels per mm
plot(1:NumFrames-1,(Disp(:)/-conv)+abs((Disp(100)/conv)))
title('Vertical Displacement over first 1000 frames')
xlabel('frame # or time (sec/2500)')
ylabel('Vertical displacement (mm)')
```

Figure 58 – Matlab code which creates a plot of vertical displacement of the specimen versus time. Note data is cleaned up with a conversion factor and the application of the tare value.

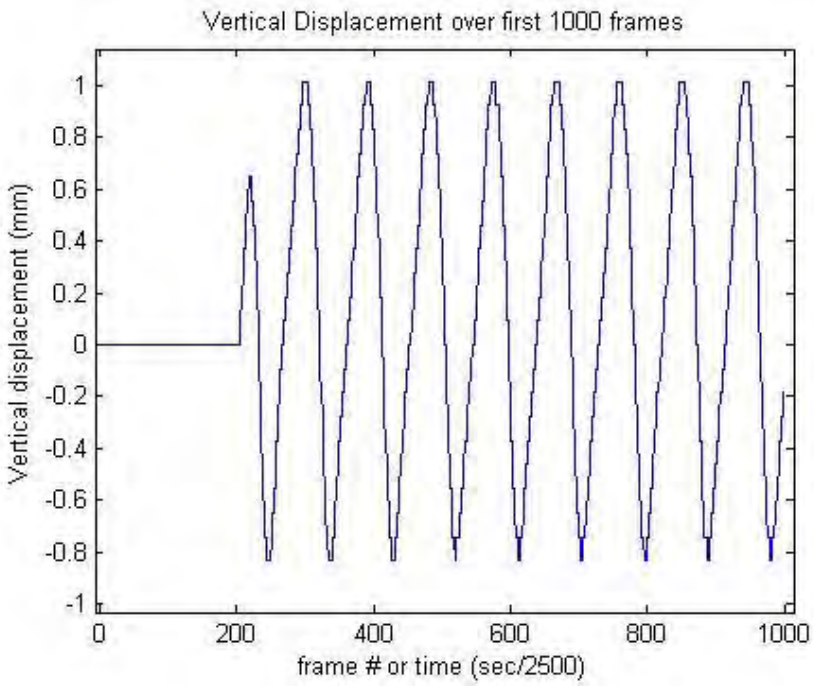

Figure 59 - Plot of vertical displacement of the specimen versus time (or frame number). A negative bias had been applied to this run, inducing a positive displacement of approximately 1mm versus a negative displacement of approximately 0.8 mm.

4.2.3.3. Power Calculation Code

All of the data necessary to calculate the mechanical power output was now available. The first step was to revisit the video and the load plot to determine the point at which the tergum made contact with the push rod.

This contact point was often evidenced by the beginning of an uptrend of the load data, though there was usually a period of fluctuating force values where the force was minimal in the first few frames of compression. It appeared that the load cell was not sensitive enough for the very low forces applied at the instant of compression initiation. Direct observation of the video frames was always used to confirm the precise frame in which the tergum contacted the push rod. Figure 60 shows a magnified view of the force plot and indicates the location of the initial contact and the point of maximum displacement. The force continues to increase after the thorax has been fully compressed because of inertial forces. The video frames were usually used to confirm the data from the plot. Initial contact was observed, within a margin of error of a frame or two, using frame-by-frame visual analysis. Compare Figure 61 with Figure 60 for an idea of where these points lie in terms of force and displacement over time.

These points, hereafter referred to as *P1* and *P2*, were then entered into the final processing code which used them to calculate power. This final code was run after ensuring that the Matlab workspaces of the signal code (with the force data) and the tracking code (with displacement data) were loaded. It begins by using *P1* and *P2*, which correspond to initial contact and maximum displacement, respectively, to create an array of displacement values which spans the period of time over which the force was applied

(Figure 62). Note that the distance is converted from millimeters to meters in order to arrive at correct units when calculating work and power.

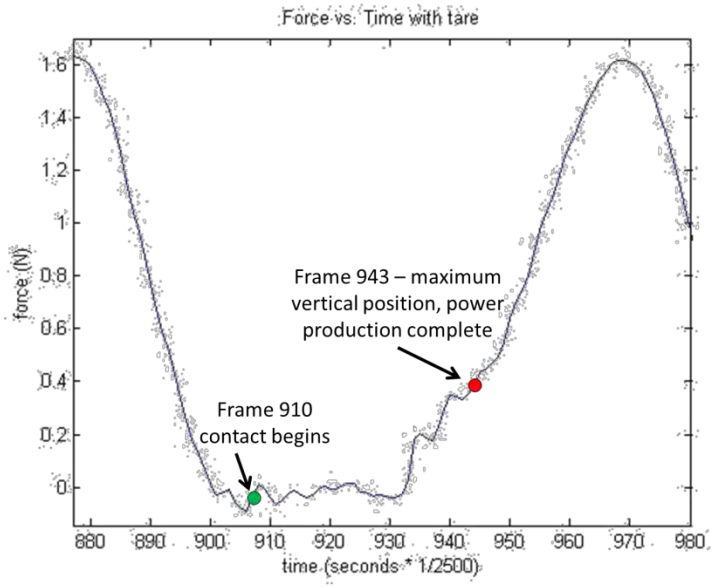

Figure 60 - Force versus time plot from Moth 7 showing initial contact point and the point of maximum powered compression. The force continues to increase after maximum displacement due to inertial forces.

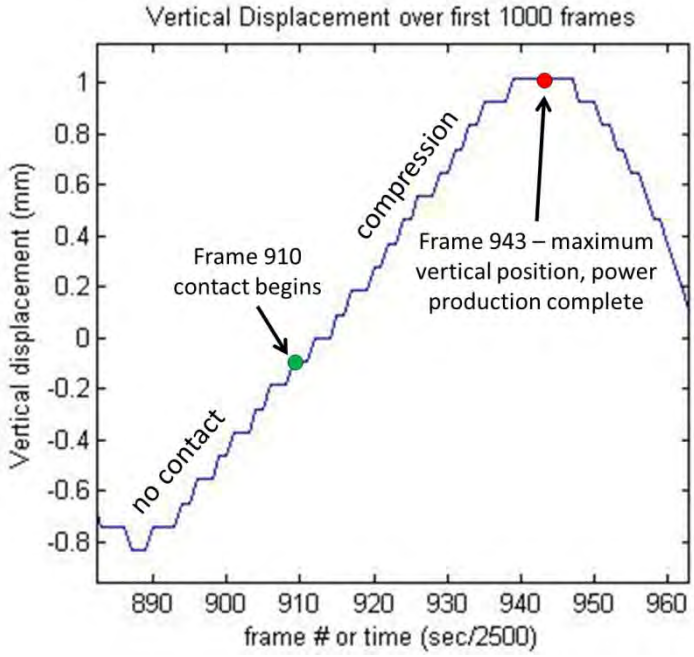

Figure 61 - Displacement of Moth 7 showing the locations used for power calculation. Note that the maximum displacement is found using this plot.

```
p1 = 904 % enter the frame in which the force begins to increase
p2 = 944 % enter the frame in which the maximum disp. occurs
%% Create array of disp. values over desired range of time
conv=4; % pixels per mm
Disp = [1:998]'*0;
Disp(:) = Point(1).y(:);
disp(1:p2-p1)=[1:p2-p1]'*0;
for i=2:p2-p1+1;
    disp(i)=disp(i-1)+(Disp(p2)-Disp(p1))/(p2-p1)/(-conv*1000);
end
D = disp'; % simplify name and invert the matrix
```

Figure 62 - Beginning of power calculation code. Inputs p1 and p2 are from the plots, and an array of displacement data is created for this data range.

Next, the force was plotted versus this displacement data for the range of time defined by *P1* and *P2*. Figure 63 shows this portion of the code. Note that the force is zeroed by setting the lowest force value (usually a negative reading based on the starting tare value being positive) to zero. Figure 64 shows a typical plot of this function and highlights the area equivalent to the work performed. Integrating this function provides the amount of work done (refer back to Figure 19, pp.33 for the theory of work).

```
%% Plot the force over distance
F = forceN + abs (min(forceN(p1:p2))); % adjusts horiz. axis
figure
plot (D,F(p1:p2))
xlabel ('Distance (m)')
ylabel ('Force (N)')
title ('Force over Distance for a Single Upstroke')
```

Figure 63 - Code portion which plots the force versus displacement. This function is then used to calculate work.

The final portion of the code (Figure 65) displays the total displacement value for record keeping and then calculates the work done by integrating the force function over the distance. This value was simply divided by the change in time over which the work was performed in order to calculate power in watts ($N \cdot m \cdot s^{-1}$).

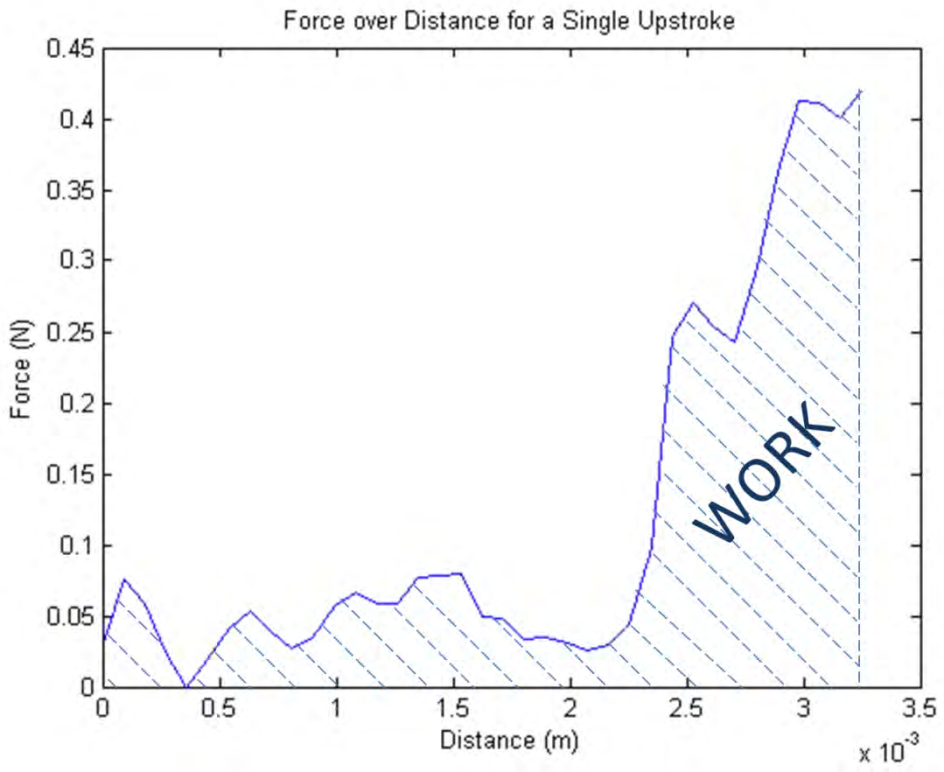

Figure 64 - Force versus displacement plot. The work done on the system (the thorax) is the integral of the force with respect to distance, or the area under the curve.

```
%% present the total displacement in mm
displacement = (D(end)-D(1))*1000

%% Integrate over this region to get the work
Work = trapz (D,F(p1:p2)) % this is the total work in Joules

%% Divide work by total time interval during application of force
time=(p2-p1)/2500 % The time interval of force application in (s)
Power = Work / time % This is what we're after!!!
```

Figure 65 - Calculation of work and power

4.3. Nanoindentation of the Tergal Plate

One of the principal objectives of this research was to thoroughly understand how *M.sexta* maintains such an energetically demanding form of flight (hovering) for extended periods of time. The dynamic load experiment investigated the mechanical power output required for flight. The static load experiment shed light on the thorax as a

mechanical spring system. The nanoindentation experiment divulged the mechanical properties of the tergum, which is a significant player in the distortion of the thoracic box during flight. In fact, the largest muscles in *M.sexta*, the DLMs, attach only to phragma at the front and rear of the tergum. Their effect when contracted is to bend the centerline of the tergum upward and depress the wings through their lift-generating downstroke. Additionally, the tergum is connected to the sternum via the DVMs, whose contraction causes it to translate downward and expand outward. Both bending motions and the DLM attachment points are indicated in Figure 66. The author believes that this bending of the tergum serves to store at least some of the inertial energy of the wings (the rest being stored in the stretched muscles or not stored at all). One of the key parameters of an engineering material, as it relates to energy storage, is the modulus of elasticity. With this in mind, the elastic modulus of the tergal plate of *M.sexta* was examined with nanoindentation.

4.3.1. Equipment

A Nano Instruments® MTS Nano G200 nanoindentation machine was used in conjunction with the software program TestWorks for this experiment.

4.3.2. Test Settings

The TestWorks software comes equipped with preset test methods. A method called "G-Series CSM Hardness, Modulus for Thin Films" was chosen for this experiment because it was hypothesized that the modulus may not be consistent throughout the thickness of the tergum and it would therefore be favorable to measure the modulus as a function of depth. Table 2 contains the settings and the user inputs and explains any changes that were made to the standard values.

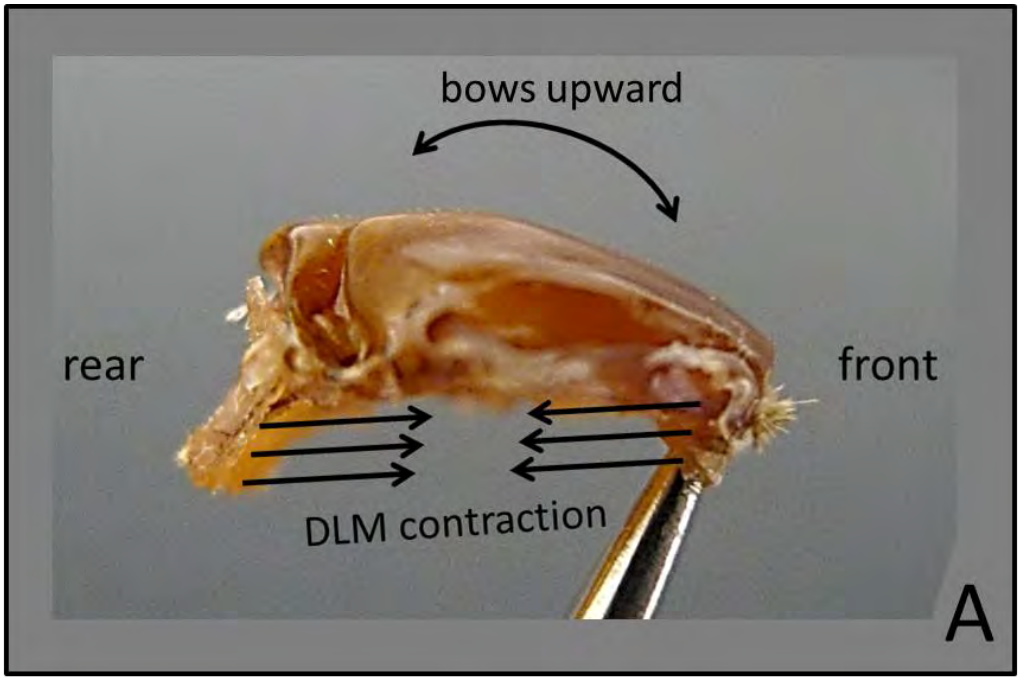

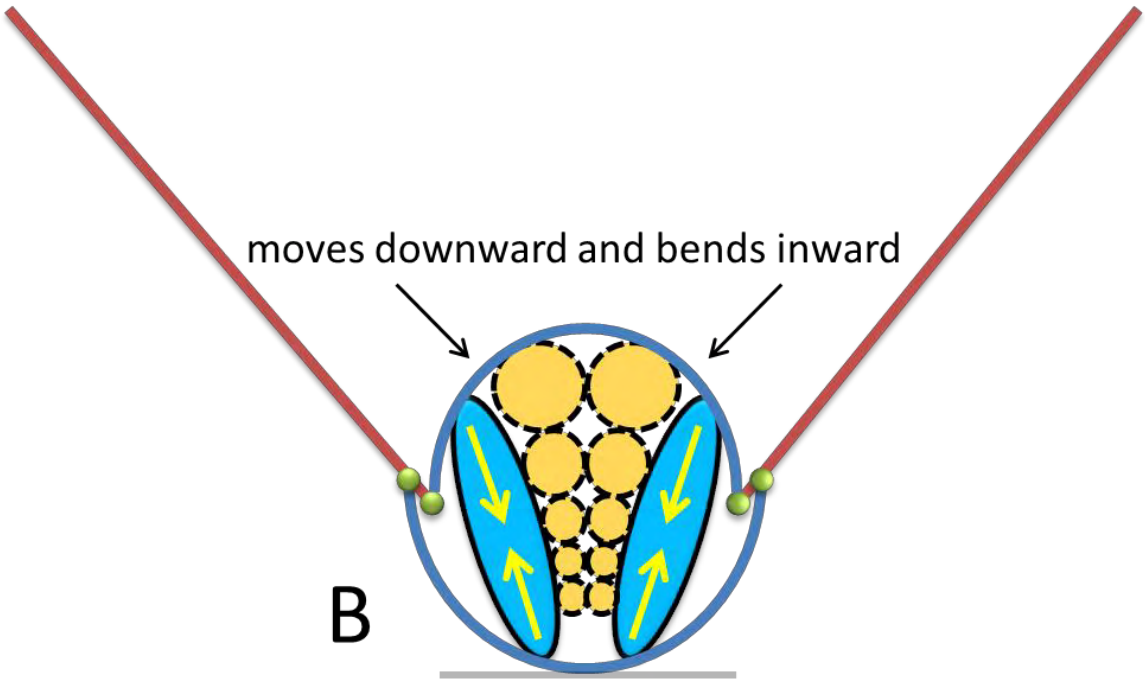

Figure 66 - Representations of tergum movement during flight. **(A)** Side view of actual tergum; dorsolongitudinal muscle contraction bows the center of the tergum upward and depresses the wings. **(B)** Dorsoventral muscle contraction (yellow arrows on blue) brings the tergum toward the sternum and bends the sides of the tergum inward to induce wing elevation.

Table 2 - Nanoindentation settings and user inputs

Settings	value	unit	changed?	original	reason for change
delta X for finding surface	50	um	no	-	
delta Y for finding surface	50	um	no	-	
allowable drift rate	5	nm/s	yes	0.05	Allowable drift rate must be satisfied before test begins. Smaller values require much more time and do not significantly affect the accuracy.
surface approach distance	1000	nm/s	no	-	
surface approach sensitivity	25	%	no	-	
surface approach velocity	5	nm/s	no	-	

User Inputs	value	unit	changed?	original	reason for change
depth limit	2000	nm	yes	500	Original depth not enough to allow data to converge.
strain rate target	0.05	1/s	no	-	
harmonic displacement target	2	nm	no	-	
frequency target	45	Hz	no	-	
poisson's ratio	0.32		yes	0.18	The tergum is made of a relatively soft and elastic material.

4.3.2.1. Indentation Depth

The maximum indenter depth was initially set to a standard 500 nm ($500x10^{-9}$m), but erratic readings caused by the irregularity of the surface and the inherent variability of the natural material meant that the elastic modulus values of the various sample points did not visibly converge at this depth (Figure 67). The machine is very sensitive to surface detection, and requires an extremely smooth surface to work well, especially at shallow depths. Biological materials like the tergum are not as smooth or polished as they may appear. This causes the machine to produce erratic results as the indenter tip penetrates the first one or two hundred nanometers surface, only approaching the true modulus as the indentation begins to take shape. It was therefore necessary to set the indentation

depth deep enough to capture a steady and consistent set of data from a majority of the sample points.

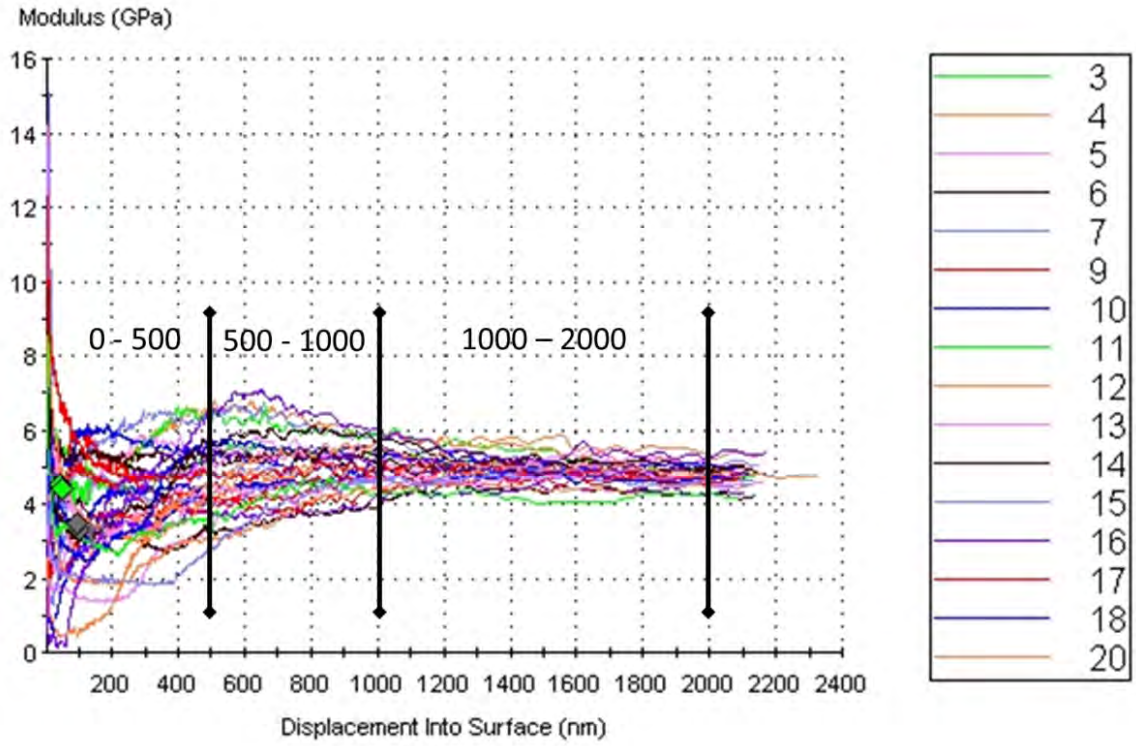

Figure 67 - Modulus versus penetration up to 2000 nm. Convergence improves significantly beyond 1000 nm.

Sun et al. indicated that the depth of indentation should not exceed 10% of the thickness of the specimen (Sun, Tong and Zhou 2006). Examination of the cross-section of the tergal plate, using a Zeiss StereoV12 microscope, showed the thickness of the tergal plate to be about 28 µm (Figure 68). Therefore, a depth of 2000 nm was selected for the indentation tests, which allowed better convergence to the true average value of the modulus of elasticity (Figure 67) without exceeding the 10% depth limit. This depth is entirely within the outermost major cuticle layer, the epicuticle, which is close to 3 µm thick. However, the resulting elastic modulus readings can be said to characterize the entire thickness of this multilayered composite material (Barbakedze, et al. 2006).

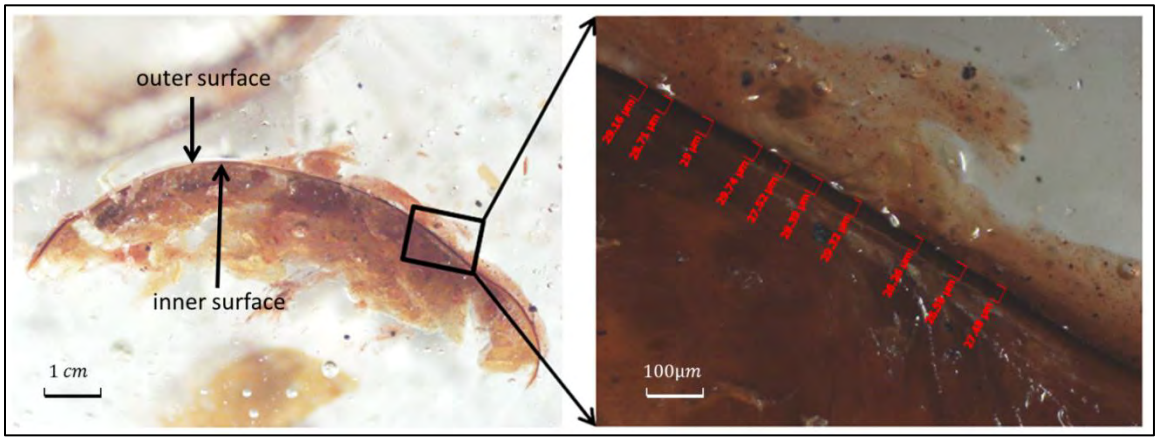

Figure 68 - Cross-section of the tergum. The subject was excised from a specimen and immediately encased in Crystalbond, a thermoset polymer described in subsequent sections of this document. The surface of the cross-section was polished until smooth which enhanced microscopic viewing. The thin, dark line is the tergum and the rest of the tan/brown material is muscle. The red markings on the right indicate locations where the thickness was measured with the microscope's software.

4.3.2.2. Number of Sample Points per Test Run

Practice runs using a 5x5 grid of sample points spaced 20 microns apart showed aberrant results were common, providing erroneous data for up to two-thirds of the sample points. This is due largely to the irregular surface of the tergal plate. The surface of the tergum is very rough and is covered with scale follicles (Figure 69) and if the indenter head contacts these holes it has a very low chance of providing reliable data, especially surface detection. Therefore, in order to ensure each run produced a large enough number of accurate sample points, the grid was increased from 5x5 to 6x6. These 36 sample points generally ensured at least 20 acceptable data sets.

4.3.3. Sample Preparation

Desiccation of biological materials such as insect cuticle causes material modification in the form of hardening and stiffening (Enders, et al. 2004). Therefore every effort was made to keep the specimen preparation period as short as possible. Many of these

specimens were first used for the dynamic load experiment and then quickly prepared for experimentation in the nanoindenter. These tests were initiated within an hour of the removal of the tergum from the specimen, though a set of 36 sample points took anywhere from 3-8 hours to run once begun.

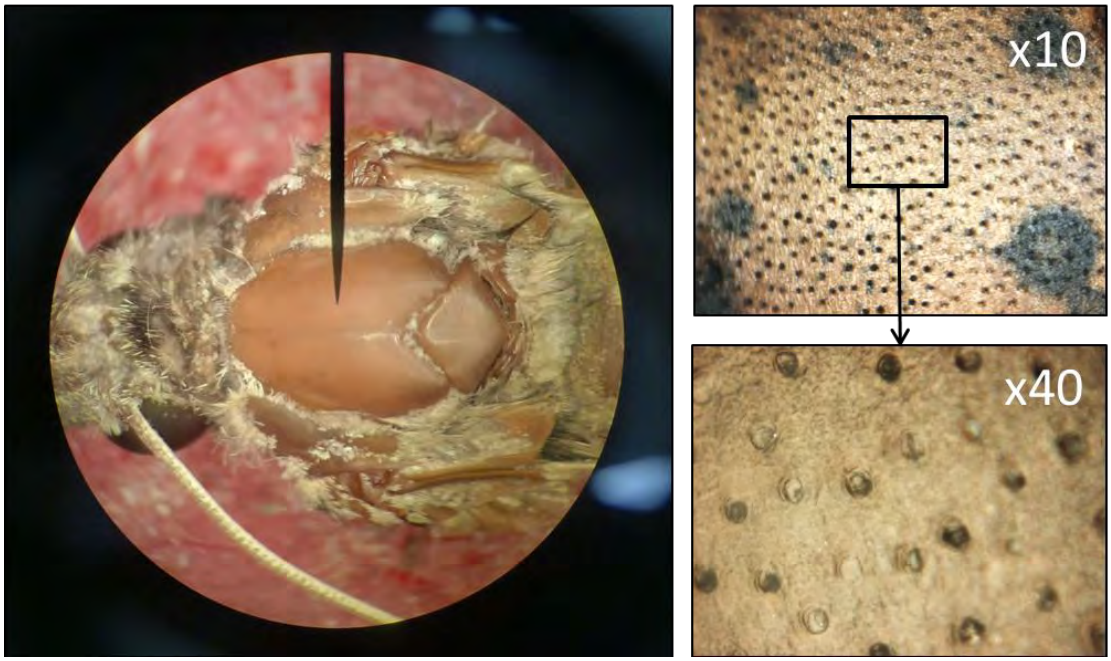

Figure 69 - Magnification of outer surface of tergum. The scales have been brushed off, leaving an apparently smooth surface which actually quite rough. The microscopic images on the right were captured with the Nano Indenter G200's video handset feature.

Repeated tests on the same specimen, performed hours and days after the initial test, showed little change in the modulus of elasticity. In fact, significant stiffening was not apparent until two weeks after the initial test of one of the specimens. This is not too surprising as the tergum is a major component of the exoskeleton and as such is relatively hard and stiff. Its water content is likely not as high as that of the cuticle in a more flexible hinge region. It was assumed that the elastic modulus data would be acceptable for all tests performed within 24-48 hours of preparation.

4.3.3.1. Isolating the Tergum

The tergal plate was removed from an *M.sexta* specimen using a combination of scalpel and surgical scissors. The DVMs were challenging to remove as they are connected along the entire left and right side of the inner surface of the tergum. Removal of the DLMs was easier to manage because they only attach at the phragma at front and rear of the tergum (see Figure 70). These extensions of the tergum can be snipped off with scissors and removed, taking the DLMs with them. The entire inner surface of the tergum was cleaned by carefully scraping with tweezers under running water.

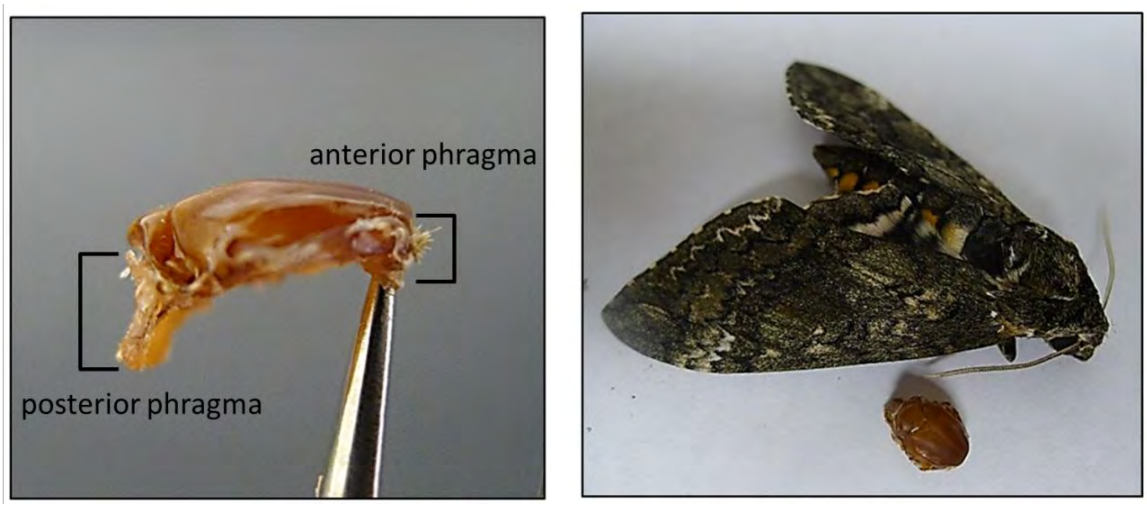

Figure 70 - *M.sexta* tergum side view and comparison with intact specimen. The phragma are extensions of the cuticle which support the dorsolongitudinal muscles. Despite how it may appear, the tergum is essentially all one continuous piece.

4.3.3.2. Mounting with Crystalbond Hot Melt

The nanoindenter uses standard aluminum pucks for mounting specimens. The tergum of *M.sexta* is a relatively large, three-dimensionally curved shape and cannot be mounted on the puck like a standard thin film of metal or polymer. At first glance, the solution seems to be simply gluing the entire thorax to the puck. However, this could potentially contaminate the stiffness data because the stiffness of a thin specimen can be influenced

by the properties of the substrate beneath it. Therefore it is necessary to isolate the tergum from the rest of the system in order to find the elastic modulus of the tergum only. It must be mounted in such a way that the supporting material below it is extremely stiff and immobile (unlike the thorax). Several methods, including cutting the tergum into small, nearly flat portions and gluing them to glass slides, failed to produce consistent results. Finally, a successful solution was devised involving a thermoplastic polymer called Crystalbond Hot Melt.

The MTS Nano G200 manual suggests a standard procedure of using Crystalbond Hot Melt to mount glass slides to the pucks. Material samples can then be adhered to the glass slides (MTS 2007). The use of Crystalbond makes cleanup and re-use of the pucks simple. It softens at 71℃ and flows at 135℃, and is rigid at room temperature. Removal of a specimen is as simple as reheating the puck until the Crystalbond softens. It can also be dissolved with acetone.

Bypassing the glass slide, the tergum was mounted directly to the aluminum puck using Crystalbond. The thermoplastic properties allowed the tergum to be pressed into a quantity of the polymer so that the entire cavity was filled. This completely supported the tergum while leaving the top surface clear for indentation (Figure 71). The mounted specimen was now secure and positioned so that center of the tergum was level and clear of debris, suitable for nanoindentation tests.

4.3.3.3. Positioning in Machine

The puck with the specimen was then placed into a slot on the sample tray inside the machine and lowered until the upper surface of the tergum aligned with the standard sample in the center of the sample tray. Aligning the upper surface of each specimen to

the same level ensured that the microscope would already be nearly in focus which simplified the testing location procedure.

Figure 71 - Tergum mounted to puck with Crystalbond Hot Melt. The thermoplastic polymer completely fills and supports the cavity created by the removal of the flight muscles. The tergum is thin enough for light to pass through, giving the specimen the appearance of amber.

4.3.3.4. Finding an Adequate Testing Location

A microscope, with either 10x or 40x magnification, was used to examine the surface to find a suitable testing location (Figure 72). The craters in the surface are follicles from which the scales emerged. Erroneous measurements resulted any time the indenter head contacted one of these craters, but it was not possible to find a testing location free of the follicles. The main criterion for a good testing location was its "flatness." In other words, if the majority of the magnified image was in focus then the area was assumed to be level enough to produce many good samples. Any significant slope would cause the indenter head to contact the surface while translating between sample points, thereby aborting the test.

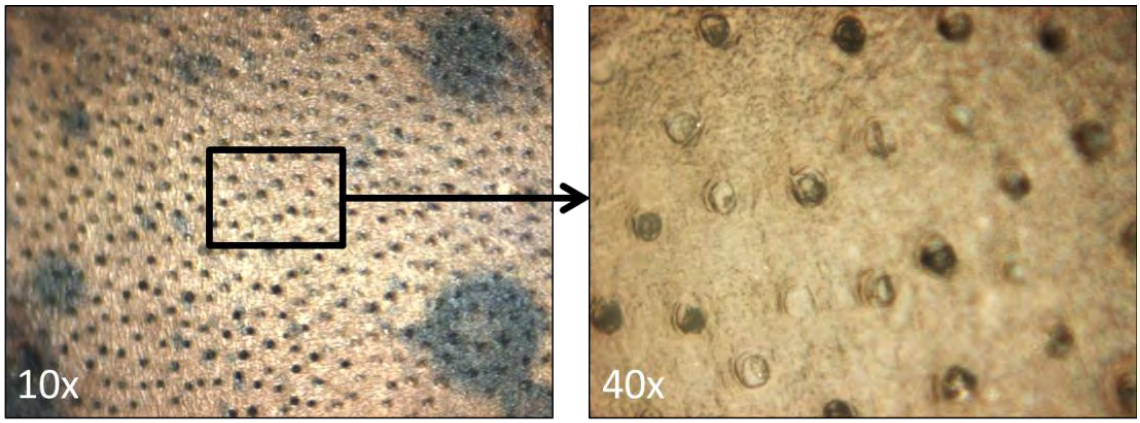

Figure 72 - Magnification of tergum using the Nano Indenter G200's video function. The top left corner of the 10x image is out of focus, which was a common due to the curved structure of the tergum. The flattest portions of the tergum were evidenced by an image in which the entire frame was in focus. When defining an array of sample points, the first point was located at the center of the image and the array was populated down and to the right.

4.3.4. Processing

TextWorks presented the results from a test run with a plot of the elastic modulus over displacement into the surface for each sample point. The average elastic modulus over the entire indentation depth of each sample was also presented, as well as an average value of all samples from that test run. However, these numbers could not be relied upon because of the erroneous data near the surface due to the inherent variability of the biological surface. It was clear that most of the sample points produced widely varying modulus values for the first couple hundred nanometers of penetration depth, due to difficulty in surface detection or anomalies on or near the surface. Most sample points converged to a relatively steady-state value at or around 500 nm of penetration. The software's average modulus value includes all of the data points from each run, including the errant readings from the shallow indentation depths. Since the desired result is the true average modulus of the material, that steady-state body of data beyond 500nm needed to be examined with the initial portion of the data removed. In addition, each run resulted in at least a few, and

often more than a dozen, erroneous samples (Figure 73) These data sets either did not come close to convergence with the majority or had a nonsensical average modulus. For example, if 28 of 36 sample points converge to approximately 5 GPa and a few of the other sample points yielded moduli of 0.5, 2, or 12 GPa, those were removed from consideration of the compiled average. The remaining five sample points in this hypothetical example were failures, that is, they failed to produce data, which was a common problem due to the uneven surface of the tergum. This selection process is described in the following section.

4.3.4.1. Eliminating Aberrant Samples

The TestWorks program produces an interactive plot of the results of the test. Selecting all of the samples plotted all data (part A of Figure 73). Often, an aborted sample point, which produced no data, was "flagged" by the program. These were deleted first. Next the aberrant samples were eliminated individually using the following procedure. Individual samples can be added or removed from the group plot, so it was possible to visually confirm whether or not a given sample was trending with the majority or was obviously erroneous. The average elastic modulus value of each sample point is produced by the software; an extremely small (sometimes negative!) or large average was cause for concern. If a sample did not converge, converged too late, or converged to a value far from the majority's convergence, it was deleted. When only the converging results were left (part B of Figure 73), the data was saved again and exported to Excel, where the data from each sample point was loaded onto a separate sheet. A Matlab code was written to process this data and ultimately determine the average modulus of elasticity for each test.

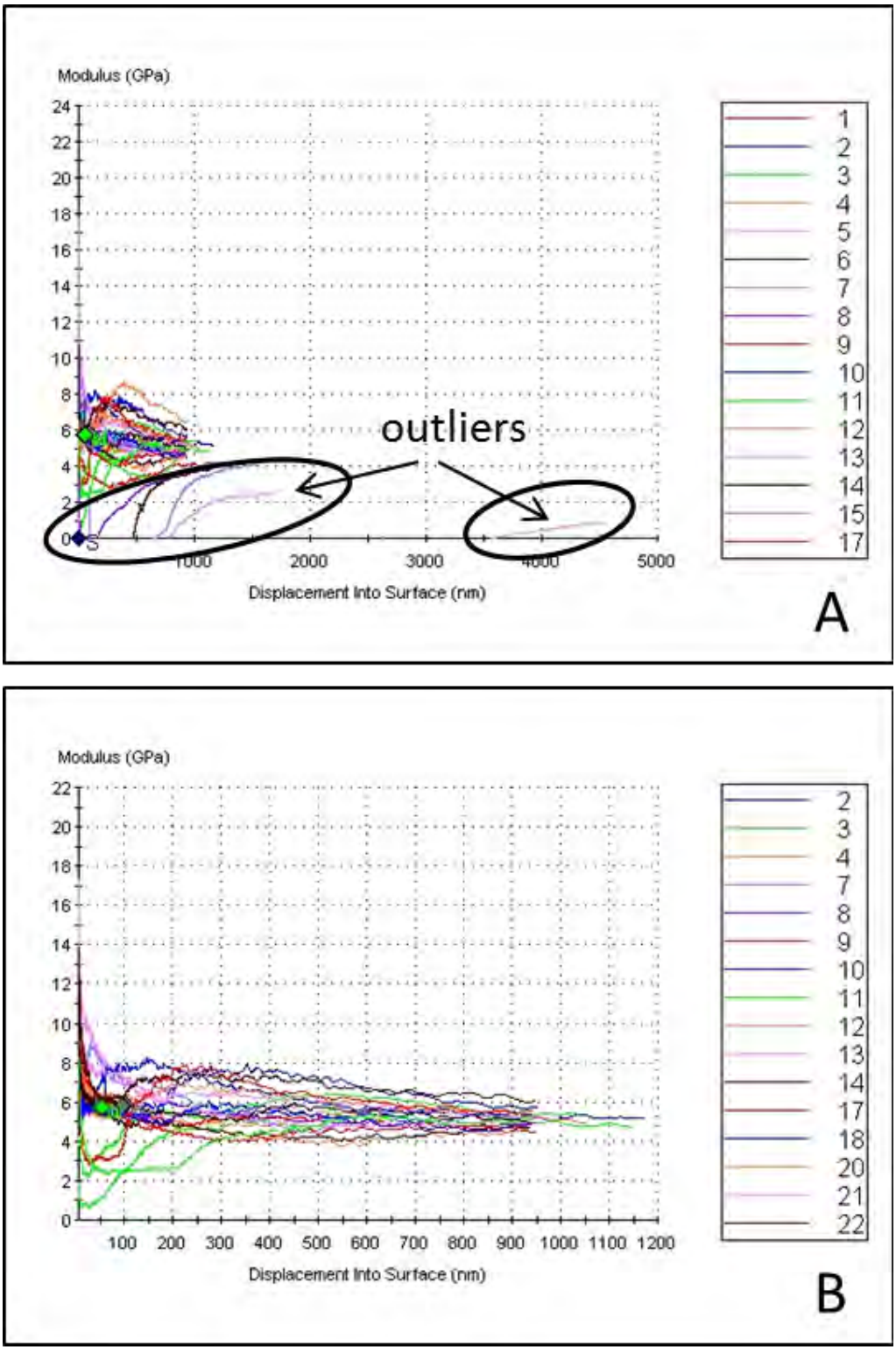

Figure 73 – Importance of removal of aberrant sample points from the results. **(A)** Plot of all 36 of the data sets from a test performed at 1000 nm depth. **(B)** Same test with 14 aberrant data sets removed. Notice the scale changes significantly due to the removal of the outliers and the grouping of the results becomes apparent.

4.3.4.2. Calculating the Average Elastic Modulus with Matlab

The entire nanoindentation processing code is presented in Appendix F. This code established communication between Matlab and the Excel file and specified which data to read in (Figure 74).

```
%% Load Excel File
filename='T6t15days.xls'; % Tergum#test#.xlsx
[status,sheets] = xlsfinfo(filename);

n = length(sheets); % Number of Samples + 3
min = 733; %Low end of data (750-850 gives 1000-2000nm range)
max = 845; % Highest number before end of data in excel file
for i=4:n
    [data, labels] = xlsread(filename,sheets{i});
    % Process the Excel File
    data      = data(:,:);
    Test(i).Depth    = data(min:max,1); %Specify range and column
    Test(i).Modulus  = data(min:max,6);
    % Calculate the Mean Modulus for each test run
    Test(i).MeanModulus = nanmean(Test(i).Modulus);
end
```

Figure 74 - Beginning of nanoindentation data processing code. Matlab makes contact with Excel and reads in the data specified by the min-max range of columns 1 (depth) and 6 (modulus). The for-loop also calculates the mean value for the modulus data for each sample point or run.

Because the machine is completely automated and adjusts its parameters (such as rate of indentation) according to constant feedback, the individual sample points did not necessarily have the same number of depth readings. The 1000-2000 nm depth readings for point 1 might be contained in rows 700-800 of the excel table, meaning that 100 readings characterized those 1000 nm of depth for that sample point. The same portion of another point's depth might be contained in rows 750-950, meaning that the indenter was moving more slowly and had gathered 200 readings over the same depth range, probably due to difficulty in the surface-finding stage of the test. The *max* value entered into the

code in Figure 74 must not exceed the maximum row of any of the sample points, so its value had to be adjusted for each indentation test. The same factors played a role in the selection of the lower limit. This was a bit more forgiving as any number less than *max* would work. Practice runs showed that a *min* value of around 700-750 and a *max* of about 850 would get most of the data in the 1000 nm to 2000 nm range without causing any errors. Errors were normally fixed by lowering the *max* value.

The final step was to find the average value of all of the individual indentations from a given set of 36, accomplished with a simple for-loop (Figure 75). Finally, as a sanity check, a plot of the modulus versus depth was created from the specified data set in order to examine whether the choice of *min* and *max* made sense (Figure 76). Occasionally, a plot would show one set of data that was nowhere near the rest, in which case the individual samples had to be revisited to make sure an erroneous sample did not get passed by in the processing stage.

```
%% Compute the average from all runs
sum = 0;
for i=4:n
    Test(i).MeanModulus
    sum = sum + Test(i).MeanModulus;
end
Average = sum/(n-3)
 %% Plot the Modulus vs. Depth data
for i=4:n
    x=Test(i).Depth;
    y=Test(i).Modulus;
    plot(x,y,'.-')
    hold on
    grid on
    xlabel('Depth into Surface (nm)')
    ylabel('Modulus of Elasticity (GPa)')
    title('All Tests')
    orient landscape
    %print(h,'-djpeg',['Test Number' num2str(i)]);
end
```

Figure 75 – Portion of code which calculates average modulus for the entire test then plots the original data as a failsafe

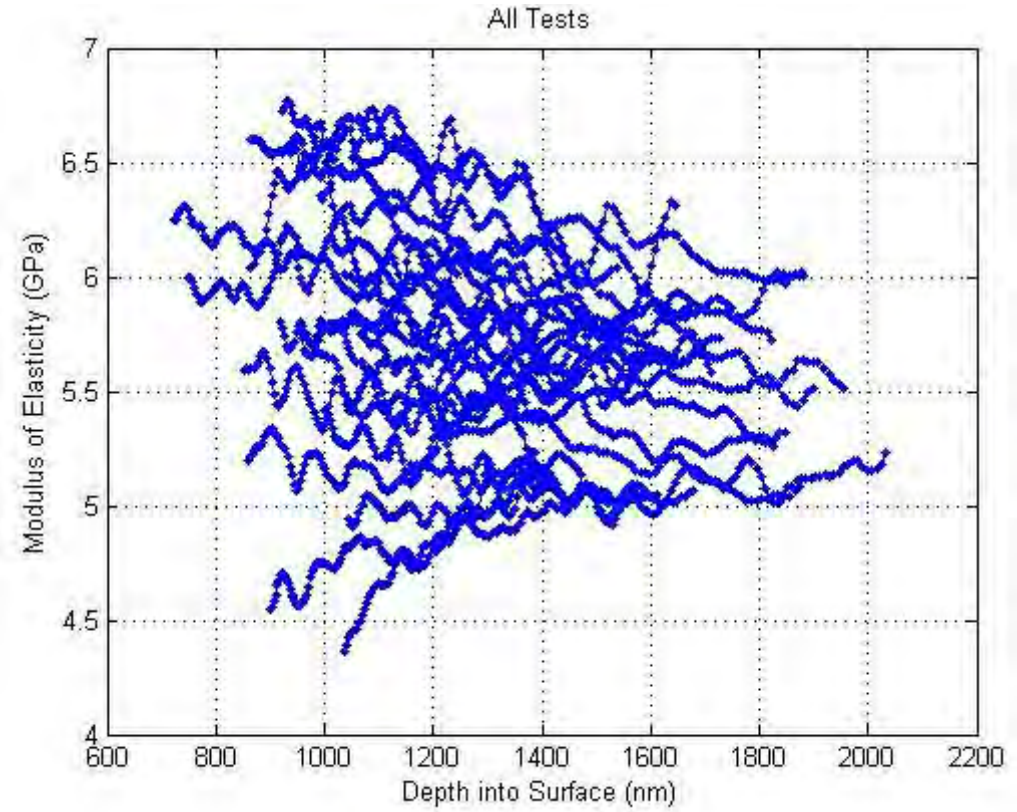

Figure 76 - Modulus versus depth into surface over the range specified by *min* and *max*. This plot was used to ensure grouping of results was acceptable. Occasionally, data from an errant sample point would make it through the elimination phase but would show up here as a major outlier.

5. RESULTS

Results of the three experiments are presented and discussed in this chapter. The significance of these results is explained in Chapter 6. The static load experiment is covered first (5.1) because it was the first investigation to be carried out. The nanoindentation experiment is presented second (5.2), followed by the results of the dynamic load experiment (5.3).

5.1. Results – Static Load Experiment

The data from the first round of the static experiment (mentioned in Chapter 4.1.2.2, pp.61) is not meaningful and is not included in the content of this chapter. Its load data is

inaccurate as those numbers were based on the total weight on the weight platform and not on the actual load transferred through the thorax. However, lessons from this iteration opened the door for numerous improvements for the final experimental setup, including the addition of the load cell for force measurement and the collection of vertical compression data. The complete results from this round of testing, including compilation and averages, are given in section 1 of Appendix G. All results presented in this chapter are from the second iteration which employed the load cell.

5.1.1. Static Load Experiment with Load Cell

During the course of the initial iteration it had been determined that, while the wing angle and force relationship may be interesting, a more fitting characterization of the mechanical nature of the thorax/wing system would be the energy storage rate within the entire thorax/wing mechanism. This led to recording the compression of the thorax in addition to the wing angle for each applied force. The addition of the load cell for force measurement also greatly contributed to the effectiveness of this version of the experiment. Figure 77 shows an example of the linear correlation between the applied force and the compression of the thorax, while a wing angle versus force plot is given in Figure 78. In total, four *M.sexta* specimens were examined; complete results are given in section 2 of Appendix G.

A compilation of the compression data is presented in Figure 79. A clear linear correlation is readily apparent. This data was plotted as one function and fitted with a linear curve (Figure 80).

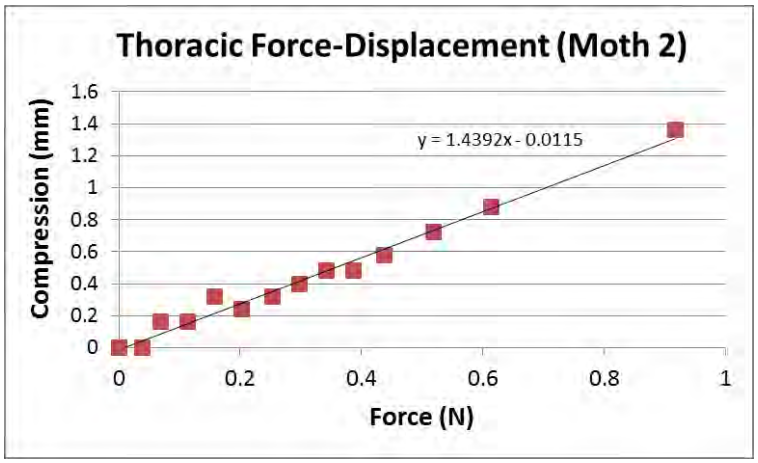

Figure 77 - Example of the compression of the thorax related to the force applied to the tergum.

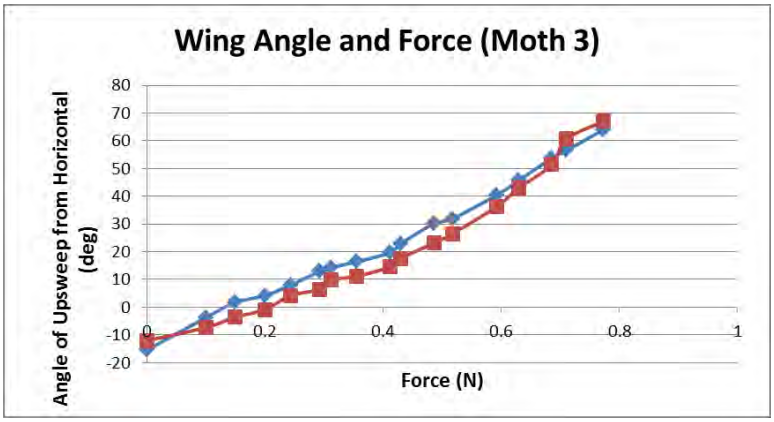

Figure 78 - Example of the wing angle induced by the applied force during the second iteration of the static load experiment. Here, the load data was accurately recorded with a load cell.

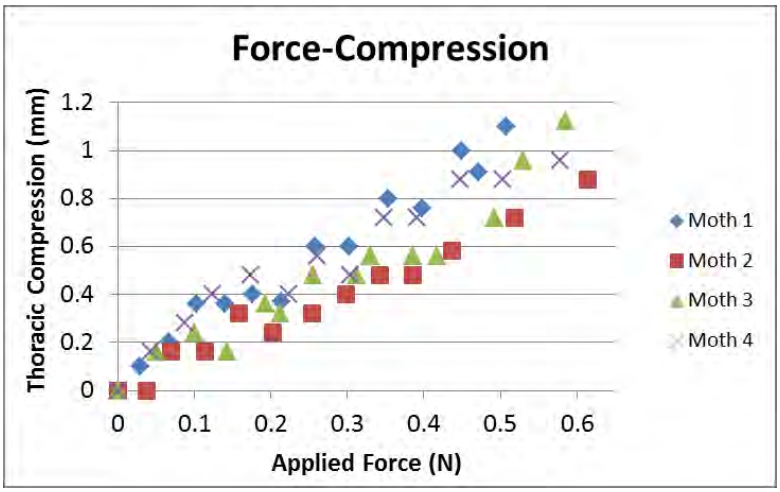

Figure 79 - Compilation of all force-compression data from the second iteration of the static load experiment.

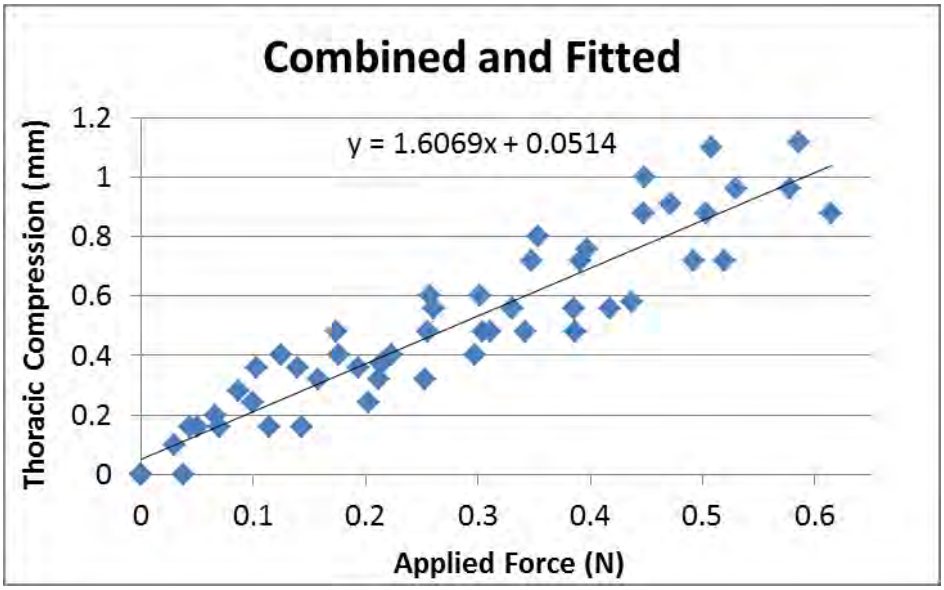

Figure 80 - Combined load vs. compression data with linear fit

All of the wing angle and force data from the four specimens is given in Figure 81. The angle data were adjusted so that each wing began at zero elevation. The vertical axis then became the absolute increase in angle from the starting position of each wing. The average wing angle from all four specimens is shown in Figure 82.

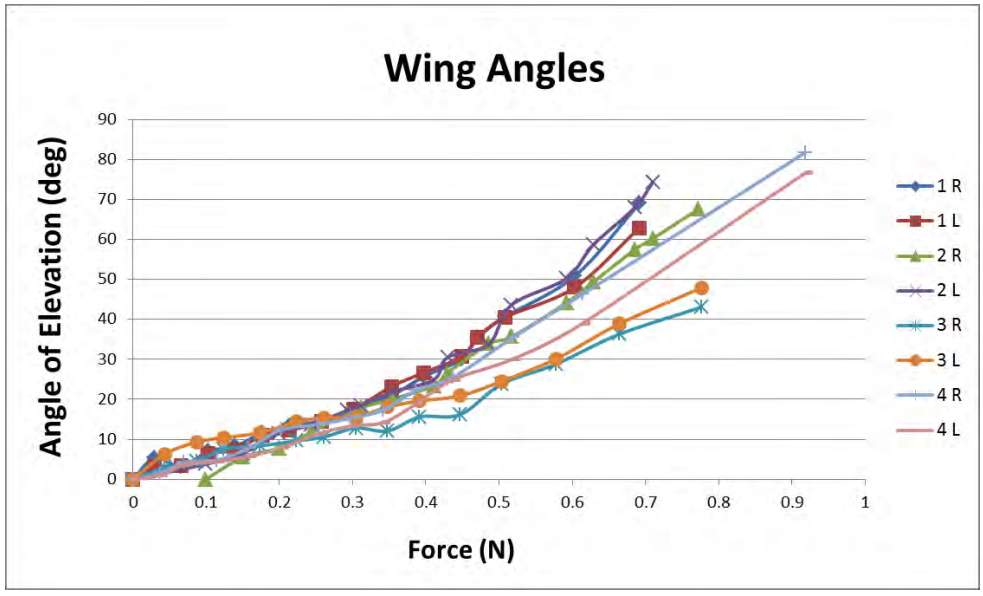

Figure 81 - Combined wing angle data from static load experiment

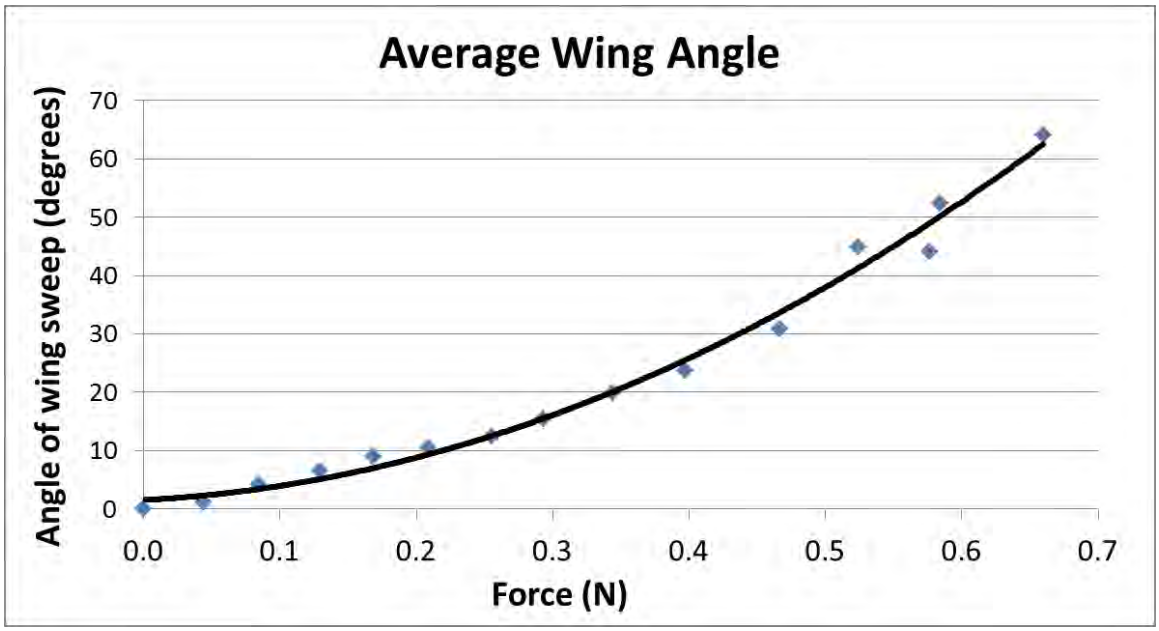

Figure 82 - Averaged wing angle data from static load experiment

5.1.1.1. Linear Spring Constant

The linear correlation of applied force and compression of the thorax enabled calculation of a linear spring constant *k* (also referred to as *stiffness*) for the thorax/wing system. The equation of the linear curve fitted to the data (Figure 80, pp.105) is:

$$\boldsymbol{x = 1.6069 \cdot F - 0.0514} \quad (48)$$

where *x* is the displacement (or compression) of the thorax and *F* is the applied force. The stiffness *k* of the system is equivalent to *F/x* (from Eqn. 1, pp.32). Thus, *k* is the inverse of the slope of this line:

$$\boldsymbol{k = \frac{F}{x} = \frac{1(N)}{1.6069(mm)}} \quad (49)$$

$$\boldsymbol{k = 0.6223\ \frac{N}{mm}} \quad (50)$$

which means the thorax, viewed as a mechanical system, requires an applied force of approximately 0.62 N per mm of compression. This value does not directly transfer into the dynamic load application, but may still find use as a benchmark for comparing man-made flapping devices for FWMAVs. Developers of finite element models of the hawkmoth thorax will also make use of this information when evaluating their models (Demasi, Palazotto and Hollenbeck 2012).

5.1.1.2. Evaluation of Wing Angle vs. Force

A theoretical evaluation of the relationship between wing angle, force and thoracic compression was carried out to confirm that the angle-force plot (Figure 82, pp.106) was realistic. Figure 83 presents a schematic of a wing/hinge/thorax linkage and the forces involved in flapping. A few assumptions must be made for this model to describe the actual system. First, the hinge is simplified as a pivot point instead of a complex region of sclerites (small plates of tanned cuticle) within a stretchy resilin matrix. Additionally, the mass of the wing is located at the wing's center of mass, which is located an arbitrary distance L from the hinge. The compressive force F represents the force applied by the push rod to the thorax (or by the DVMs during flight), and is located a short, arbitrary distance d inside the thorax from the hinge.

The goal of the following exercise is to arrive at an expression for force F in terms of angle θ and to compare that funciton to the result of the static load experiment given in Figure 82. We begin by equating the moments from the applied force and the gravitational force of the wing through the wing center of mass for this static scenario:

$$\boldsymbol{M_{wing} = M_{applied}} \quad (51)$$

$$\boldsymbol{m_{wing} g L \cos\theta = F d} \quad (52)$$

where $F = kx$, L is the location of the wing center of gravity, and m_{wing} is the mass of the wing. Theta is the wing elevation angle from horizontal. Refering to Figure 83, trigonometry yields:

$$\boldsymbol{d = \frac{x}{\sin\theta}} \quad (53)$$

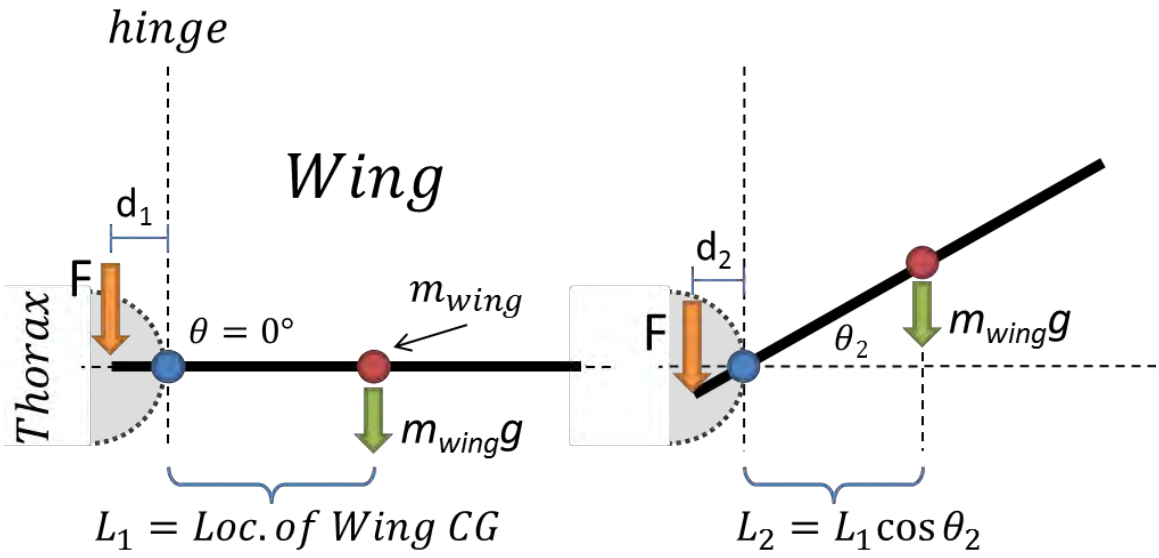

Figure 83 - Theoretical representation of the wing and hinge mechanism. The centroid of the wing is located at the red dot, which is distance *L* from the hinge. The push rod (or a DVM) applies a force *F* to the base of the wing, located a distance *d* from the hinge. The weight of the wing *mg* acts as a force through the center of gravity, which must be counterbalanced by the applied force *F*.

Plugging $F = kx$ and Eqn. 53 into Eqn. 52 yields:

$$\boldsymbol{m_{wing} g L \cos\theta = kx \cos\theta \frac{x}{\sin\theta}} \quad (54)$$

Simplifying Eqn. 54 by eliminating the cosine terms and isolating the x terms yields an expression for x in terms of θ:

$$x = \sqrt{\frac{m_{wing} g L \sin\theta}{k}} \quad (55)$$

All of the terms in Eqn. 55 except x and θ are constants, so its reduced form is:

$$x = C_1 \cdot \sqrt{\sin\theta} \quad (56)$$

Therefore the displacement or vertical compression of the thorax varies with the square root of the sine of the subsequent wing elevation angle. Since the applied force is equivalent to the spring constant k multiplied by the displacement x (Eqn. 1, pp.32), it can also be shown that the force varies in the same manner as the displacement:

$$F = kx = kC_1 \cdot \sqrt{\sin\theta} \quad (57)$$

$$F = C_2 \cdot \sqrt{\sin\theta} \quad (58)$$

Figure 84 shows the Eqn. 58 plotted with $C_2 = 1$ for simplicity and compares it to the force-angle data from the second iteration of the static load experiment. The experimental results appear to exhibit a similar trend to the plot of Eqn. 58. The trend from the first iteration, with no load cell, was significantly different (see Appendix G, section 1). This demonstrates that the use of the load cell improved the outcome of this

experiment and that the resulting 2nd-order fit is an appropriate approximation of the real wing angle response to DVM loading.

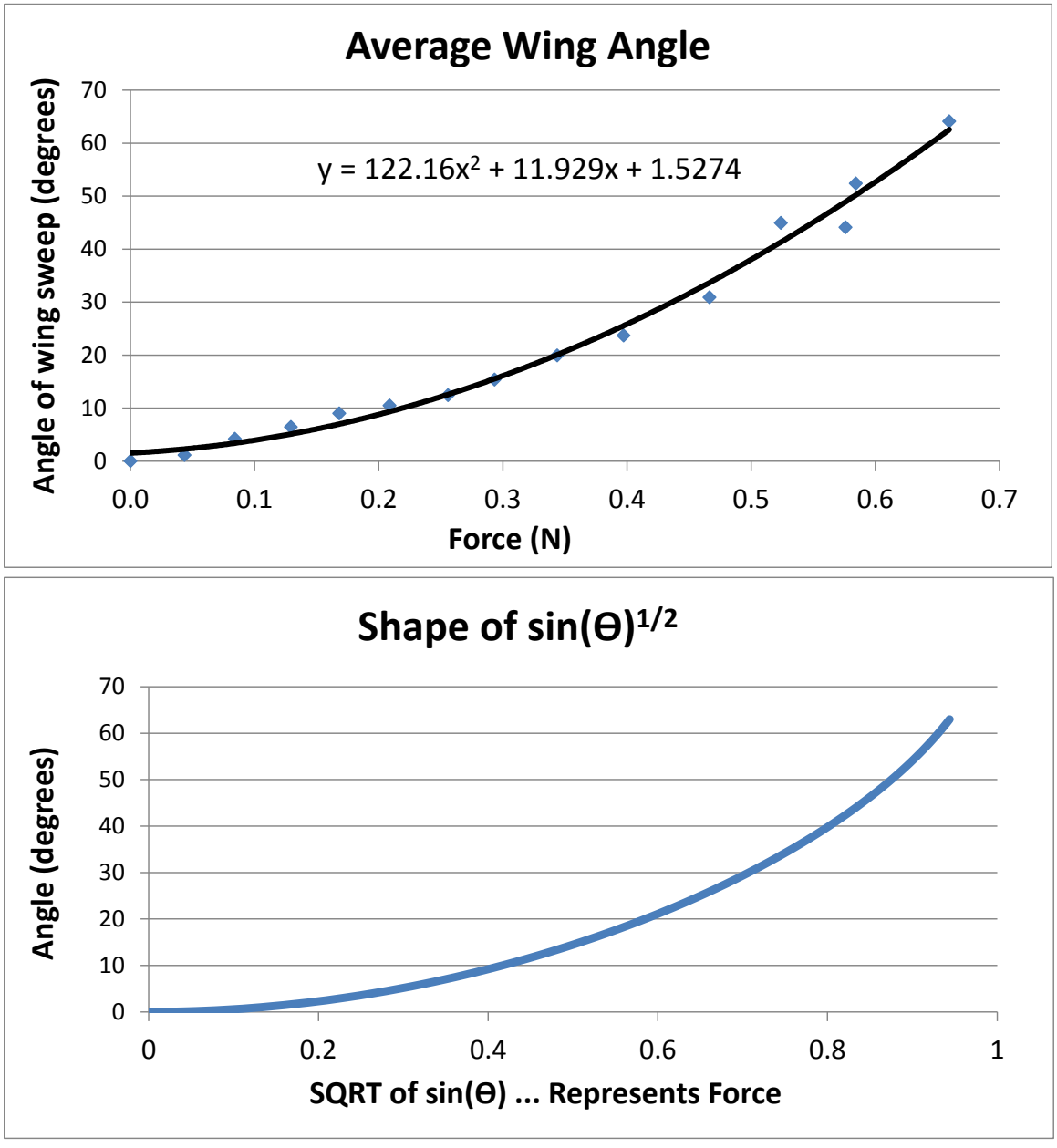

Figure 84 - Results (above) compared with a plot of Eqn. 58 with C2 set equal to 1. The shape is very similar, demonstrating that the 2nd-order fit is an appropriate approximation of the real wing angle response to DVM loading.

5.2. Results – Nanoindentation Experiment

Table 3 contains all of the results of the nanoindentation experiment and includes a description of each of the recorded criteria. Five specimens were examined.

Table 3 - Complete results from the nanoindentation experiment. The "*time run began*" row points out the passing of time before the initiation of the test after the preparation of the tergum. The "*# good samples*" row gives the actual number of samples used to determine the average modulus after the erroneous samples were removed. The "*depth range*" is the range from which the average modulus was calculated.

specimen #	**1**			**2**		**3**	
date of 1st run	5-Dec-11			7-Dec-11		9-Dec-11	
mass (g)	2.3			2.375		2.385	
time run began	fresh	27 hrs	60 hrs	fresh	24 hrs	fresh	12 hrs
# good samples	4	6	24	21	20	23	12
depth range (nm)	300-600	300-500	300-800	300-900	1000-1800	600-1800	500-1900
average E (Gpa)	**5.46**	**4.95**	**5.67**	**5.23**	**5.03**	**5.17**	**5.35**
notes	Depth not enough, increased from 500 in first two to 1000 for third.			Depth 1000 for first run, 2000 for second		Depth 2000 nm for the rest of the tests.	

specimen #	**4**		**5**					
date of 1st run	14-Dec-11		15-Dec-11					
mass (g)	2.2		1.85					
time run began	fresh	24 hrs	fresh	12 hrs	24 hrs	36 hrs	48 hrs	15 days!
# good samples	-	16	29	31	12	27	22	27
depth range (nm)	-	1000-2000	1000-2000	1000-2000	1000-2000	1000-2000	1000-2000	1000-2000
average E (Gpa)	-	**4.49**	**4.58**	**4.92**	**4.97**	**4.75**	**5.2**	**5.67**
notes	First run failed, second was good.		This shows that the tergum does not stiffen quickly due to dessication. After 15 days the modulus has only increased 16% over the average for the first two days.					

All of the tergum specimens were tested multiple times. In total, 10 test runs were performed on specimens within the first 24 hours after preparation (including the test on Moth 1 at 27 hours). A few more tests were run beyond this time frame to check for desiccation effects. The average elastic modulus ($\pm$ std. dev.) from all tests performed within approximately 24 hours was 5.02 ± 0.31 GPa (n=10). Moth 5 had a few tests

done between 24 and 48 hours; with these results included the average modulus was 5.01 ± 0.34 GPa (n=12). This value is lower than the first because Moth 5 had a relatively low modulus compared to the other specimens. The averages are summarized in Table 4. The final test of Moth 1 was performed after 60 hours, and the last run with Moth 5 was performed after 15 *days* to determine if any significant stiffening resulted from prolonged desiccation of the tergum. The resulting value of both of these tests was 5.67 GPa, which is about 13% greater than the average value from the first 24 and 48 hours of all tests. This minimal increase in stiffness over that extended period of time indicates that the tergum has a relatively low moisture content compared to softer, more pliable types of cuticle such as the joint articulation component of the beetle *Panchnoda marginata*, which stiffens by as much as 500% with desiccation (Barbakedze, et al. 2006). It is also possible that the method of preparation helped to seal in moisture. The outermost, waxy protective layer on the cuticle was not removed and the Crystalbond created a solid seal against the inner surface of the tergum.

Table 4 - Summary of elastic modulus values of the tergum found by nanoindentation

Timeframe	ave. E ± std dev	unit	# of Tests
average within 24 hrs	5.02 ± 0.31	GPa	N=10
average within 48 hrs	5.01 ± 0.34	GPa	N=12

The average modulus of elasticity of the *M.sexta* tergum, found in this experiment through nanoindentation, falls within the range reported for similar insect cuticle found by other means. Tensile and compression tests have been performed on cuticle parts of various insects and provide a range of elastic moduli from 1 GPa to 20 GPa for dry, tanned cuticle like the tergum (Vincent and Wegst 2004). This wide range is due to the

diverse applications of cuticle; many structural exoskeletal components tend to fall between 5 and 10 GPa (Dickinson 2012). The fact that the result from this experiment places the elastic modulus of the *M.sexta* tergal cuticle within the expected range indicates that nanoindentation is a viable option for determining the stiffness of insect cuticle. This experiment has shown that *M.sexta*'s tergum has a stiffness of approximately 5 GPa, providing a benchmark for comparison with manmade materials which might be used in a FWMAV fuselage with energy-storage capabilities.

5.3. Results – Dynamic Load Experiment

The dynamic load application experiment was used to determine the power output of the DVMs of 8 *M.sexta* specimens (Table 5). The average mechanical power ($\pm$ std.dev) required to elevate the wings through their natural range of motion was found to be 8.59 ± 2.20 mW for these 8 specimens.

Table 5 –Summary of power calculations. The calculated power is the absolute power required for the DVMs to fully elevate the wings at 25 Hz.

Specimen	Date	Mass (g)	disp. (mm)	time (ms)	Work (J) x10^{-4}	power (mW)
1	5-Dec-11	2.80	1.43	16	1.09	6.8
2	9-Dec-11	2.23	1.35	14.4	1.12	7.8
3	12-Dec-11	1.58	1.00	13.2	1.27	9.6
4	13-Dec-11	2.28	1.04	12.8	1.31	10.2
5	13-Dec-11	2.01	1.33	12	0.82	6.8
6	13-Dec-11	1.72	1.30	12.4	0.81	6.5
7	14-Dec-11	1.85	0.71	10.8	0.87	8.1
8	11-Feb-12	1.64	1.20	13.6	1.75	12.9
Averages		2.01	1.17	13.15	1.13	**8.59**
std. dev.		0.41	0.24	1.58	0.32	2.20

The mechanical power obtained in this experiment is an absolute value and must be divided by either the mass of the body or the mass of the muscle in order to be compared to accepted data from the literature in the form of power density. The term *power density* is used here despite the units of power/mass (instead of power/volume). The term *specific power* is better suited to this unit, but the present research was carried out using *power density* in order to conform to the literature.

Obtaining the actual DVM mass of each specimen would involve dissection skills that were outside the scope of this project. The standard ratio of *M.sexta* flight muscles to body mass is 20% (Stevenson and Josephson 1990), (Casey 1981). Dissections of *M.sexta* specimens revealed that the DLMs are significantly larger than the DVMs, an observation confirmed by a leading *M.sexta* expert (Willis 2012). The relative mass of the DVMs and DLMs was not available in the literature, so an equation for DVM power density ρ_{dvm} was developed based on a wide range of ratios:

$$\boldsymbol{\rho_{dvm} = \frac{P}{\alpha\beta m_b}} \qquad (59)$$

where α is the ratio of flight muscle mass to body mass and β is the ratio of DVM mass to flight muscle mass. P is the average absolute power derived experimentally and m_b is the average body mass of the specimens. This equation was plotted for a wide range of β with α set to 20% (Figure 85). The author's estimation is that the true value of β is between 15% and 30%, which cover a range of 72 W*kg^{-1} to 143 W*kg^{-1}. These values are in accordance with accepted measured and calculated *M.sexta* mechanical power output.

Table 6 contains the compilation of *M.sexta* power density values that were reported in Chapter 2 with the addition of the results of the present study. This experiment arrived at a power density which aligns with the bulk of the accepted data. The most reliable numbers in that table have been indicated in bold font. These values were obtained either directly from the muscle, or, as in this case, directly from the entire thorax/wing system. The other values may not be quite as reliable since they were obtained indirectly with computational or numerical models and equations which require numerous assumptions and simplifications. Casey's prediction in particular can be singled out as incorrect. He assumed a muscular efficiency of 20% and calculated the power output density based on measured power input (Casey 1976). That efficiency percentage was an accepted value at the time but has since been demonstrated to be much too high by modern estimations of insect muscular efficiencty . A range of accepted efficiency values is now between 5% and 10%, which would reduce Casey's predictions (for power density per muscle mass) to 102 $W*kg^{-1}$ and 135 $W*kg^{-1}$ which fits with the remainder of the estimations.

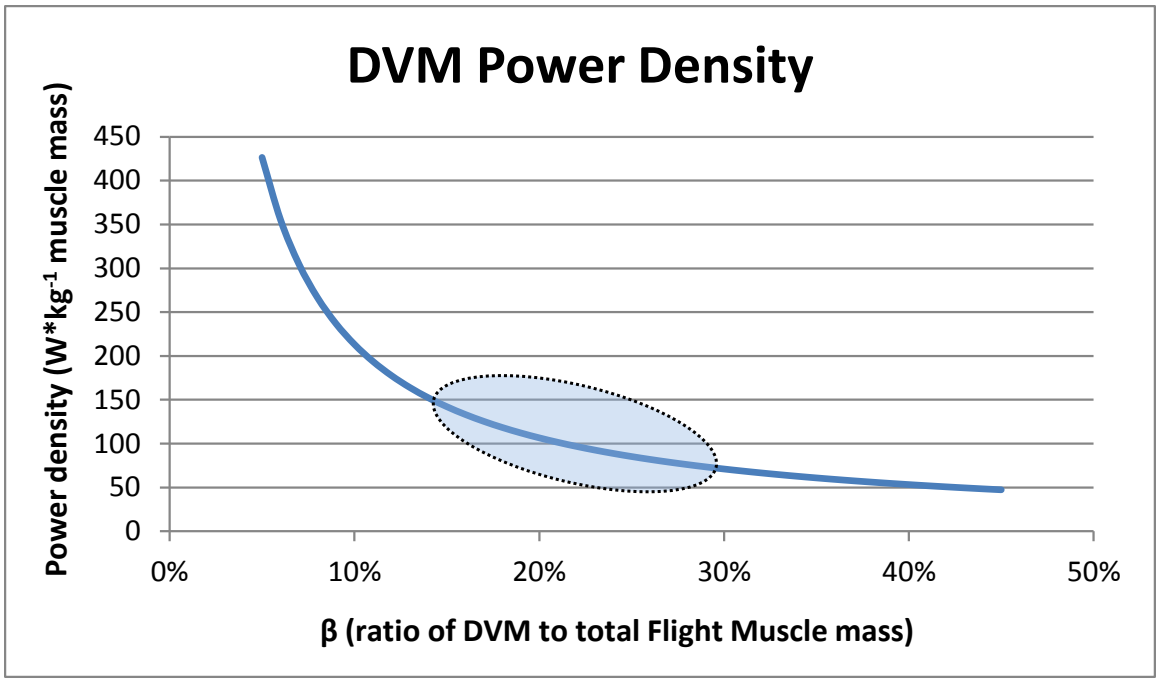

Figure 85 - This plot of Eqn. 59 shows the range of possible power densities for the DVMs assuming that flight muscle mass is 20% of the total body mass. The ratio of DVMs to flight muscle mass is represented by the horizontal axis. The author estimates that the DVMs comprise 15% to 30% of the flight muscle mass. That region is circled.

Table 6 - Compilation of *M.sexta* power densities including this author's contribution

***M.sexta* Power Output**		**power density ($W*kg^{-1}$)**		
researcher/year	**method**	**body mass**	**muscle mass**	**notes**
Casey 1976	estimation from power input	41-54	*205-270	Based on measurements of power input and estimate of 20% efficiency. We now know that actual efficiency is much lower
Pennycuick, Rezende 1983	muscle study	-	**82-97**	Estimated power density of muscle based on a known value for power density of mitochondria
Stevenson, Joesephson 1990	work-loop	-	**90**	Mean maximum power. Absolue max reached 130 in two specimens. 50-80 determined to be min. power req'd for flight
Sun, Du 2003	numerical	33-39	*164-194	With elastic storage - without elastic storage
Tu, Daniel 2004	work-loop	-	**83.3**	Specifically studied the DLMs
Liu, Aono 2009	computational	39.5	*197.5	Diff. species of hawkmoth, *Agrius convolvuli*
Zhao, Deng 2009	kinematics and aerodynamics	19.7 (aero) 16.4 (inertial)	*98-180	With elastic storage (no inertial power) - Without elastic storage (must overcome all power requirements)
Hollenbeck 2012	mechanical	-	†**72-143**	Direct measurement of mechanical power

*indicates equivalent value based on 20% muscle mass

†estimated range based on DVM/flight muscle ratio of 15% - 30%

***M.sexta* Power Input**		**power density ($W*kg^{-1}$)**		
researcher/year	**method**	**body mass**	**muscle mass**	**notes**
Casey 1976 (Reporting Heinrich 1971)	metabolic	191-289	478-722	Moth flies in closed jar and depletion of oxygen is measured/correlated to energy by assuming fat utilization during flight
Casey 1976	metabolic	237	694	Based on oxygen consumption
Stevenson, Joesephson 1990	metabolic	-	**1170**	Derived from Heinrich's 0_2 consumption. Most reliable number based on newer data

6. CONCLUSIONS

This research has furthered the understanding of a biological organism, the hawkmoth *M.sexta*, from a mechanical perspective as it relates to manmade FWMAV development efforts. Each of the three distinct sub-projects produced valuable results and, most importantly, paved the way for future explorations into the engineering applications of insect mechanics. This chapter summarizes the conclusions drawn from the results of each experiment and provides recommendations for technological and experimental improvement.

6.1. Static Load Experiment

The static load experiment characterized the mechanical properties of the *M.sexta* thorax/wing mechanism. The linear spring constant k which governs the force-compression relationship of this system was found to be 0.62 $N*mm^{-1}$. This spring constant will serve as a benchmark for FE models of the hawkmoth thorax. In addition, the wing elevation angle was related to thoracic compressive force (simulating DVM action). The observed relationship exhibited the theoretically predicted trend, indicating that the linear spring constant result, obtained with the same data set, it also trustworthy.

6.1.1. Recommendations

The basic setup for the static load experiment can be applied to nearly any current or future FWMAV design. It would be interesting to compare the spring constant of manmade vehicles with that of *M.sexta*. Of course, this experiment could easily be reworked for use on other insects such as dragonflies, bees, or flies. One conceivable research project might be to apply this experiment to several species of insects with the

objective of characterizing the spring constant *k* of natural FWMAVs. It may turn out that this constant varies with size, flapping frequency, wing type or muscle mass as do many other parameters common to both insects and FWMAVs. An improved understanding of size effects on insect flight mechanisms will correlate to increasingly precise manmade designs.

6.2. Nanoindentation Experiment

The tergum of the hawkmoth was shown to have an elastic modulus of just over 5 GPa. This value appeared to be consistent throughout the entire 2 μm depth of the indentation test with the exception of readings taken within a few hundred nanometers of the surface. Desiccation appeared to have little effect on the stiffness of the tergum, which indicated that this plate of the exoskeleton likely has a low moisture content *in vivo*.

6.2.1. Recommendations

The constant stiffness measurement (CSM) nanoindentation technique appeared to work satisfactorily for this application. The only cause for concern was the erratic behavior of the data near the point of surface contact (through the first few hundred nm). Careful analysis of the surface detection and indentation rate settings might reveal the reason for the errant readings and improve the quality of the experimental results. At the very least, it may be possible to alter the test settings to minimize the high rate of failure. However, it must be acknowledged that the roughness and impurity of the tergum, like any biological material, almost certainly precludes a 100% success rate.

It is possible that some of the approaches taken in this experiment could be improved upon in future biological nanoindentation efforts. Admittedly, specimen

preparation is one area where the author might have benefitted from a few extra biology lessons. Most of the biological nanoindentation sources presented in this thesis contain helpful information on the various procedures for preservation, rehydration, and mounting. It would be wise for any researcher pursuing this area of study to spend time familiarizing themselves with this material before beginning experiments.

In this experiment the tergum was excised from the specimen and mounted with Crystalbond. The author had theorized that mounting the entire thorax would not have been a viable option; however, Enders et al. suggest otherwise (Enders, et al. 2004). They examined a portion of the head-to-thorax articulation system of a beetle *Parachnoda marginata* by mounting the intact head to the sample holder. This indicates that it might be possible to streamline the indentation process for future experiments by simply mounting the entire thorax to the sample puck. It would be interesting to test a specimen with the thorax intact and run another test immediately afterwards on the tergum only. It is very likely that the results would be nearly identical. If they are not, then the next logical step would be to determine why the disparity exists and which method is more accurate.

The orientation of the specimen is another subject of interest. The elastic modulus found by indenting the surface of a multilayered composite structure (like the cuticle) is influenced by the entire thickness of that structure (Barbakedze, et al. 2006). Therefore, the value of 5 GPa for the tergum's modulus obtained in this experiment can be said to characterize the entire tergum. This should be the only value of interest to engineers, who only need to understand the tergum as a component of the thorax/wing mechanism. The elastic modulus of the entire thickness of the tergum defines its energy-storage capability

in bending. FWMAV designers can use the dimensions and properties of exoskeletal components like the tergum to search for manmade alternatives with similar qualities. If, however, it is determined that the various elastic moduli of the individual layers of the cuticle are of interest, precedents exist which can be followed. Sun et al. examined the cuticle layers of the elytra (wing covering) of the dung beetle *Copris ochus* by nanoindenting a cross-section of that component (Sun, Tong and Zhou 2006).

6.3. Dynamic Load Experiment

The dynamic load experiment measured the absolute power required to reproduce the full wing elevation portion of hovering flight in *M.sexta*. This value was related to the power density of the dorsoventral muscles (DVMs) by Eqn. 59, repeated here with all known values combined into a constant:

$$\boldsymbol{P_{dvm} = \frac{P}{\alpha \beta m_b}} \tag{60}$$

$$\boldsymbol{P_{dvm} = \frac{8.59}{(0.20)\beta(2.01)}} \tag{61}$$

$$\boldsymbol{P_{dvm} = \frac{21.37}{\beta}} \tag{62}$$

The most encouraging outcome of this experiment is the agreement between its result and the set of previously measured and calculated values for the mechanical power output of *M.sexta*. This indicates the accuracy of the method and essentially signals that this approach is viable for further development and future applications.

6.3.1. Evidence for Elastic Storage of Inertial Energy

The high-speed videos of this experiment's induced flapping clearly show at least some storage of inertial energy. Each flap requires the wings to return to the starting point in $1/50^{th}$ of a second with no externally applied force. That is, as the shaker retreats from its maximum vertical position, the vertically compressive (DVM) force on the thorax is being removed but there is no horizontally compressive force which kicks in to depress the wings (as the DLMs would in actual flight). Still, under the power of stored energy, the wings manage to return to, or nearly to, the initial position in time for the next vertical compression. There is one caveat, which is the fact that the entire specimen is moving up and down with the shaker. There will be some inertia transferred to the specimen as the shaker stops retreating and begins rising from its lowest position. This change in direction may be aiding the return of the wings, especially considering that there are a few milliseconds of disconnect between the tergum and the push rod during which the wings can continue to depress before contact is made. Redesigning the device so that the specimen is stationary and the push rod/load cell assembly moves with the shaker would resolve this problem.

However, a cursory review of the literature has turned up evidence for relatively significant movement of the moth's center of mass while hovering. More research in this area will be required before a conclusion can be reached, but it appears that the device used in this experiment moved the specimen's center of mass *less* than it would move in normal conditions. Daniel and Hedrick report a variation of ± 2.9 mm in hover during feeding (Daniel and Hedrick 2006), while the typical displacement induced in the present research was ± 1 mm. The value of ± 2.9 mm seems large and movements of that

magnitude are not evident in high-speed footage of live *M.sexta* specimens in flight. Therefore it is currently unclear whether the device developed for the present research moves the center of mass *too much* or *too little*, a question which must be answered before any conclusive statements are made about inertial energy storage.

6.3.2. Evidence for Passive Wing Twist

Wing twist is an important part of hovering flight in insects. How this wing twist is controlled is of interest to biologists and aerodynamic engineers alike. One of the major points of debate is the extent of muscle control versus passive control. In the past, the challenge of reproducing realistic flapping flight at 25 Hz with all boundary conditions intact *and without any muscle control from the living specimen* was impossible to overcome. This project is the first to offer a solution. No muscles were active during the flapping produced by the dynamic experiment (the specimens were euthanized). All boundary conditions were about as close as possible to *in vivo* conditions (some exceptions: muscle temperature and full range of motion downstroke). Wing twist was clearly observed in all of the high-speed videos, indicating that most, if not all of the wing twist is passively controlled by aerodynamic and inertial forces.

6.3.3. Actuators

One type of actuator, piezoelectric, is currently capable of producing high enough power densities to meet the demand of hawkmoth-like flapping flight. Harvard's Microrobotic Fly uses piezoelectric actuators which produce up to 400 $W*kg^{-1}$ (Wood 2008). However, their FWMAV needs to be wired to a power source and is therefore not capable of true free flight. The challenge, then, is to find a power source with high enough *energy* density to power the actuators in free flight. Small lithium batteries can produce 450

$W*kg^{-1}$ while weighing in at only 0.81 g (Steltz, et al. 2006). However, their charge lasts for 10 minutes or less. Finding or developing a power source light enough to carry in flight but energetically dense enough to sustain prolonged flight is the most imposing design challenge faced by engineers in the FWMAV field. The power source technology simply has not caught up to the rest of micromachinery advancements in recent years.

A few other options for actuation exist, though the problem of powering these actuators remains the same. Bao et al. describe an electromagnetic actuator at the micro scale capable of producing 40 $W*kg^{-1}$, which may be within range of the requirement of *M.sexta* (Bao, et al. 2011). Other options include comb drive, parallel plate, thermal biomaterial cantilever, and thermal expansion. Karpelson et al. provide an excellent review of these technologies as they relate to FWMAVs (Karpelson, Wei and Wood 2008).

6.3.4. Recommendations

This study has broadened the scope of the mechanical evaluation of flying insects for engineering applications. The device can be upgraded for numerous experiments and can even be applied as-is to certain areas of study which will provide numerous follow-on project opportunities.

6.3.4.1. Improvements to Current Experiment

Increasing the sample rate and using a more sensitive load cell would improve the results of the dynamic load experiment. The apparatus seemed to have difficulty sensing the precise moment of contact with the tergum. This meant that the author had to step through the video images frame-by-frame to manually determine that point. Higher precision, the result of an increased sample rate and a more sensitive load cell, would

enable automation of this process: the code would look for the upward turning point of the load within a pre-defined range of data and use that point for *P1*. Automatic determination of *P2* was already possible with the current setup and future studies could use this capability. The displacement tracking and processing code can be modified to find the peak displacement within a pre-defined range and label that point *P2*.

This experiment can also be improved with an upgraded mount and push rod system. It would often take five or six attempts to get a specimen precisely aligned with the push rod and keep it from sliding out of place during the run. A new mount with a more anatomically correct fit of specimen's body would streamline the test setup and reduce the frequency of failed runs. The push rod can be improved by designing the end to anatomically fit the average *M.sexta* tergum. An exact mimicry of the DVM load application cannot be created with a fully-rigid push rod. One way to overcome this challenge might be a spring-loaded set of small, angled arms at the end of the push rod which direct the force through the thorax at the angle of the DVMs. The angle would change with increased load and displacement just like the relative angle of the DVMs and the inner surface of the tergum changes during compression. This would be a complicated endeavor but might be the only way to truly simulate the realistic application of DVM force.

6.3.4.2. Adapting for Future Experimentation

The dynamic load experiment only reproduced the vertical compression caused by the DVMs and the subsequent wing elevation. The DLMs and their invoked downstroke of the wings were not examined. It would be a significant improvement to alter this device to replicate the complete flapping motion of *M.sexta*. There are at least two ways this can

be undertaken. The first is to incorporate two of everything; two shakers, two load cells and two cameras. The original setup would be unchanged except for the addition of a horizontal shaker for the DLM compression and a second camera set up perpendicular to the original to record the horizontal compression of the thorax during the downstroke. The second option is to devise a linkage system which induces both the vertical and horizontal compression of both muscle groups using the original vertical shaker setup. The author has designed a prototype linkage and mount system of this nature which is currently under development at AFIT. Appendix H contains a detailed explanation of this design.

6.3.4.3. Wings: Aeroelasticity and Inertial Effects

Modeling the dynamic movement of insect wings during flight presents unique challenges. Delineating the relative significance of fluid dynamic forces and inertial effects on wing bending can simplify the process, especially if it turns out that the motion can be modeled without considering aerodynamics. One such study attempts to do just that.

Using freshly excised wings clamped to a motor, Combes and Daniel examined the patterns of *M.sexta* wing deformation in air and helium (15% of air density) to determine the extent of aeroelasticity, fluid-damping, and inertial-elastic forces on wing bending (Combes and Daniel 2003). They determined that the aeroelastic effects are minimal and only inertia plays a significant role in bending. Their finite element models confirmed this theory. They concluded that a damped finite element model can accurately predict the pattern and magnitude of wing deformations during flight without considering

aerodynamic calculations, confirming their theory set forth the previous year (Daniel and Combes 2002).

Their conclusions, however, are not without objection from many in their field (Sims 2010). The jury is still out on the aeroelasticity problem, but the dynamic load device developed for the present study may be able to contribute to the solution. One of the biggest issues with the current methods is the lack of proper boundary conditions for the wing. All of the experiments involve removing the wing and clamping it to a motorized flapper. Completely realistic flapping, with all boundary conditions intact (with the exception of actual electro-chemical muscle contraction) will be possible with the modified, full-flapping version of the author's dynamic load device. It might be pointed out that it would be easier to observe a live specimen in flight, and indeed this has been done extensively. However, that same live specimen cannot be placed in a vacuum (or in pure helium for that matter) and expected to flap for very long. This device will enable full boundary condition flapping in a vacuum or other low-density, low-oxygen environments which can then be compared with flapping in air.

6.4. Summary of Conclusions

1. The thorax linearly compresses 1 mm under 0.62 N of force in the direction of the DVMs. Therefore, the thorax has a linear spring constant of $k = 0.62\ \mathrm{N/mm}$.

2. The static displacement of the wing and thorax caused by contraction of the DVMs can be described by the following equation which relates force, compression and wing elevation angle:

$$P = k\left(\frac{m_{wing} g L \sin\theta}{k}\right)^{\frac{1}{2}} \quad (63)$$

3. Constant stiffness measurement (CSM) nanoindentation of the tergum was successfully carried out and resulted in a modulus of elasticity of approximately 5 GPa for the *M.sexta* tergum.

4. The thickness of the tergum was examined as part of the nanoindentation experimental setup. This major component of the exoskeleton is a consistent 28-30 μm thick throughout the cross-section.

5. The power density ρ_{dvm} of *M.sexta*'s dorsoventral flight muscles (DVMs) is given by the following equation:

$$\rho_{dvm} = \frac{P}{\alpha\beta m_b} \quad (64)$$

where α is the ratio of flight muscle mass to body mass (assumed to be 20%) and β is the ratio of DVM mass to flight muscle mass. P is 8.59 mW, the average absolute power derived in the experiment. The average body mass of the specimens, 2.01 g, is represented by m_b. A range of 15% to 30% was used for β when calculating the DVM power density.

6. The dynamic load experiment is the first of its kind and has measured a power density of 72-143 $W*kg^{-1}$ for the DVMs. This range can be narrowed down if the ratio β of DVM to total flight muscle mass becomes available.

7. The dynamic load experiment can be redesigned to induce the full natural range of motion in euthanized *M.sexta* specimens.

8. The device developed for the dynamic load experiment, and its future iterations, will enable ultra-low viscosity flapping (in vacuum or helium, for example) with fully intact boundary conditions, which will contribute significantly toward solving the problem of viscous versus inertial effects on wing bending.

9. The dynamic experiment revealed evidence for inertial energy storage. A redesign of the device which fixes the specimen in place and actuates the push rod/load cell may fully decide the case.

10. Similarly, the dynamic experiment has provided excellent evidence for passive wing twist. Observation of the high-speed videos confirms that the wings twist significantly (and realistically) without any muscle control.

Appendix A. Raising Hawkmoths

The AFIT FWMAV research group receives hawkmoth pupae on a regular basis from Dr. Mark Willis at Case Western University. Dr. Willis' lab contains a thriving colony of *Manduca Sexta*, which produces scores of moths each week. The most challenging part of raising the hawkmoths, hatching the eggs and feeding the caterpillars, is already complete when we receive the pupae in the mail (refer to (Reinecke, Buckner and Grugel 1980) for an excellent exposition on the full life cycle). All they need are a proper light cycle and the right temperature in order to eclose (hatch into adulthood). Figure 86 shows a hawkmoth pupa. The specimen is on its back with the head pointed toward the left. The right forewing can be seen wrapped around midsection of the body. The abdomen with its many segments and spiracles, points to the right. The "handle" object protruding from the head is the proboscis, folded several times. When extended, the proboscis of the adult *M.sexta* can be as long as it's body, and is used for feeding on flower nectar while hovering.

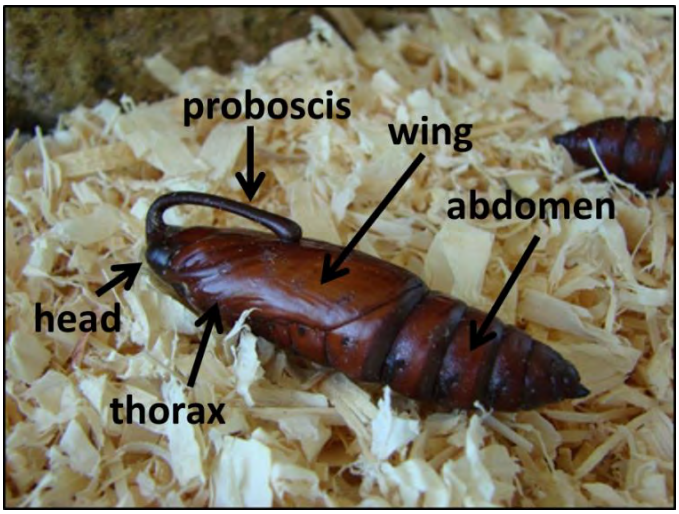

Figure 86 - Typical *M.sexta* pupa. The wins are small and wrapped around the thorax and upper abdomen. In the wild, these pupa use the segmented abdomen to burrow under soil or leaves for protection from the elements until it is time to eclose.

A.1. The Enclosure

A 1x1x1 foot cubic terrarium holds the pupae prior to eclosion. The bottom of the terrarium is lined with approximately 1 inch of wood shavings beneath a layer of paper towels. This, along with frequent cleaning, is necessary because with each moth's eclosion comes a release of large quantities of waste (*meconium*) which is the by-product of the transformation from caterpillar to moth (Reinecke, Buckner and Grugel 1980). The front of the terrarium has doors which can swing open for access from the front and the entire top glass pane can be removed for access from the top. The most important feature is the back wall made of textured foam. This wall gives the freshly eclosed moth a surface to climb up, which is an absolute necessity. The moth must climb off of the ground in order to pump fluids through the veins in its wings to stretch them out before they harden. Typically, the moth finds a position on the wall in about 10 minutes and has fully inflated its wings 20 minutes later. Figure 87 shows two young adult hawkmoths which hatched only a few minutes apart.

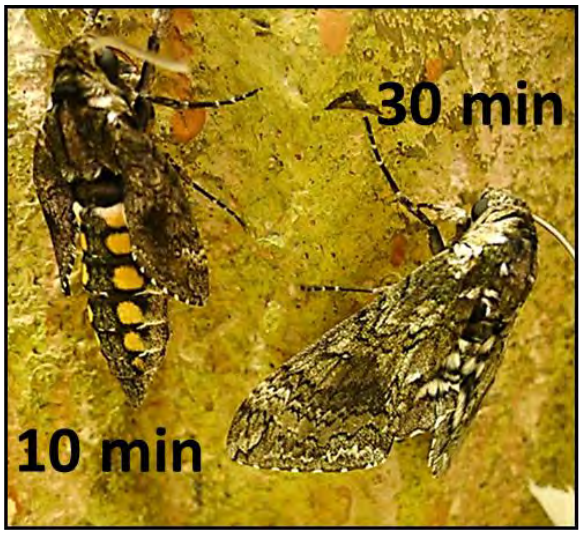

Figure 87 - Two freshly-eclosed *M.sexta* specimens. One is only 10 minutes old and has not inflated its wings.

A.2. Light Cycle and Environment

M.sexta thrives in the warm temperatures of the southern North American summer. The pupae prefer a summertime light cycle of long days and short nights, as well as warm summertime temperatures. The light cycle for the AFIT moths has been set to 14 hours of light and 10 hours of darkness (Willis 2011). The light cycle is accomplished using a standard outlet timer wired to a string of LED lights secured around the inner walls of a cardboard box (Figure 88). The terrarium with the pupae is placed within this box and the lid is then closed, allowing no light from the outside. The temperature of the vivarium is set to 80 degrees Fahrenheit and the humidity is kept at 40 percent in order to replicate summertime conditions.

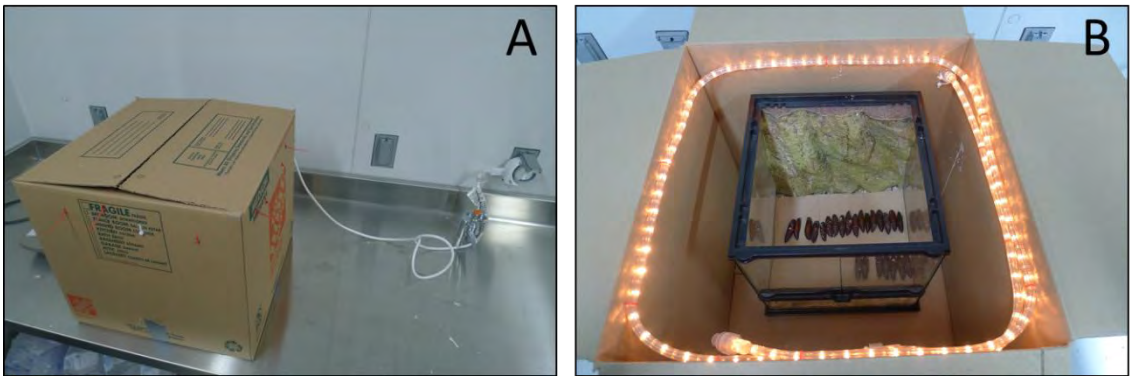

Figure 88 - Enclosure for the pupae: **(A)** Closed box creates day/night conditions with a timer controlling the LED lights, shown in part **(B)**

A.3. Eclosion

The terrarium is checked daily for newly emerged adult moths. They tend to eclose at "dusk," or shortly after their light cycle switches from light to dark. Since the cardboard box enclosure around the terrarium allows this light cycle to be set for any time of day, the light-to-dark transition has been set to occur mid-afternoon. That way, the moths will eclose in the afternoon and the terrarium can be checked for adults when heading home

for the day. When an adult moth is found in the pupa terrarium during daily inspections, it is transferred to a mesh cage which is constantly open to the light of the vivarium (Figure 89). *M.sexta* is a nocturnal species, and as such is inactive during daylight. The adults are therefore docile and essentially dormant as long as the lights are kept on. If the lights are switched off, however, the adults will fly for hours against the walls of the enclosure and damage their wings. This is to be avoided because much of the research that goes on among the AFIT FWMAV research group requires intact forewings.

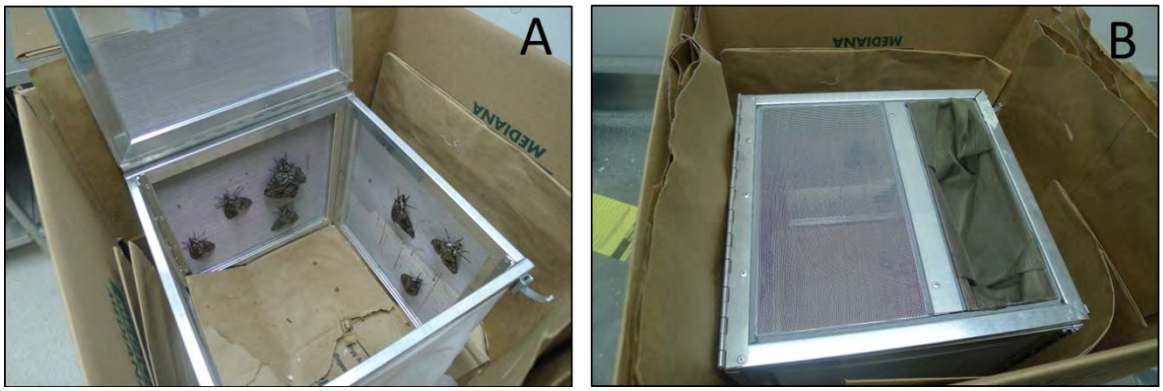

Figure 89 - Adult enclosure: (C) Moths sit dormant on the mesh wall, (B) Lid closed, light can pass through. The cage sits inside a cardboard box lined with paper bags to facilitate cleaning. Adults often emit meconium hours or even days after eclosion.

A.4. Preparation for Experimentation

When an adult *M.sexta* is required for an experiment it is removed from the vivarium and placed in a jar. If the integrity of the wings is of utmost importance, the jar is then placed in a refrigerator and left for at least 30 minutes. The cold air immobilizes the moth but will not cause tissue damage. Immobilizing the moth with refrigeration helps prevent excessive flapping inside the jar which could damage the wings. The jar is then removed from the refrigerator. Paper towels soaked with nail polish remover are then added to the jar. The acetone vapor asphyxiates the moth within 1 hour. An alternative option is to

place the specimen in a freezer for more than 45 minutes. This is long enough to kill the specimen without crystallizing most of the liquid in the muscles. This method was only used for dissection specimens, as it was deemed too harsh on the material properties of the cuticle and muscles for the purposes of the experiments.

A.5. Removal of Scales

Scales cover nearly the entire body of the adult moth. The wings and abdomen are covered with a thin layer of scales that tends to stay on the moth unless purposefully brushed away. The scales on the thorax, however, are very densely packed and easily become airborne when a specimen is handled. It is therefore necessary to remove the scales from the thorax before beginning experimentation. The scales can be brushed off under running water either with a toothbrush or by hand. Moving water carries the scales away and prevents them from becoming airborne, which could be an eye irritant.

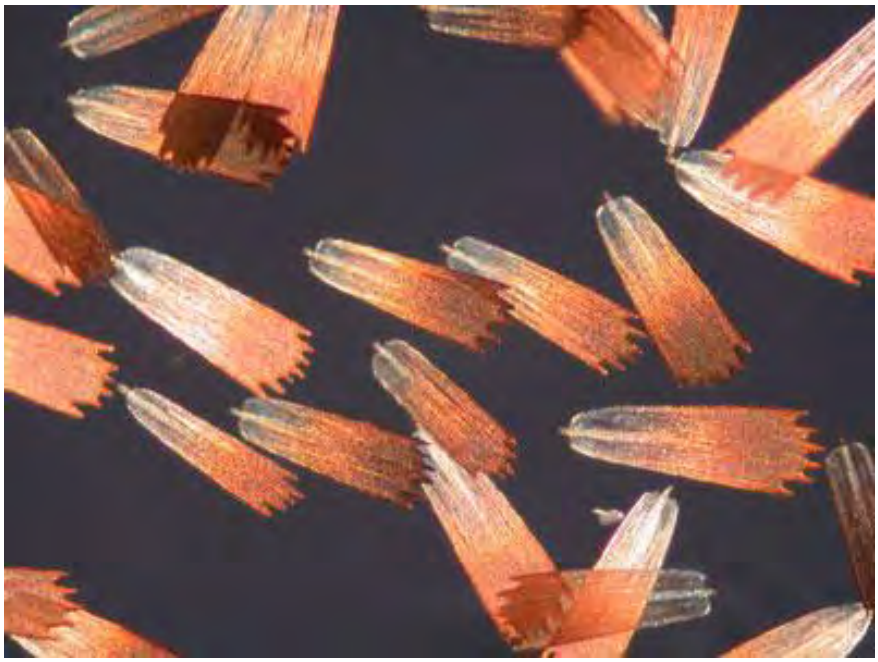

Figure 90 – 200x Magnified image of moth scales (Jenikova 2005)

Appendix B. Matlab Code for Static Experiment Processing

```
clc,clear,close all

%% First, let's read all the data-sets from the dam0.unv file
[FileName,PathName] = uigetfile('*.jpg*','0');
File = FileName(1:findstr(FileName,'.')-1);
Ext = FileName((findstr(FileName,'.')+1):length(FileName));

%% Read in Moth image
I = imread([PathName FileName]);

%% Plot the picture in a figure
imshow(I);

%% Pick 5 Points on the image
%  location is in pixels
[x,y]=ginput(5)
%% Convert Pixels to millimeters
Pix2mm =40;
mm = [x,y] / Pix2mm

%% Save .mat file with image filename
save([File '.mat'])

%% Calculate wing angles and vertical distance from ruler
Theta_Right=abs(atand((y(2)-y(1))/(x(2)-x(1))))
Theta_Left=abs(atand((y(3)-y(1))/(x(3)-x(1))))
disp=abs(mm(4,2)-mm(5,2))
```

Appendix C. Signal and Load Code for Dynamic Experiment

```
clc,clear,close all
%% Set the Sampling Options
SampleSeconds = 1; % Time in Seconds
SampleRate    = 2500; % Hz
SampleNumber = SampleRate * SampleSeconds; % Total Samples
SampleTime = linspace(0,SampleSeconds,SampleNumber); %Time Vector

%% Calculate the output signal based on the SampleNumber of the data
g = 1.9;   % Gain (amplitude of sine wave)
bias=0;  % Bias for the shaker sine wave signal (neg. bias for pos.
movement)
OmegaDeg = 25;                  % Frequency in Hz
OmegaRad = OmegaDeg*2*pi;       % Frequency in Radians

% Output 1 - Camera Trigger
data1 = 5 * ones(1,SampleNumber)';
data1(end)=0;
% Output 2 - Shaker Signal
data2=0*ones(1,SampleRate)';  % Establish a SampleRate:1 matrix to fill
t=200;  % Number of samples used to tare the load cell before shaker
starts
data2(1:t) = 0*ones(1,t);  % Signal is zero for duration of "t"
data2(t+1:SampleRate) =
sin(linspace(0,OmegaRad*SampleSeconds,SampleNumber-t))'; % Sinusoidal
signal
data2 = g * data2;     % Apply Amplitude (gain)
data2 = data2 + bias;  % Apply Bias to sine wave
data2(1:t) = 0*ones(1,t);  % after bias so tare will still be at zero
data2(end)=0;

%% Get NI USB-6251 Data
NI = daqhwinfo('nidaq');

%% Create Device object
ao = analogoutput('nidaq',NI.InstalledBoardIds{1});
ai = analoginput('nidaq',NI.InstalledBoardIds{1});

%% Set Channels
chans_ao = addchannel(ao,0:1); % Analog Out Channel 0 & 1
chans_ai = addchannel(ai,0); % Analog In  Channel 0

%% Set AO Sample Options
ao.SampleRate = SampleRate;

%% Set AI Sample Options
ai.SampleRate = SampleRate;
ai.TriggerRepeat = 0;
ai.SamplesPerTrigger = SampleNumber;

%% Obtain the actual rate set in case hardware limitations
ActualRate = get(ao,'SampleRate');
```

```
%% Set TriggerType to Manual for fastest triggering
set([ai ao],'TriggerType','Manual')

%% Queue the output on 2 channels
putdata(ao,[data1 data2]);

%% Start and Trigger the Output
start([ai ao]);   % Start Analog Output
trigger([ai ao]); % Start Analog Input

%% Capture Analog Input Data from the buffer
data_ai = getdata(ai);

%% Clean and Remove ai & ao from memory
delete(ai)
delete(ao)

%% Convert voltage signal to grams and grams to Newtons
tare=sum(data_ai(1:t)/t) % gets average voltage signal from tare period
slope = 0.0219; % grams/volt slope of the load cell as calibrated
force = -45.749*data_ai + tare/slope; % Determines equivalent mass in
grams
forceN = force/101.971; % Convert mass (grams) to Newtons

%% Make figures of force vs time
figure
plot (1:SampleRate,forceN)
title('Force vs. Time with tare')
xlabel('time (seconds * 1/2500)')
ylabel('force (N)')

%% Check sine wave signal, only necessary for setting up test runs
%figure
% plot(data2(t+1:SampleRate));
```

Appendix D. Video Proc. and Tracking for Dynamic Experiment

```
%% Modified to select triangle and square and log excessive shifts in x
and y
clc,clear all ,close all

%% Get .tif files
Files=dir('*.tif');
NumPoints=input('How many points are you tracking?\n');
NumFrames=input('How many frames are you using?\n');

l=1;
k=1;
n=2;
m=1;
while m<=NumFrames-1;

    I(1).I = imread(Files(m).name);
    I(2).I = imread(Files(m+1).name);
    for p=1:NumPoints
        if m == 1

            fprintf('Select point %d.\n',p);
            [I(1).Point(p).Sub,I(1).Point(p).SubRect] = imcrop(I(1).I);
% Choose the Subimage of square from I1
            [I(2).Point(p).Sub,I(2).Point(p).SubRect] =
imcrop(I(2).I,I(1).Point(p).SubRect);    % Choose the Subimage from I2
            if p==NumPoints
                fprintf('Go play pinball or minesweeper on the
nanoindenter computer.\n');
            end
        end
        if m>3
        checks =(abs(Point(p).x(m-1)-Point(p).x(m-2))>10);
            if checks == 1
            fprintf('Select the %d.\n',p);
            [I(1).Point(p).Sub,I(1).Point(p).SubRect] = imcrop(I(1).I);
% Choose the Subimage of square from I1
            [I(2).Point(p).Sub,I(2).Point(p).SubRect] =
imcrop(I(2).I,I(1).Point(p).SubRect);   % Choose the Subimage from I2
            fprintf('Go back to your coffee.\n');
            m=m-1;
            end
        end
    % Compute Normalized Xcorr2 Sub-Image 1 to Image 2
    c = normxcorr2(I(n-1).Point(p).Sub,I(n).I);
    %figure, surf(I(n).c(:,:,1)), shading flat
    [MaxC,Imax] = max(abs(c(:)));
    [y_peak, x_peak] = ind2sub(size(c),Imax);
    corr_offset_xs = x_peak-size(I(n-1).Point(p).Sub,2);
    corr_offset_ys = y_peak-size(I(n-1).Point(p).Sub,1);
    Point(p).x(m) = corr_offset_xs+I(n-1).Point(p).SubRect(3)/2;
    Point(p).y(m) = corr_offset_ys+I(n-1).Point(p).SubRect(4)/2;
```

```
    fprintf('Process Frame %d of %d\n',[m NumFrames-1])
    end
    m=m+1;
end

%% Make Avi of Tracking progress
% Create Video Object
vidObj = VideoWriter('Moth 14.avi');

% Set and view the frame rate.
vidObj.FrameRate = 30;

% Open Video Object
open(vidObj);
figure
for m=2:NumFrames-1
   imshow(imread(Files(m).name))
   hold on
   for p=1:NumPoints
   plot(Point(p).x(m),Point(p).y(m),'r+')
   end
   hold off
   currFrame = getframe;
   writeVideo(vidObj,currFrame);
end

% Close the file.
close(vidObj);

% make a plot of the shaker displacement versus time
conv=10.8 % pixels per mm

Disp = [1:998]'*0
Disp(:) = Point(1).y(:)
%% plot the vertical displacement
figure
%plot((1:NumFrames)/2500,atand(abs((Point(1).y(:)-
Point(3).y(:))/(Point(1).x(:)-Point(3).x(:)))),'r');
% ^^ can be used to calculate wing angles, just click where you would
for the static test
plot(1:NumFrames-1,(Disp(:)/-conv))
title('Vertical Displacement over first 1000 frames')
xlabel('frame # or time (sec/2500)')
ylabel('Vertical displacement (mm)')
```

Appendix E. Power Calculation Code for Dynamic Experiment

```
%% Before running this code, load the workspaces for the force and
tracking data

clear D
clear disp

p1 = 904 % enter the frame in which the force begins to increase
p2 = 944 % enter the frame in which the maximum displacement occurs

%% Create an array of displacement values over the desired range of
time
conv=10.8; % pixels per mm
Disp = [1:998]'*0;
Disp(:) = Point(1).y(:);
disp(1:p2-p1)=[1:p2-p1]'*0;
for i=2:p2-p1+1;
    disp(i) = disp(i-1) + (Disp(p2)-Disp(p1))/(p2-p1)/(-conv*1000);
end
D = disp'; % simplify name and invert the matrix

%% Plot the force over distance
F = forceN + abs (min(forceN(p1:p2))); % adjusts the force so the
smallest value is set to zero
figure
plot (D,F(p1:p2))
xlabel ('Distance (m)')
ylabel ('Force (N)')
title ('Force over Distance for a Single Upstroke')

%% present the total displacement in mm
displacement = (D(end)-D(1))*1000

%% Integrate over this region to get the work
Work = trapz (D,F(p1:p2)) % this is the total work or energy in Joules

%% Divide work by total time interval during application of the force
time=(p2-p1)/2500 % The time interval in seconds during which the force
is imparted
Power = Work / time % This is what we're after!!!
```

Appendix F. Processing Code for Nanoindentation Experiment

```
clc,clear,close all

%% Load Excel File
filename='T6t15days.xls'; % Tergum#test#.xlsx
[status,sheets] = xlsfinfo(filename);

n = length(sheets); % Number of Samples + 3
min = 733; % Low end of best excel data (750-850 gives 1000-2000 nm
range)
max = 845; % Highest number before end of data in excel file

for i=4:n
    [data, labels] = xlsread(filename,sheets{i});

    % Process the Excel File
    data     = data(:,:);
    Test(i).Depth    = data(min:max,1); % Specify range  and column
    Test(i).Modulus  = data(min:max,6);

    % Calculate the Mean Modulus for each test run
    Test(i).MeanModulus = nanmean(Test(i).Modulus);
end

%% Compute the average from all runs
sum = 0;
for i=4:n
    Test(i).MeanModulus
    sum = sum + Test(i).MeanModulus;
end
Average = sum/(n-3)

%% Plot the Modulus vs. Depth data
close all
for i=4:n
    x=Test(i).Depth;
    y=Test(i).Modulus;
    plot(x,y,'.-')
    hold on
    grid on
    xlabel('Depth into Surface (nm)')
    ylabel('Modulus of Elasticity (GPa)')
    title('All Tests')
    orient landscape
    %print(h,'-djpeg',['Test Number' num2str(i)]);
end
```

Appendix G. Complete Results of Static Experiment

G.1. First Iteration – Wing Angle vs. Force – No Load Cell

The static load experiment was the first investigation performed as part of this research project. The initial iteration produced only rough data correlating the DVM force with the subsequent wing elevation angle. As previously mentioned, the data is rough because the load cell was not yet in use. Five *M.sexta* specimens were examined in this round of testing, with the third moth undergoing two test runs. The force and wing angle data from this set of tests is given in Figure 91.

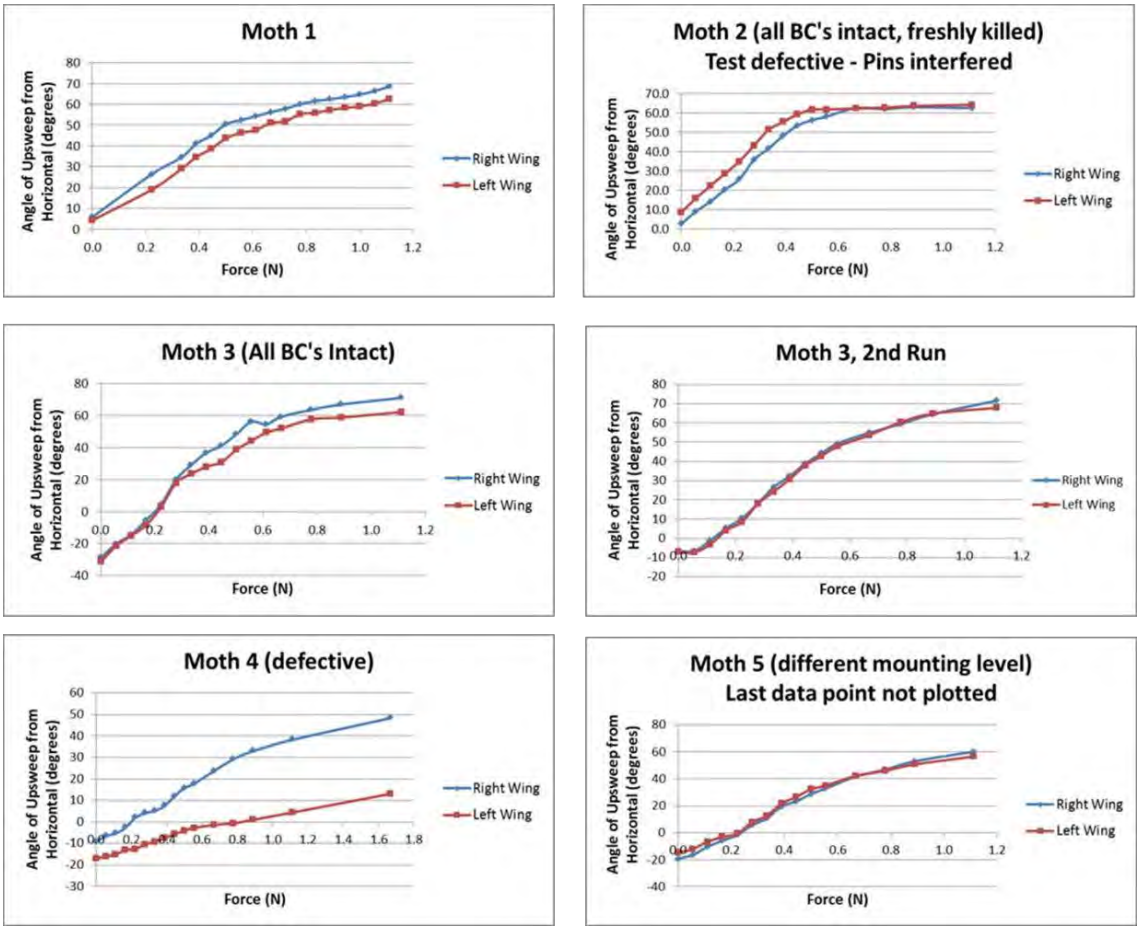

Figure 91 - All data from first round of static load tests. No load cell was used and the data is not reliable.

The results were then refined by adjusting each set of data so that the initial angle is zero, which produced a plot of absolute increase in angle for each run (Figure 92). It was obvious that a few of the data sets were erroneous. Moth 2 was eliminated because a close review of the photos revealed that the wings had come into contact with the pins supporting the specimen, which prevented them from surpassing 60 degrees in elevation. The first run of moth 3 was removed due to issues with the mounting angle of the specimen. The initial measurement of the wing angle was over 30 degrees below horizontal because the specimen was tilted too far forward. The positioning was corrected and the second run of moth 3 produced data in accordance with that of the other specimens. Moth 4 was the only specimen that was outright defective. No amount of force could induce a wing elevation beyond 40 degrees for the right wing and about 20 for the left wing. It was also noted that the tergum easily buckled under minimal pressure. It is likely that this specimen had not fully formed before eclosion. The final compilation of the three acceptable runs is shown in Figure 93.

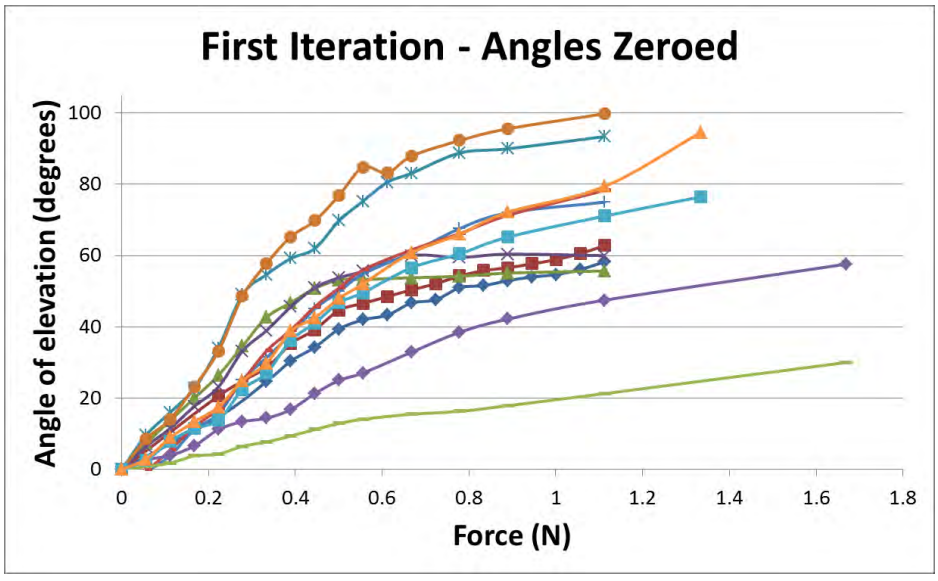

Figure 92 - Compilation of complete force-angle results of first iteration

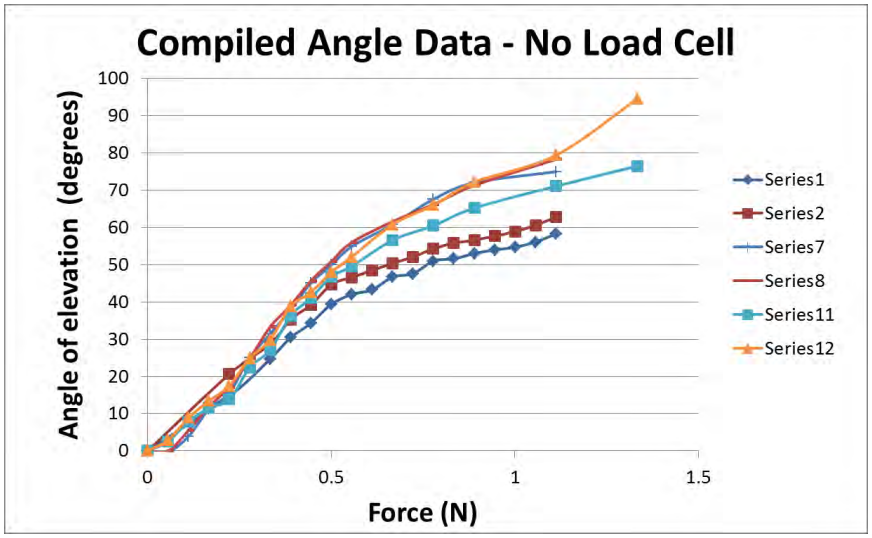

Figure 93 - Defective results removed

Finally, these results were averaged and plotted in order to observe the trend (Figure 94, Figure 95, and Figure 96).

	Moth 1		Moth 3		Moth 5					
# of Quarters	zeroed		zeroed		zeroed		Average Left	Average Right	**Average wing angle**	Force (N)
	left	right	left	right	left	right				
0	0.0	0.0	0.0	0.0	0.0	0.0	0.00	0.00	**0.00**	0.00
1			-0.3	0.0	2.5	2.9	1.10	1.45	**1.28**	0.06
2			3.9	5.5	7.9	8.9	5.90	7.20	**6.55**	0.11
3			11.2	11.9	11.5	13.4	11.35	12.65	**12.00**	0.17
4	14.7	20.6	15.6	17.1	13.8	17.5	14.70	18.40	**16.55**	0.22
5			25.1	24.8	22.4	24.9	23.75	24.85	**24.30**	0.28
6	24.7	28.7	31.4	33.3	27.1	29.8	27.73	30.60	**29.17**	0.33
7	30.4	35.3	37.9	39.1	36.2	38.8	34.83	37.73	**36.28**	0.39
8	34.3	39.2	45.1	45.7	41.1	42.6	40.17	42.50	**41.33**	0.44
9	39.4	44.7	49.9	50.9	46.8	48.0	45.37	47.87	**46.62**	0.50
10	42.0	46.6	54.9	56.0	49.6	52.1	48.83	51.57	**50.20**	0.56
12	46.7	50.4	60.8	61.6	56.6	60.8	54.70	57.60	**56.15**	0.67
14	51.0	54.3	67.6	66.2	60.5	66.0	59.70	62.17	**60.93**	0.78
16	53.0	56.6	72.0	71.3	65.2	72.2	63.40	66.70	**65.05**	0.89
20	58.3	62.8	75.0	78.3	71.1	79.4	68.13	73.50	**70.82**	1.11

Figure 94 - Array of data used for the production of the plot of average wing angle versus force

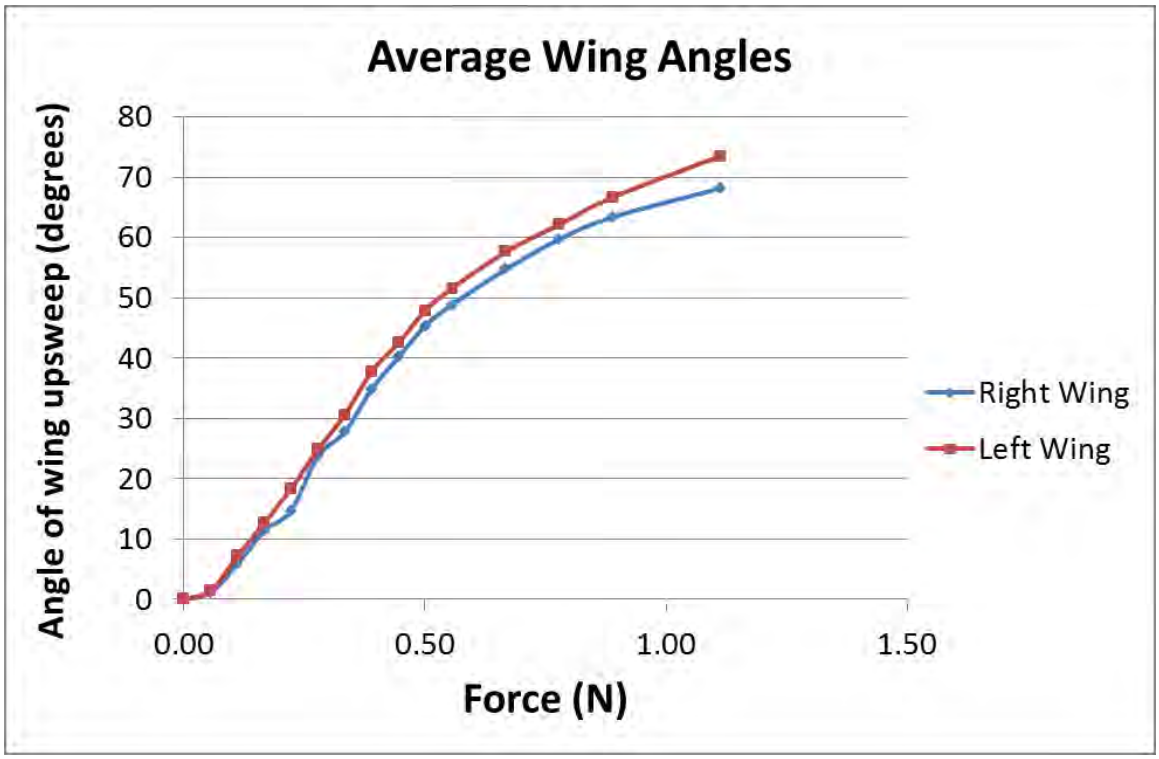

Figure 95 - Average wing angle for right and left wings for the first iteration

Figure 96 - Average wing angle versus applied force (first iteration of static load experiment)

G.2. Second Iteration – Compression and Wing Angle vs. Force with Load Cell

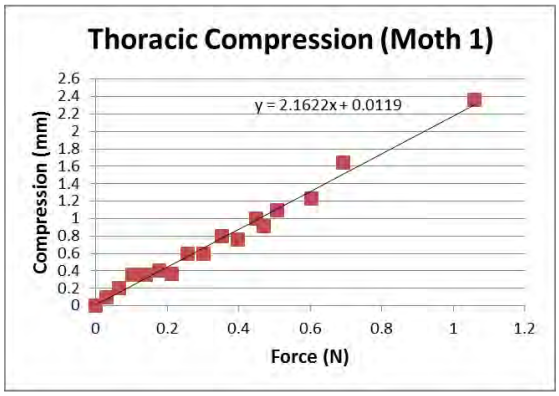

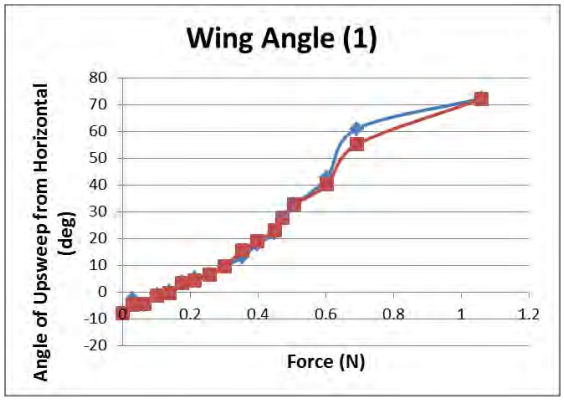

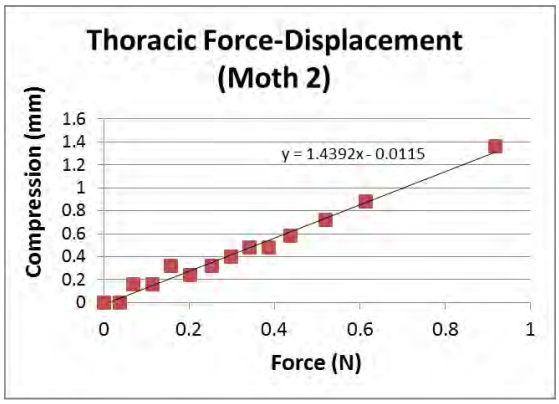

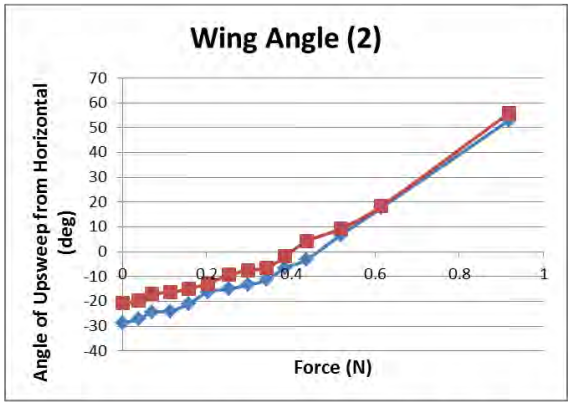

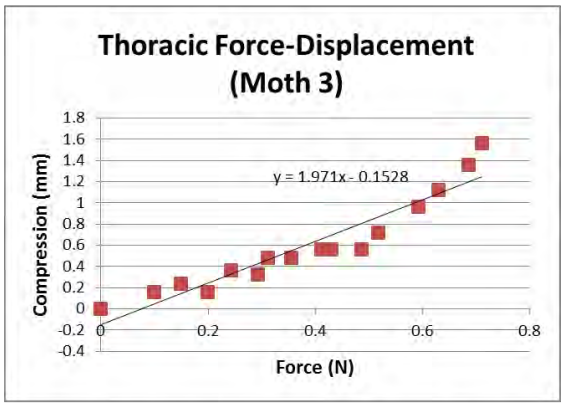

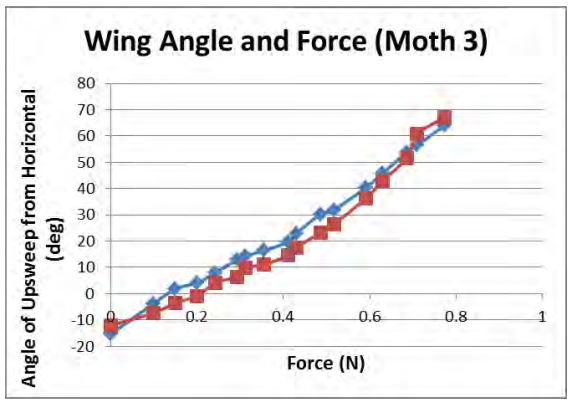

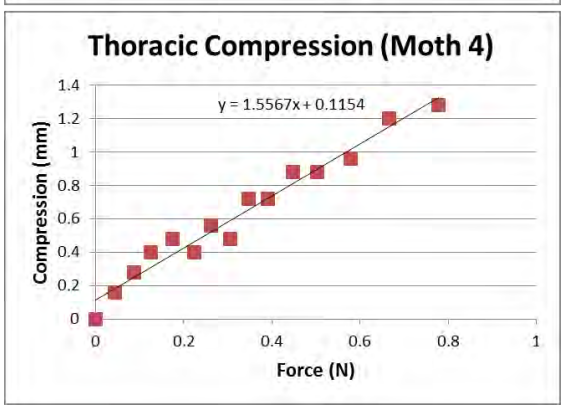

Appendix H. Modifying Dynamic Device for Full ROM Flapping

The author modified the original device to include horizontal force for longitudinal compression of the tergum. This new design will, with some minor adjustment to the geometry and sizing of the components, be able to induce complete range of motion (RoM) flapping. Figure 97 shows the original device compared with this concept. Only one camera and one shaker are required. The horizontal displacement can be calculated based on the four-bar linkage and correlated to the vertical displacement. This means that the horizontal movement will not have to be tracked and therefore will not have to be filmed.

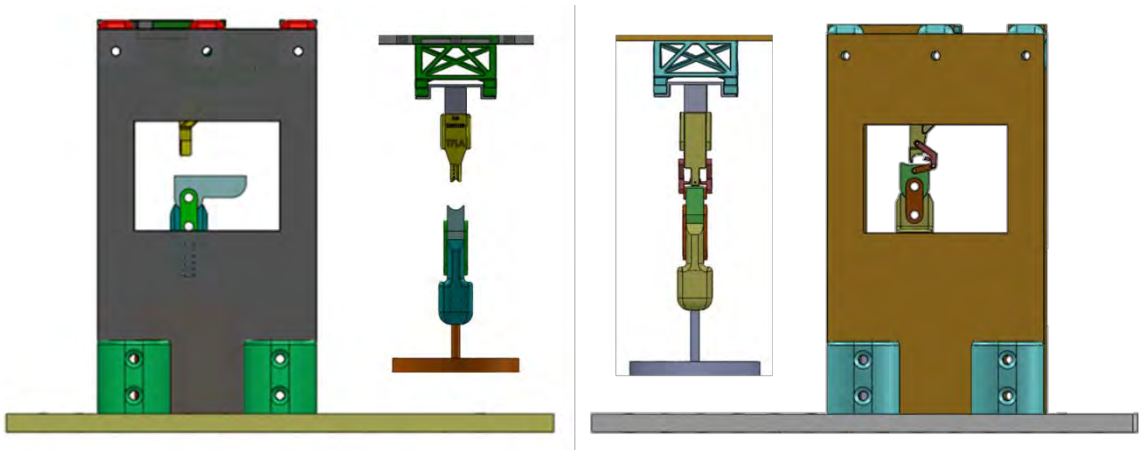

Figure 97 - Comparison of original dynamic DVM load device (left) and the modified DVM/DLM load concept (right)

This new device will require the removal of the head and abdomen of the *M.sexta* specimens. This is necessary because the horizontal push rod must compress the thorax, especially the tergal plate, in a lengthwise manner. The head and thorax obstruct the front and rear of the thorax and will not allow force to be applied to the phragma. Figure 98 shows a tergum and indicates where this longitudinal force must be applied. A magnified view of the conceptual mechanism and its simplified four-bar model are given in Figure

99. Finally, Figure 100 shows one full up/down cycle and indicates when the vertical and horizontal compressions occur.

Figure 98 - Location of longitudinal compressive force simulating DLM contraction. This image shows only the tergum, but the entire thorax would be intact for this experiment. The head and abdomen must be removed for access to the load application points at the front and rear phragma.

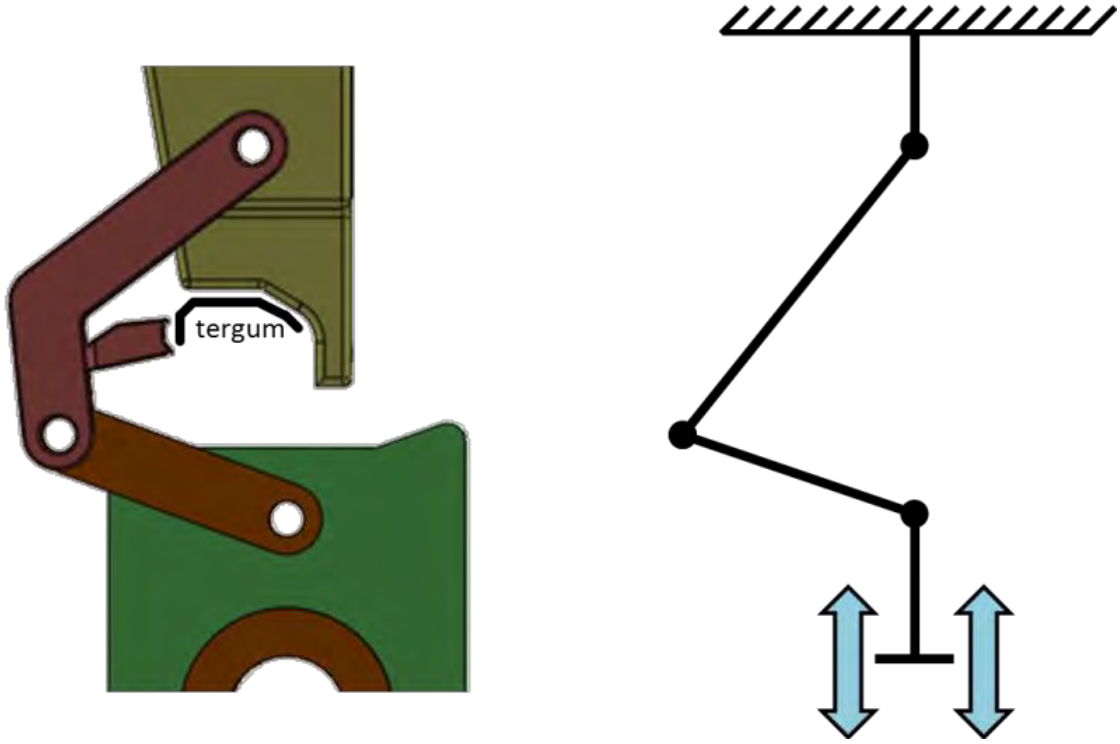

Figure 99 - Side view of the conceptual mechanism for bi-directional load application. The location of the tergum (front facing right of page) is indicated on the left. The equivalent four-bar linkage is given on the right. The top is anchored and the bottom piece simply moves up and down just like in the original dynamic load experiment.

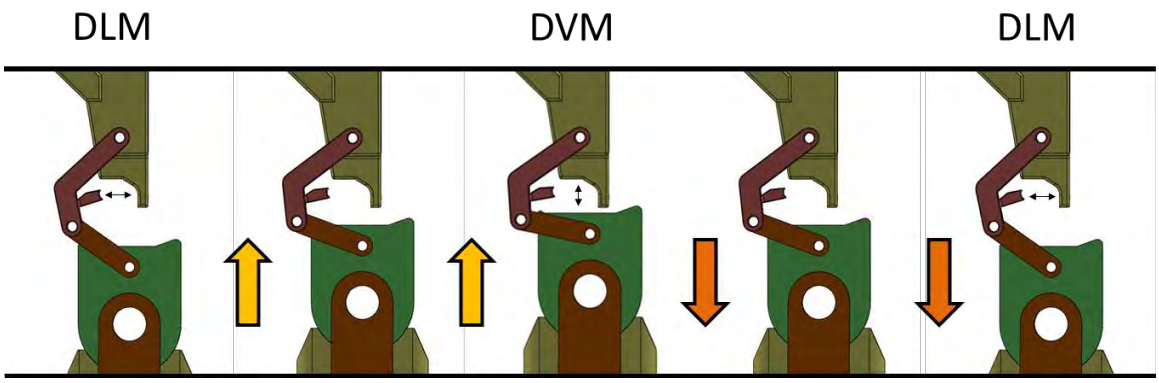

Figure 100 - Sequential representation of one full cycle. From left to right: Shaker is at lowest displacement and DLM compression is complete; shaker travels upward; shaker is at maximum displacement with full DVM compression; shaker travels downward; longitudinal compression begins again.

Appendix I. High-Speed Video Frame Sequence

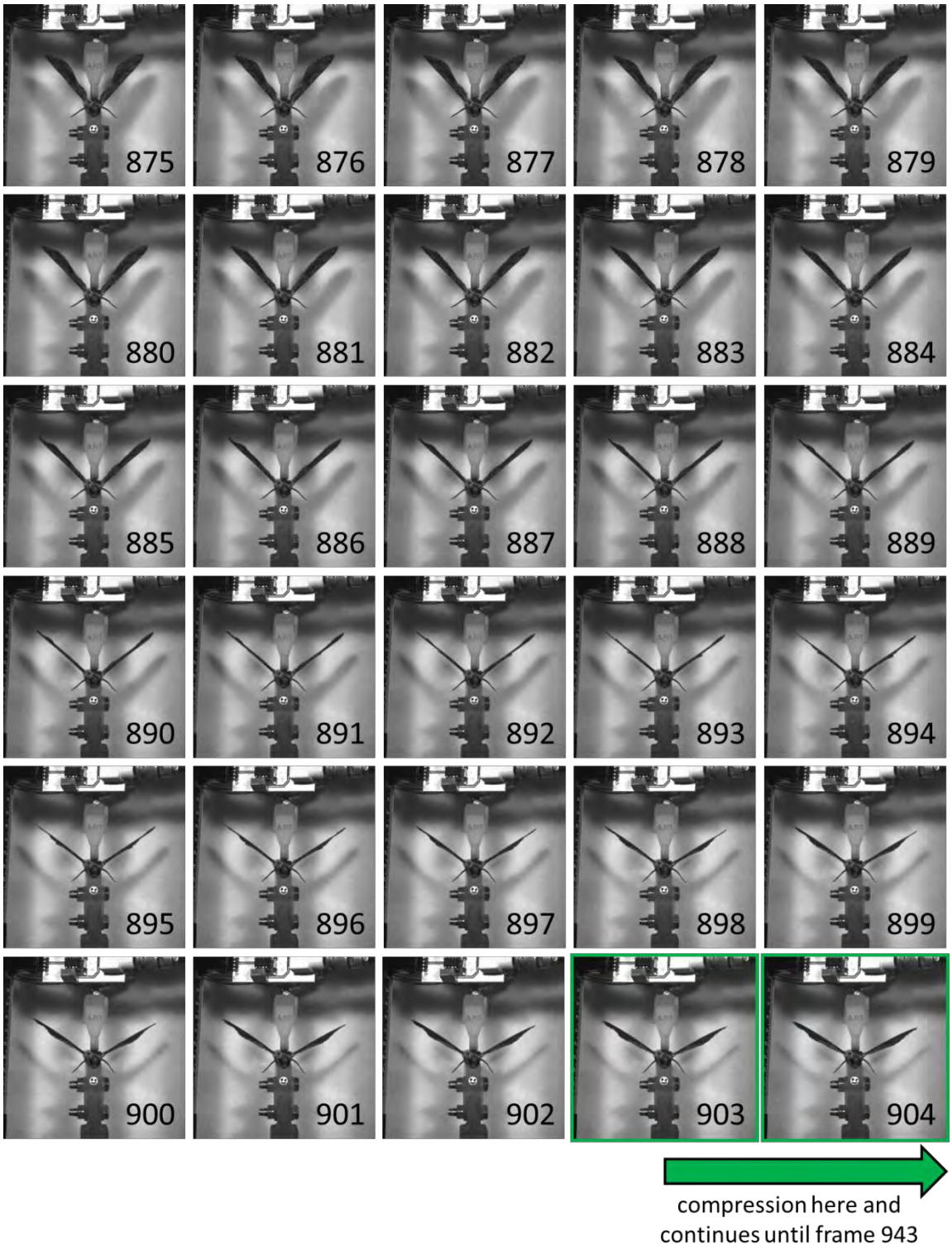

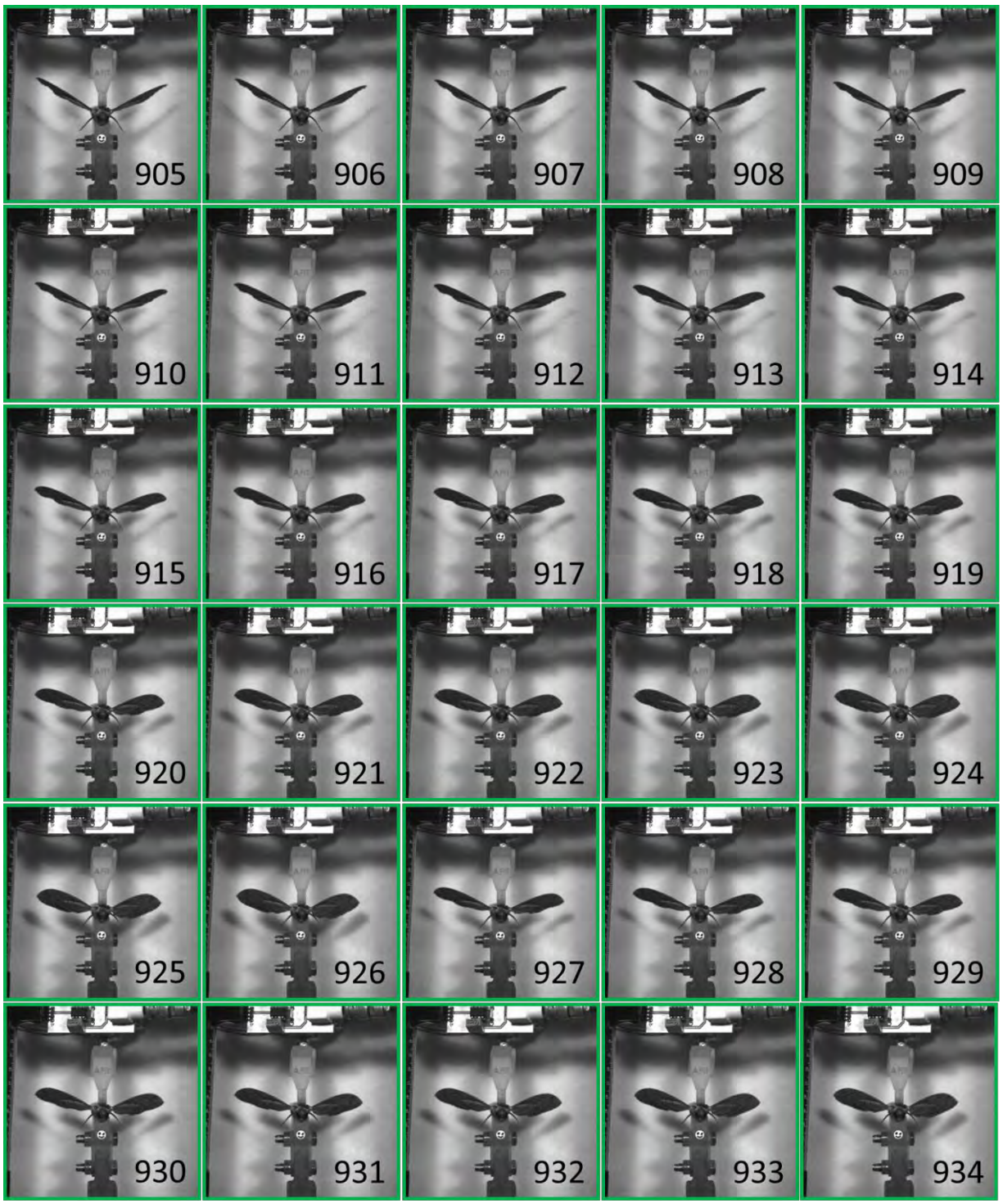

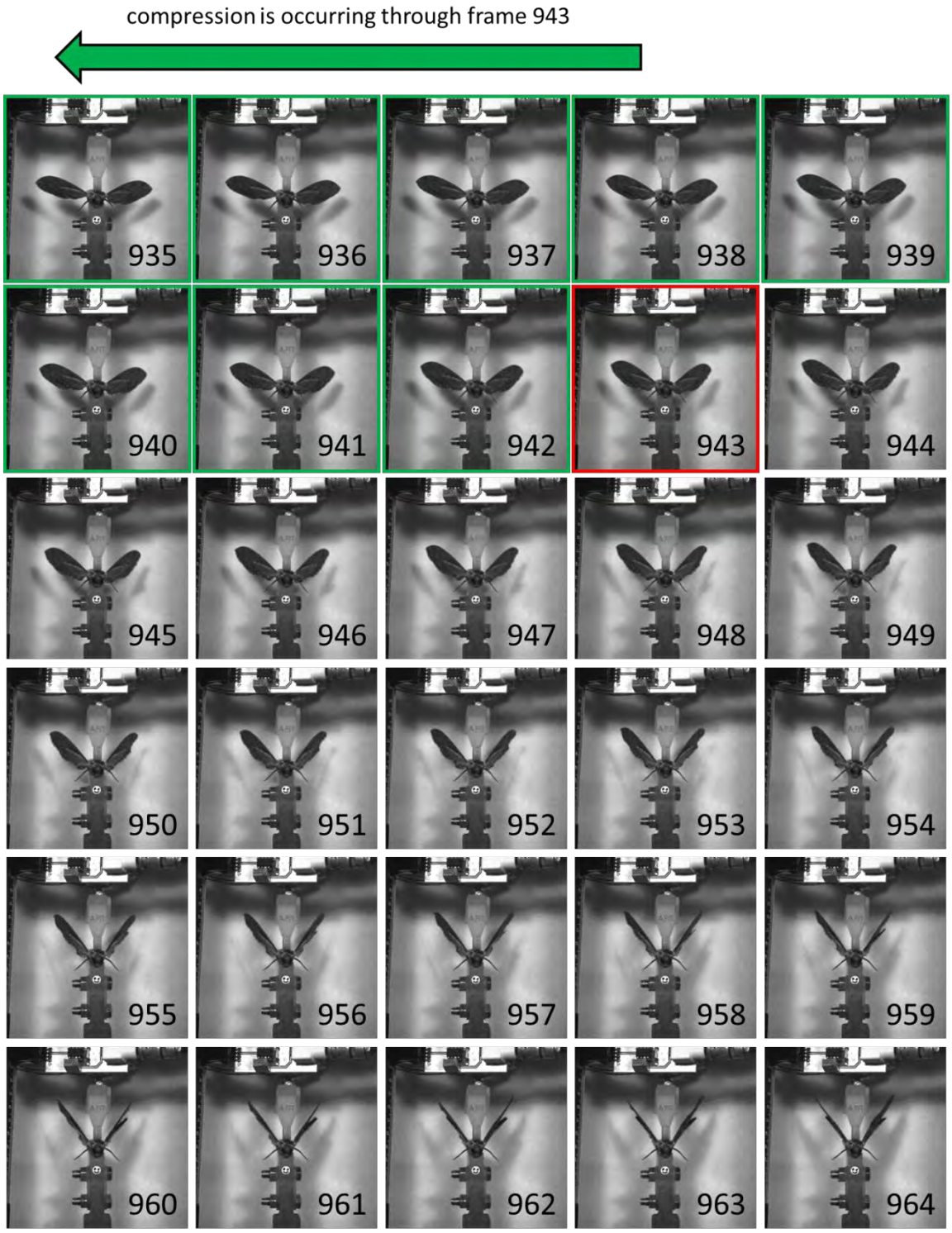

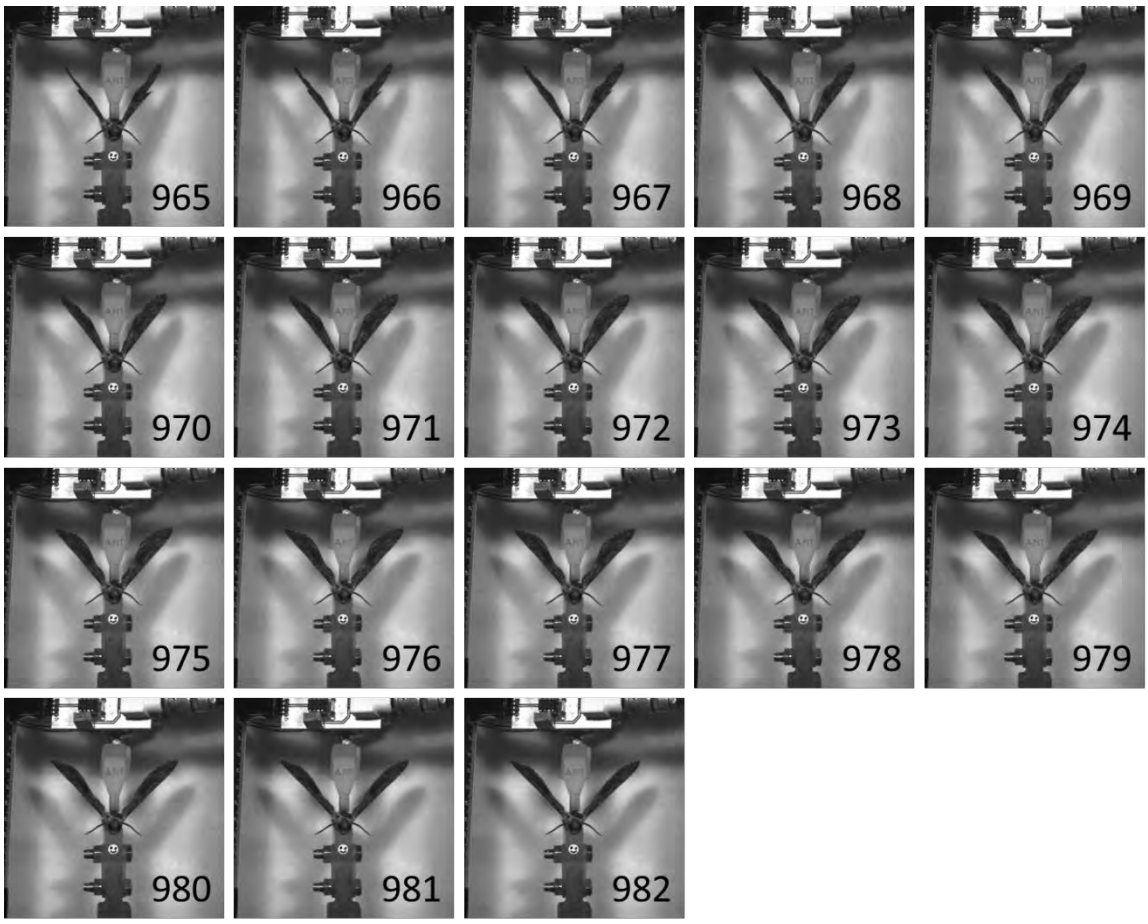

Appendix J. *M.sexta* Thorax Non-Linear Spring FE Model

The results of the static load and nanoindentation experiments are being incorporated into Luciano Demasi's non-linear FE models of the *M.sexta* thorax. His model Figure 101 is a moderately high-fidelity mathematical approximation of the thorax/wing mechanism and, like the author's earlier model, is not intended to replicate the exact geometry of the organism. The focus is on the characterization of the DVM and DLM flight muscle groups and their interaction with the system.

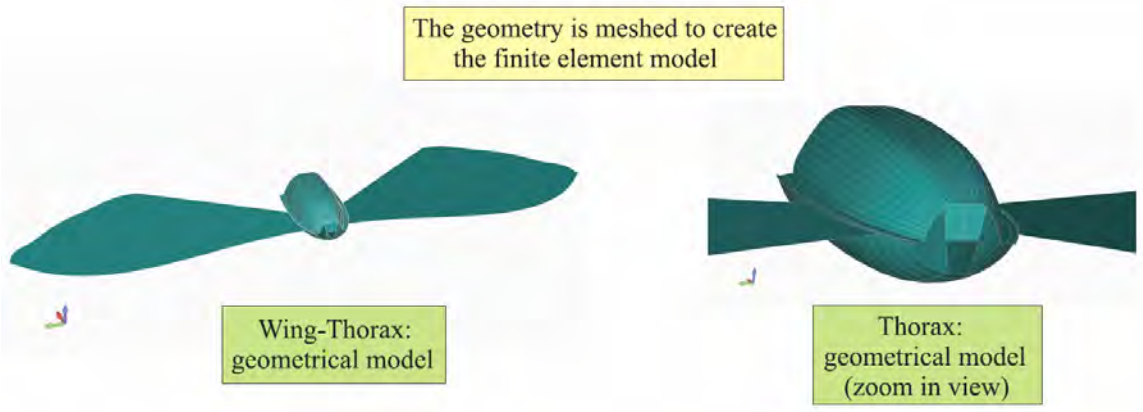

Figure 101 - Geometric model of the thorax-wing system (Demasi, Palazotto and Hollenbeck 2012)

The flight muscles are simulated by springs connecting the sternum/tergum (DVMs) and the anterior/posterior phragma of the tergum (DLMs) as shown in Figure 102.a. The boundary condition at the wing hinge is also modeled by springs (Figure 102.b). These springs must be non-linear in order to properly characterize the motion of the system. The details of non-linear FE modeling are beyond the scope of this thesis and will not be presented here.

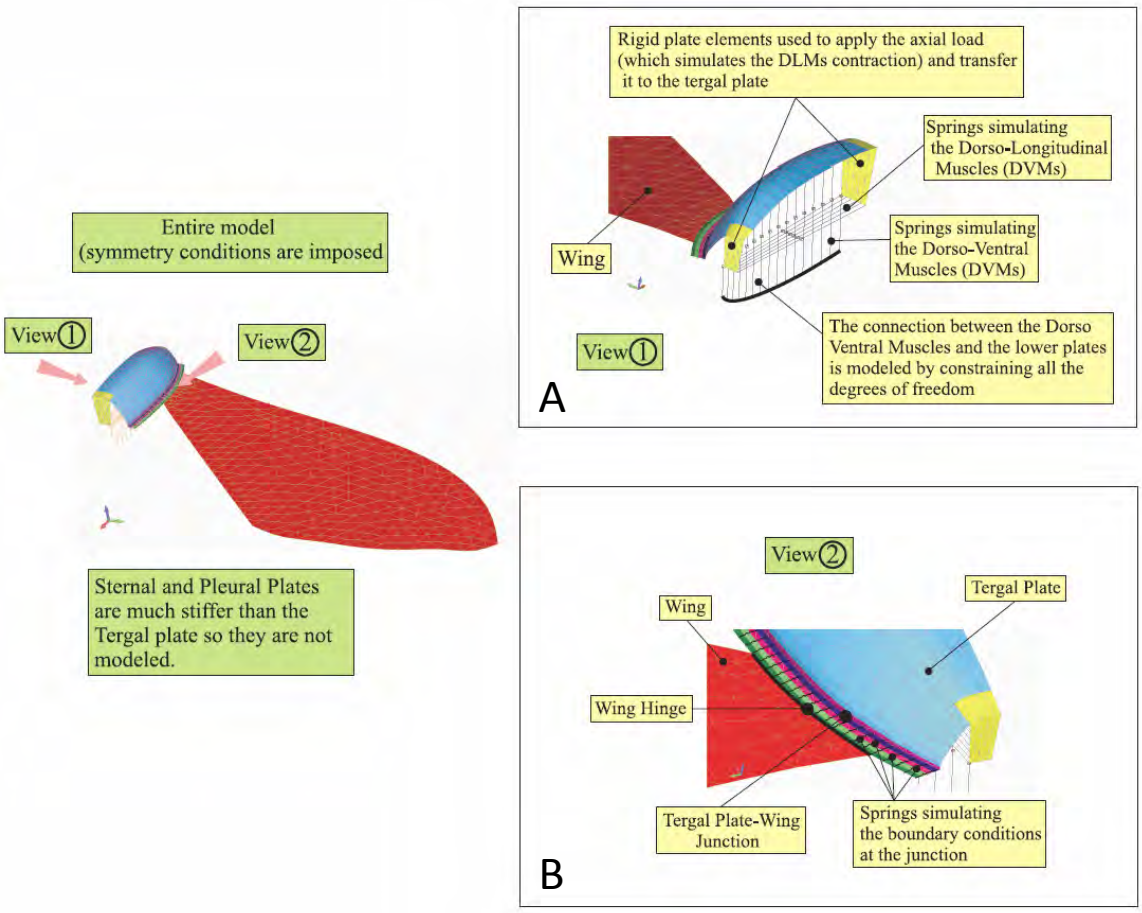

Figure 102 - Finite element model of the thorax-wing mechanism **(Demasi, Palazotto and Hollenbeck 2012)**

Preliminary analysis of Demasi's model has demonstrated that simulated DVM forces produce wing elevation and DLM forces produce the downstroke as expected (Figure 103).

Current efforts involve tuning these springs to improve the accuracy of the magnitude of these movements. The results of the author's static load experiment will be especially useful in this area. The compression/force relationship describing the entire thorax subjected to a vertical force (DVM simulation) from that experiment is given by

Eqn. 65, and the wing angle/force relationship is approximated with Eqn. 66. These are benchmarks to which Demasi's model can be compared.

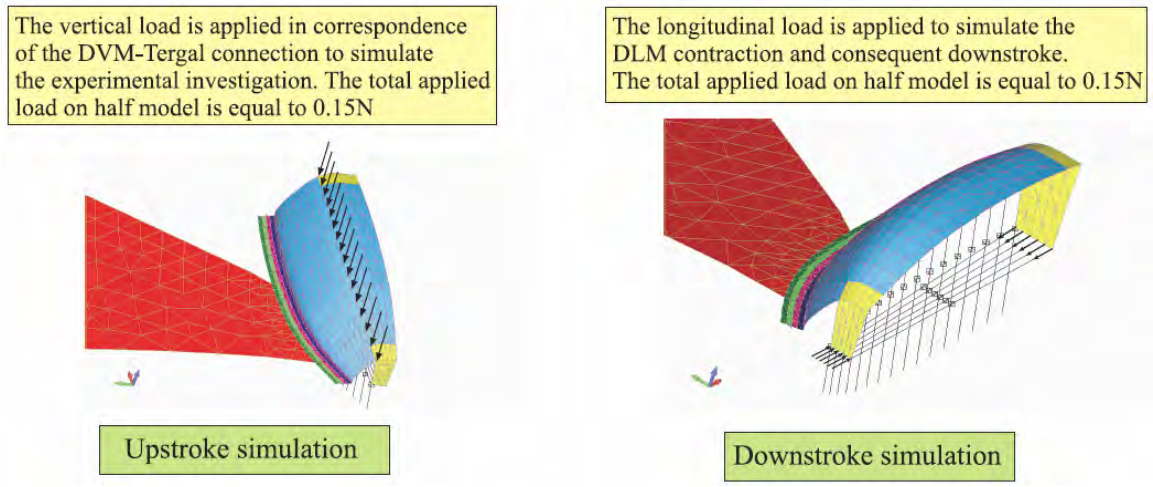

Figure 103 - Distributed loads applied to the tergum (DVM simulation) and the phragma (DLM simulation), **(Demasi, Palazotto and Hollenbeck 2012)**

$$x = 1.6069 \cdot F - 0.0514 \quad (65)$$

$$\theta = 122.16F^2 + 11.929x + 1.5274 \quad (66)$$

Bibliography

AeroVironment. "DARPA Contract Goals." *AVinc.* 2009. http://www.avinc.com/downloads/NAVPRLongDARPAV4.doc.pdf (accessed 2012).

—. *Nano Hummingbird.* 2012. http://www.avinc.com/nano.

Alexander, D.E. *Nature's Flyers; Birds, Insects and the Biomechanics of Flight.* Baltimore: The Johns Hopkins University Press, 2002.

Ashley, Steven. "Palm-Size Spy Plane." *Mechanical Engineering, ASME.* February 1998. http://www.memagazine.org/backissues/membersonly/february98/palmsize/palmsize.html.

Bao, X.Q., A. Bontemps, T. Vanneste, J-B Paquet, S. Grondel, and E. Cattan. "Fabrication and Actuation of Flapping-Wing Robotic Insect Prototype using Selected Polymer." *Bionic Robots Workshop.* 2011. http://www.emn.fr/z-dre/bionic-robots-workshop/uploads/Abstracts%20BRW%202011/26.pdf (accessed 2012).

Barbakedze, N., S. Enders, S. Gorb, and E. Arzt. "Local Mechanical Properties of the Head Articulation Cuticle in the Beetle Panchnoda Marginata (Coleoptera, Scarabaeidae)." *Journal of Experimental Biology* 209, no. 4 (February 2006): 722-730.

Bolsman, Caspar. *Flapping Wing Actuation Using Resonant Compliant Mechanisms.* PhD Dissertation, PhD Dissertation, Delft University of Technology, The Netherlands: Ipskamp, ISBN 9789090256856, 2010.

Bonsor, Kevin. *HowStuffWorks.com.* January 08, 2012. http://www.science.howstuffworks.com/spy-fly.htm (accessed 2012).

butterfliesandmoths.org. 2012. http://www.butterfliesandmoths.org (accessed January 2012).

Casey, T.M. "A Comparison of Mechanical and Energetic Estimates of Flight Cost for Hovering Sphinx Moths." *Journal of Experimental Biology* 91 (1981): 117-129.

Casey, T.M. "Flight Energetics of Sphinx Moths: Power Input During Hovering Flight." *Journal of Experimental Biology* 64 (1976): 529-543.

Chakravarty, U.K., and R. Albertani. "Energy Absorption Behavior of a Hyperelastic Membrane for Micro Air Vehicle Wings: Experimental and Finite Element Approaches." *International Journal of Micro Air Vehicles* 3, no. 1 (2011): 13-21.

Combes, S.A., and T.L. Daniel. "Into Thin Air: Contributions of Aerodynamic and Inertial-Elastic Forces to Wing Bending in the Hawkmoth Manduca sexta." *Journal of Experimental Biology* 206 (2003): 2999-3006.

Cook, R.D., D.S. Malkus, M.E. Plesha, and R.J. Witt. *Concepts and Applications of Finite Element Analysis, 4th ed.* John Wiley and Sons, Inc., 2002.

Daniel, T.L., and S.A. Combes. "Flexing Wings and Fins: Bending by Inertial or Fluid-Dynamic Forces?" *International Computational Biology* 42 (2002): 1044-1049.

Daniel, T.L., and T.L. Hedrick. "Flight Control in the Hawkmoth Manduca sexta: The Inverse Problem of Hovering." *Journal of Experimental Biology* 209 (August 2006): 3114-3130.

Daniel, Thomas L., and Michael S. Tu. "Submaximal Power Output from the Dorsolongitudinal Flight Muscles of the Hawkmoth Manduca Sexta." *Journal of Experimental Biology* 207 (2004): 4651-4662.

Demasi, Luciano, Anthony Palazotto, and Alex Hollenbeck. "Structural Investigation of a MAV's Thorax." *53rd Structures, Structural Dynamics and Materials Conference (SDM).* Honolulu HI: AIAA, 2012.

Dickinson, M. "Mechanical Properties of an Arthropod Exoskeleton." *Hysitron.com.* 2012. www.hysitron.com/LinkClick.aspx?fileticket=x-hOMSdlj3E%3d&tabid=324.

DoD. "DARPA Selects Micro Air Vehicle Contractor." *US Department of Defense News Release No. 676-97.* December 12, 1997. http://www.defense.gov/releases/release.aspx?releaseid=1538 (accessed January 2012).

Dumont, E.R., I.R. Grosse, and G.I. Slater. "Requirements for Comparing the Performance of Finite Element Models of Biological Structures." *Journal of Theoretical Biology* 256 (2009): 96-103.

Eaton, J.L. "Morphology of the Head and Thorax of the Adult Tobacco Hornworm, Manduca sexta (Lepidoptera: Sphingidae)." *Annals of the Entomological Society of America* 64 (1971): 437-445.

Ellington, C.P. "Power and Efficiency of Insect Flight Muscle." *Journal of Experimental Biology* 115 (1985): 293-304.

Ellington, C.P. "The Aerodynamics of Hovering Insect Flight VI. Lift and Power Requirements." *Philosophical Transactions of the Royal Society B: Biological* 305 (1984): 145-181.

Enders, S., N. Barbakadse, S.N. Gorb, and E. Arzt. "Exploring Biological Surfaces by Nanoindentation." *Materials Research Society* 19, no. 3 (March 2004): 880-887.

FedScoop. *Time Honors DARPA Projects on 2011 50 Best Inventions List.* November 2011. fedscoop.com/time-honors-darpa-projects-on-2011-50-best-inventions-list/.

FishbowlNY. *Time Lists 50 Best Inventions.* November 2011. http://www.mediabistro.com/fishbowlny/time-lists-50-best-inventions_b47098.

Flannigan, William C. "Finite Element Modeling of Arthropod Exoskeleton." MS Thesis, Department of Mechanical and Aerospace Engineering, Case Western Reserve University, Cleveland, 1998.

Harvard. *Harvard Microrobotics Laboratory.* 2012. http://www.micro.seas.harvard.edu/research.html.

Hay, J. "Introduction to Instrumented Indentation Testing." *Society for Experimental Mechanics: Characterization of Materials by Nanoindentation Series*, 2009: 66-72.

Hay, J., P. Agee, and E. Herbert. "Continuous Stiffness Measurement During Instrumented Indentation Testing." *Experimental Techniques: Nanomechanical Characteristics of Materials by Nanoindentation Series*, 2010: 86-94.

Hillerton, J.E. "Cuticle: Mechanical Properties." In *Biology of the Integument I. Invertibrates*, by J. Bereiter-Hahn, A.G.Matolsky, & K.S. Richards, 626-637. New York: Springer-Verlag, 1984.

Hoffmann, K. *An Introduction to Measurements using Strain Gages.* Darmstadt: Hottinger Baldwin Messtechnik GmbH, 1989.

Hollenbeck, Alex, Anthony Palazotto, and Mark Willis. "Evaluation of the Hawkmoth Thorax for Flapping-Wing Micro Air Vehicles." *Dayton Engineering and Sciences Symposium (DESS).* Dayton: Wright-State University OH, 2011.

Ifju, P., B. Stanford, and L. Kyu-Ho. "The Mechanics of Micro Air Vehicle Flexible Wings." University of Florida, 2008. Virginia Tech CSM Conference Presentation.

Jenikova, Zdenka. *Nikon Small World Gallery.* 2005. http://www.nikonsmallworld.com/gallery/year/2005/53 (accessed 2012).

Jensen, M., and T. Weis-Fogh. "Biology and Physics of Locust Flight V. Strength and Elasticity of Locust Cuticle." *Philisophical Transactions of the Royal Society B: Biological* 245 (1962): 137-169.

Karpelson, M., G.Y. Wei, and R.J. Wood. "A Review of Actuation and Power Electronics Options for Flapping-Wing Robotic Insects." *IEEE International Conference on Robotics and Automation.* Pasadena CA, USA, 2008.

Khan, Zaeem A., and Sunil K. Agrawal. "Study of Biologically Inspired Flapping Mechanism for Micro Air Vehicles." *AIAA Journal* 49, no. 7 (July 2011): 1354-1365.

Knospe, Carl R. *Insect Flight Mechanisms: Anatomy and Kinematics.* University of Virginia. Fall 1998. people.virginia.edu/~crk4y/research/flight.PDF.

Liu, H., and H. Aono. "Size Effects on Insect Hovering Aerodynamics: An Integrated Computational Study." *Bioinspiration and Biomimetics* 4 (March 2009): 13pp.

loadcelltheory.com. 2012. http://www.loadcelltheory.com/loadCellTheory.html.

Machin, K.E., and J.W.S. Pringle. "The Physiology of Insect Fibrillar Muscle II. Mechanical Properties of a Beetle Flight Muscle." *Proceedings of the Royal Society of London* B 151 (1959): 204-225.

Martin, M., M. Olek, M. Giersig, and H. Schmitz. "Micromechanical Properties of Consecutive Layers in Specialized Insect Cuticle: The Gula of Pachnoda marginata (Coleoptera, Scarabaeidae) and the Infrared Sensilla of Melanophila acuminate (Coleoptera, Buprestidae)." *Journal of Experimental Biology* 211 (2008): 2576-2583.

McMichael, J.M., and M.S. Francis. "Micro Air Vehicles - Toward a New Dimension in Flight." *Unmanned Systems* 15, no. 3 (1997): 8-17.

MTS. "Nano Indenter G200 User's Manual." *MTS Systems Corporation.* Doc. No. G2A-13192-0, April 2007.

Murray, Jeremy, Ryan O'Hara, and Anthony Palazotto. "The Use of Photogrammetry to Evaluate Dynamic Characteristics of a Manduca Sexta Wing." *Dayton Engineering Sciences Symposium (DESS).* Dayton: ASME, 2011.

Norris, A., A. Palazotto, and R. Cobb. "Structural Dynamic Characterization of an Insect Wing: Toward the Development of Bug Sized Flapping Wing Micro Air Vehicles." *American Institute of Aeronautics and Astronautics*, 2006: 2010-2790.

Oliver, W.C., and G.M. Pharr. "An Improved Technique for Determining Hardness and Elastic Modulus Using Load and Displacement Sensing Indentation Experiments." *Journal of Materials Research* 7 (1992): 1564-1583.

Omega. *The Strain Gage.* 2012. www.omega.com/literature/volume3/strain2.html.

Pennycuick, C.J., and M.A. Rezende. "The Specific Power Output of Aerobic Muscle Related to the Power Density of Mitochondria." *Journal of Experimental Biology* 108 (1984): 377-392.

Ramesh, K.T. *Nanomaterials, Mechanics and Mechanisms.* New York: Springer, 2009.

Reeder, Mark. *International Journal of Micro Air Vehicles.* Vol. 3. Multi-Science Publishing, 2011. Editorial, inside front cover.

Reinecke, J.P., J.S. Buckner, and S.R. Grugel. "Life Cycle of Laboratory-Reared Tobacco Hornworms, Manduca sexta: A Study of Development and Behavior using Time-Lapse Cinematography." *Biological Bulletin* 158 (February 1980): 129-140.

Sims, T. "A Structural Dynamic Analysis of a Manduca Sexta Forewing." MS Thesis, Air Force Institute of Technology, Wright-Patterson AFB, OH, 2010.

Sims, T., A Palazotto, and R. Cobb. "A Structural Dynamic Analysis of a Manduca Sexta Forewing." *International Journal of Micro Air Vehicles* 2, no. 3 (September 2010).

Steltz, E., M. Seeman, S. Avadhanula, and R.S. Fearing. "Power Electronics Design Choice for Piezoelectric Microrobots." *IEEE International Conference on Intelligent Robots and Systems.* Beijing, China, 2006.

Stevenson, R.D., and R.K. Josephson. "Effects of Operating Frequency and Temperature on Mechanical Power Output form Moth Flight Muscle." *Journal of Experimental Biology* 149 (1990): 61-78.

Sun. "High-Lift Generation and Power Requirements of Hovering Insect Flight." *Fluid Dynamics Research* 37 (2003): 21-39.

Sun, J.Y., J. Tong, and J. Zhou. "Application of Nano-Indenter for Investigation of the Properties of the Elytra Cuticle of the Dung Beetle (Copris ochus Motschulsky)." *Institution of Electrical Engineering Proceedings, Nanobiotechnology* 153, no. 5 (October 2006): 129-133.

Sun, M., and G. Du. "Lift and Power Requirements of Hovering Insect Flight." *Acta Mechanica Sinica* 19, no. 5 (2003): 458-469.

Tubbs, T.B. "Biological Investigation of the Stimulated Flapping Motions of the Moth, Manduca Sexta." MS Thesis, Air Force Institute of Technology, Wright-Patterson AFB OH, 2011.

Vincent, Julian F.V., and Ulrike G.K. Wegst. "Design and Mechanical Properties of Insect Cuticle." *Arthropod Structure and Development* 33, no. 3 (July 2004): 187-189.

Wainwright, S.A., W.D. Biggs, J.D. Currey, and J.M. Gosline. *Mechanical Design in Organisms.* Princeton: Princeton University Press, 1982.

Wasserthal, Lutz T. "Flight-Motor-Driven Respiratory Air Flow in the Hawkmoth Manduca Sexta." *Journal of Experimental Biology* 204 (July 2001): 2209-2220.

Weis-Fogh, T. "Tetanic Force and Shortening in Locust Flight Muscle." *Journal of Experimental Biology* 33 (1956): 668-684.

Willis, Mark. Associate Professor of Biology, Case Western Reserve University, Cleveland OH. Personal Correspondence, July 26, 2011.

—. Associate Professor of Biology, Case Western Reserve University, Cleveland OH. Personal Correspondence, February 10, 2012.

Willmott, A.P., and C.P. Ellington. "The Mechanics of Flight in the Hawkmoth Manduca Sexta." *Journal of Experimental Biology* 200 (1997): 2705-2722.

Wood, R.J. "The First Takeoff of a Biologically Inspired At-Scale Robotic Insect." *IEEE Transactions on Robotics* 24, no. 2 (April 2008): 341-347.

WSU. *Wright State Micro Air Vehicle Open House.* March 21, 2011. http://www.webapp2.wright.edu/web1/newsroom/2011/03/21wright-state-micro-air-vehicle-open-house.

Wu, P., B. Stanford, and P. Ifju. "Insect-Inspired Flapping Wing Kinematics Measurements with Digital Image Correlation." *SEM Annual Conference.* Albuquerque: Society of Experimental Mechanics, Inc., 2009.

Zhao, L., and X. Deng. "Power Distribution in the Hovering Flight of the Hawk Moth Manduca Sexta." *Bioinspiration and Biomimetics* 4 (2009): 7pp.

Vita

2nd Lieutenant Alex C. Hollenbeck graduated from O'Fallon Township High School in O'Fallon, Illinois. He entered undergraduate studies at the Missouri University of Science and Technology (formerly University of Missouri-Rolla) in Rolla, Missouri where he graduated Magna Cum Laude with a Bachelor of Science degree in Mechanical Engineering in May 2010.

He was commissioned through Detachment 442 AFROTC at the Missouri University of Science and Technology. His first assignment was at Wright-Patterson AFB as a student at the Air Force Institute of Technology where he is currently pursuing a Master of Science degree in Aeronautical Engineering. Upon graduation, he will be assigned to the Air Force Research Lab at Eglin AFB, Florida.

REPORT DOCUMENTATION PAGE		Form Approved OMB No. 0704–0188
The public reporting burden for this collection of information is estimated to average 1 hour per response, including the time for reviewing instructions, searching existing data sources, gathering and maintaining the data needed, and completing and reviewing the collection of information. Send comments regarding this burden estimate or any other aspect of this collection of information, including suggestions for reducing this burden to Department of Defense, Washington Headquarters Services, Directorate for Information Operations and Reports (0704–0188), 1215 Jefferson Davis Highway, Suite 1204, Arlington, VA 22202–4302. Respondents should be aware that notwithstanding any other provision of law, no person shall be subject to any penalty for failing to comply with a collection of information if it does not display a currently valid OMB control number. PLEASE DO NOT RETURN YOUR FORM TO THE ABOVE ADDRESS.		
1. REPORT DATE (DD–MM–YYYY) 23 03 2012	2. REPORT TYPE Master's Thesis	3. DATES COVERED *(From — To)* Aug 2010-Mar 2012
4. TITLE AND SUBTITLE Title in Title Case Evaluation of the Thorax of *Manduca sexta* for Flapping-Wing Micro Air Vehicle Applications		5a. CONTRACT NUMBER 5b. GRANT NUMBER 5c. PROGRAM ELEMENT NUMBER
6. AUTHOR(S) Hollenbeck, Alex C. 2Lt, USAF		5d. PROJECT NUMBER 5e. TASK NUMBER 5f. WORK UNIT NUMBER
7. PERFORMING ORGANIZATION NAME(S) AND ADDRESS(ES) Air Force Institute of Technology Graduate School of Engineering and Management (AFIT/ENY) 2950 Hobson Way WPAFB OH 45433-7765		8. PERFORMING ORGANIZATION REPORT NUMBER AFIT/GAE/ENY/12-M22
9. SPONSORING / MONITORING AGENCY NAME(S) AND ADDRESS(ES) Dr. Douglas Smith AFOSR/RSA (703) 696-6219 DSN (426-6219 Fax (503) 696-7320 E-mail: douglas.smith@aforsr.af.mil Air Force Office of Scientific Research Arlington VA		10. SPONSOR/MONITOR'S ACRONYM(S) AFOSR 11. SPONSOR/MONITOR'S REPORT NUMBER(S)
12. DISTRIBUTION / AVAILABILITY STATEMENT APPROVED FOR PUBLIC RELEASE; DISTRIBUTION UNLIMITED		
13. SUPPLEMENTARY NOTES This material is declared a work of the U.S. Government and is not subject to copyright protection in the United States.		

14. ABSTRACT

The tobacco hornworm hawkmoth (*Manduca sexta*) provides an excellent model from which to garner knowledge pertaining to the development of a Flapping Wing Micro Air Vehicle (FWMAV). Insect-sized FWMAVs will be used by the future warfighter for reconnaissance, nuclear/chemical/biological hazard sensing, and targeting.

One of the major challenges facing FWMAV developers is the energetically demanding nature of low Reynolds flapping flight. Investigating the *M.sexta* thorax/wing flapping mechanism as a mechanical system provided insight into its inherent efficiency. The energetics of the thorax under static loading were examined using a load-application technique. It was discovered that the thorax resists compression by a spring constant $k = 0.62\ N/mm$ under the action of the dorsoventral flight muscles (DVMs).

Constant stiffness measurement (CSM) nanoindentation of a major component of the thoracic exoskeleton, the tergum, revealed an elastic modulus of 5 GPa. This value is a benchmark for engineers seeking energy-storing materials for a FWMAV fuselage.

Finally, a truly groundbreaking device was devised and used to directly measure the power requirement of the (DVMs) at hovering frequency (25 Hz). This effort yielded a mechanical power output of 72-143 $W*kg^{-1}$ for the DVMs. The feasibility of the author's approach was confirmed by the agreement of this conclusion with published results.

15. SUBJECT TERMS

Manduca sexta, M.sexta, Micro Air Vehicle, Flapping-Wing, FWMAV, MAV, Power Density, Nanoindentation

16. SECURITY CLASSIFICATION OF:			17. LIMITATION OF ABSTRACT	18. NUMBER OF PAGES	19a. NAME OF RESPONSIBLE PERSON .Dr. Anthony Palazotto, Professor, AFIT, (ENY)
a. REPORT U	b. ABSTRACT U	c. THIS PAGE U	UU	164	19b. TELEPHONE NUMBER (Include Area Code) (937)255-3636, ext. 4599 Email: Anthony.palazotto@afit.edu